The Dissertation Committee for Anthony Michael Scopatz
certifies that this is the approved version of the following dissertation:

Essential Physics for Fuel Cycle Modeling & Analysis

Committee:

_____
Erich Schneider, Supervisor

_____
Steven Biegalski

_____
Sheldon Landsberger

_____
Mark Deinert

_____
Man-Sung Yim

Essential Physics for Fuel Cycle Modeling & Analysis

by

Anthony Michael Scopatz, B.S., M.S.E.

DISSERTATION

Presented to the Faculty of the Graduate School of

The University of Texas at Austin

in Partial Fulfillment

of the Requirements

for the Degree of

DOCTOR OF PHILOSOPHY

THE UNIVERSITY OF TEXAS AT AUSTIN

December 2011

For Mary, Jana, & Stephen Scopatz

$\mu\eta\delta\grave{\epsilon}\nu \ \acute{\alpha}\gamma\alpha\nu$

Acknowledgments

I would like to first evoke my unending appreciation to Dr. Erich Schneider for guiding and advising me through out my graduate studies at the University of Texas. Furthermore, I would like to thank the Nuclear & Radiation Engineering program for granting me countless opportunities and support over the years.

Moreover, I am continually indebted to Dr. Jun Li and Dr. Man-Sung Yim for their influence, criticisms, and efforts without which much of this work would have been severely impoverished.

Additionally, gratitude unbound must be expressed to The Hacker Within. At the risk of leaving many worthy friends unacknowledged, a heartfelt thanks to Dr. Paul Wilson, Dr. Milad Fatenejad, and Dr. Puneet Kishor for challenging me to be a better scientist and engineer. To Kathryn Huff, words fail.

For their unwavering support and understanding, the company Enthought deserves great praise for helping me persevere through the course of my studies. In specific, the resolutions of Dr. Travis Oliphant and Jonathan March cannot go unrecognized.

Essential Physics for Fuel Cycle Modeling & Analysis

Publication No. _____

Anthony Michael Scopatz, Ph.D.
The University of Texas at Austin, 2011

Supervisor: Erich Schneider

Nuclear fuel cycles (NFC) are the collection of interconnected processes which generate electricity through nuclear power. Due to the high degree of coupling between components even in the simplest cycles, the need for a dynamic fuel cycle simulator and analysis framework arises. The work presented herein develops essential physics models of nuclear power reactors and incorporate them into a NFC simulation framework.

First, a one-energy group reactor model is demonstrated. This essential physics model is then to simulate a sampling fuel cycles which are perturbations of well known base-case cycles. Because the NFC may now be simulated quickly, stochastically modeling many fuel cycle realizations dramatically expands the parameter space which may be analyzed. Finally, a multigroup reactor model which incorporates spectral changes as a function of burnup is presented to increase the fidelity of the original one-group reactor.

These methods form a suite of modeling technologies which reach from the lowest levels (individual components) to the highest (inter-cycle compar-

isons). Prior to the development of this model suite, such broad-ranging analysis had been unrealistic to perform. The work here thus presents a new, multi-scale approach to fuel cycle system design.

Table of Contents

List of Tables

List of Figures

Chapter 1

Introduction

Nuclear fuel cycles (NFC) are the collection of interconnected processes which generate electricity through nuclear power. At a minimum, heavy metal resources (U, Th) are removed from the ground and fissioned in a reactor, releasing energy. Generally, this energy is converted into electricity while the excess process heat is released to the environment. After the fuel is burned, it is removed from the reactor and stored as a solid on the surface. This is known as a the once-through fuel cycle.

This work focuses on methods for assessing an open fuel cycle and a variety of other strategies which have been subjected to intensive levels of technology development and deployment (TD&D).

There are many possible fuel cycle strategies that may be implemented in a nuclear power economy. The ability of nuclear power to recycle its own waste stream affords it distinct advantages. Foremost among these is the option to limit the number of deep geologic repositories (DGR) that must be built to dispose of waste. All reactors generate fission products (FP) from which further fissioning is not possible. The vast majority of fuel cycles call for the FP masses to be buried. DGR space is limited and precious, particu-

larly in light of the United States Senate 2009 decision to cease work on the Yucca Mountain Project. By closing the fuel cycle it is possible that only one repository need be built to satisfy future conceivable needs.

Repository space is not the sole consideration for NFC designers. Economic considerations are also weighted very heavily. The total cost of electricity from nuclear power must remain competitive with other forms of production. As all components in the cycle contribute to the overall cost burden, different strategies & technologies used may have disparate levelized electricity costs.

However, increased costs may be deemed acceptable if there is a commensurate value added. For instance, system designers often seek to improve the implicit resistance a fuel cycle has to the proliferation of weapons. Other considerations include natural resource utilization and sustainability, operating capacity, dynamic deployment effects, embodied energy costs, and political feasibility. The material balance for a given strategy affects, and often drives, these cycle wide metrics.

Because NFCs allow for recycling, material balance calculations may require a higher degree of algorithmic sophistication than is the case for other forms of electricity production. Recycle scenarios in which only one or two elements from waste streams are re-burned may partially close the fuel cycle. Mixed-oxide (MOX) strategies, such as those pursued in France, generally recycle only the plutonium stream. To compare alternative recycle strategies such as once-through and MOX on the basis of the metrics described above,

it is important to simulate the nuclear fuel cycle. This involves the characterization of material flows at each stage in terms of mass, isotopic composition, and time. This enables the coupling of nuclear fuel cycle component design to the design and evaluation of the system as whole.

Moreover, perturbing a single parameter in the NFC may have global reach over the entire cycle. For example, in the case of the once-through fuel cycle, altering the initial fresh-fuel ^{235}U enrichment given to a standard light-water reactor changes how much natural uranium must be mined earlier in the cycle. On the back end, changes to the design of a reprocessing facility also affect how much energy may be extracted from the fuel form and how the waste may be safely disposed.

Due to the high degree of interconnectedness between components even in the simplest cycles, the need for a dynamic fuel cycle simulator and analysis framework arises.

Many fuel cycles are studied via pre-defined base case scenarios in which all input parameters take on static values. Linear one-dimensional sensitivity studies may be performed which evaluate the effects of slightly changing a single parameter, while keeping all other inputs constant. However, perturbing a single value may push these base case models into a regime in which they are no longer valid. Moreover, important design regions of the parameter space may be overlooked by base case analysis due to the inability to perturb several parameters simultaneously. Exploring and analyzing design regimes that are far from pre-set scenarios is necessary for correctly designing components based

on parameters with global fuel cycle reach.

Strongly coupling component & cycle design considerations requires that the fuel cycle be simulated repeatedly, each time perturbing some aspect of the cycle. Decision analysis methods often require many iterations over the design option space to function in a statistically meaningful way. Thus it is desirable for NFC simulations to run quickly. This in turn requires that component simulation is even faster. By capturing only the essential physics in component models, commensurate algorithmic speed boosts are obtained.

Essential physics models are fuel cycle component algorithms which remain physically valid in the locality on which they are defined. At a minimum, their inputs are *perturbable* within an acceptable range and their outputs respond accordingly. Such models do not seek to compute extraneous parameters that are not of direct importance to the system at hand. For example, the flux in the fuel region of a reactor is pertinent to the discharge material composition. However, the neutron current in the shielding is not. Essential physics models seek reasonable simplifications of more detailed computational simulations that preserve physics-driven responses to changes in important system inputs.

The work presented herein will develop essential physics models of nuclear power reactors and incorporate them into a NFC simulation framework.

The first is a fluence-based parameterized reactor burnup model. This method seeks to characterize nuclear power reactors on properties of the mate-

rial initially loaded into the core. The nuclides themselves will be parametrized in terms of the time-evolution of the neutron production and destruction rates, their burnup, and their transmutation vectors. Since no discretization will be done in energy or solid angle, the model will focus exclusively on computing material flows. Thus this method will have the fewest number of algorithmic steps while remaining perturbable.

Once this reactor model is demonstrated, it will be applied within a fuel cycle context. This will show the validity of such a model as a tool for system designers. Analyzing several strategies, such as a standard once-through fuel cycle, a recyclable uranium cycle, and a fast burner reactor cycle, will test the dynamic properties of the fluence-based model.

Having proved the reactor model inside of various cycles, the NFC framework will be ready to perform at scale. Picking the fast burner cycle from above, as it has the highest degree of complexity, many (stochastically chosen) realizations may be performed. With this hitherto unseen amount of data, fundamentally new types of analysis will be needed to parse through the information. Entropy-based measures will be considered as a surrogate for traditional linear sensitivity studies.

After considering the abilities and limitations of this multi-scale model, a refinement to the original fluence-based reactor model will be proposed. In many cores, the flux spectrum evolves along with the composition. Such effects would not be captured by the previously proposed reactor model. This in turn limits the fuel cycle schema that may be analyzed. The integration of this

multi-energy group model (which accounts for internal spectral shifts) into an NFC analysis framework follows analogously to the work above.

In §2, the one-energy group reactor model is demonstrated; §3 uses this essential physics model to simulate a sampling fuel cycles which are perturbations of well known base-case cycles. Next, §4 dramatically expands the space analyzed by stochastically modeling the NFC as a whole. §5 presents a multigroup reactor model which incorporates spectral changes as a function of burnup. Finally, concluding remarks are presented.

Chapter 2

One-Group Reactor Methodology

2.1 Introduction

Coupled neutron transport and fuel burnup calculations require large execution times and intensive computational resources. This constraint renders such calculations impractical when attempting to address high-level fuel cycle engineering problems on a reasonable time scale. The approaches taken in the past to circumvent these time constraints have typically sacrificed fidelity by fully decoupling the fuel cycle simulation from physics-based reactor burnup calculations [11].

Fuel cycle problems revolve around perturbing input parameter values and measuring corresponding component or systemic changes which result. For instance, initial fresh fuel compositions in a reactor may be varied to attain a specific burnup. Or repository impact may be studied by varying the cooling time before emplacement. Even the simplest once-through fuel cycle, when making isotopic considerations, has a large number of degrees of freedom, each featuring a continuum of acceptable values. Lengthy calculation times going from input to output fuel vectors makes a parameterization of these degrees of freedom a near impossibility.

Rather than relying on predetermined recipes that limit study to specific cores with precise burnups, there is a need for an essential physics mechanism that allows for quick, dynamic calculation of burnup parameters. The methodology that is described within details a tool for use in fuel cycle analyses that calculates these burnup-related parameters for any reactor or interacting fleet of reactors.

The burnup-related parameters include the input and output isotopic vectors for the reactor as well as the burnup itself, which in turn depends on criticality, allowable fluence, safety issues such as reactivity coefficient values, and other constraints. Other parameters may be of interest for specific fuel cycles and will be discussed as they arise. The burnup tool uses pre-tabulated values for the neutron production and destruction rates and the burnup as a function of initial isotope present and fluence. The algorithm then determines the burnup-fluence relationship, giving the burnup only in terms of the initial isotopics of the reactor. The initial isotopics of the core may be iterated using this process until the composition that reaches some target burnup is found. This process assumes that there are multiple actinide streams to be blended, and the blending ratios are unknowns to be computed. The output isotopics of the reactor are dependent on initial core composition and the burnup, and thus are calculated after other parameters. This tool may then be embedded within a full fuel cycle model. To demonstrate how such a coupled framework functions, it is applied to two fuel cycle concepts. Because the neutron production and destruction rates are integral quantities over all

energy, this reactor model is known as the one-group method.

The first of the two fuel cycles incorporates a limited uranium recycle strategy. Uranium from a standard pressurized water reactor (PWR) is reprocessed and blended with enriched natural uranium (NU) before going into the second core to be burned again. After this burn, it is noteworthy that further recycling via blending is still possible. In other words, this fuel cycle could be fully closed with respect to the uranium stream, avoiding the need to dispose of the reprocessed uranium that comprises over 90% of the mass of used PWR fuel on an initial heavy metal (IHM) basis. This is known as a recyclable uranium (RU) blend and burn fuel cycle since the uranium is reused in PWRs independently of other actinides. RU blend and burn is an attractive option since it has the potential to eventually do a near complete burn of all uranium in light water reactor (LWR) used fuel (UF) if used in a fully closed cycle.

The second fuel cycle that utilizes the burnup tool developed here demonstrates how the tool may be used to improve the fidelity of the fuel cycle material balance calculations associated with one of the Advanced Fuel Cycle Research and Development (AFC R&D) base-case proposals [44]. This case is a closed fuel cycle that uses a fast burner reactor (FR) with a conversion ratio of 0.5. Actinides are continually recycled in the FR while fission products (FP) are removed and disposed. The reprocessing facility that is built for fast reactor used fuel has a separation efficiency of 0.99 for all actinides. This is a meaningful option to explore since fast reactors are considered to be a key component of long term nuclear energy strategies that close the fuel cycle.

In these two instances the same basic algorithm is used to very quickly solve the blending problem to obtain the fresh fuel composition that achieves the desired discharge burnup (BUd); the isotopic content of the output is also calculated. A fuel cycle wrapper governs the mass streams through the reactors and other fuel cycle components.

As will be seen, many fuel cycle parameters may be calculated from the resulting data. Moreover due to the dynamic nature of this method, these parameters will be more accurate than if a static recipe or simple linearizion had been used. A static recipe would not be able to mix recyclable and low enriched uranium (LEU) streams in a way that respects the dependence of neutronic characteristics on feed composition, an issue that is inherent to the RU fuel cycle. Moreover, models that use static recipes may fail to accurately capture the evolution of material balances with each successive pass through a fast reactor.

The remainder of the one-group discussion proceeds as follows. §2.2 provides a full illustration of the burnup model. §2.3 discusses in depth the recyclable uranium and fast reactor fuel cycles to which the burnup model is applied. Next §2.4 presents the results obtained for these cycles. The final section is concludes the one-group discussion.

2.2   Burnup Model

The burnup model takes a given input isotopic composition and returns the maximum discharge burnup of the fuel as well as its post-irradiation

isotopic composition. Thus, if given a target burnup, the model can mix multiple material streams to solve for the fresh fuel composition that achieves this burnup.

The burnup model algorithm takes several quantities as inputs. The neutron production and destruction rates, the burnup, and the compositional evolution of every isotope initially present. Furthermore, these parameters are all specified as functions of fluence (F), the time integral of the total spatially-averaged flux in the reactor. A discussion of how to compute and compile these presupposed parameters follows later in this section.

2.2.1 Isotopic Transformation

The first of the burnup model parameters is the nuclide-specific transformation as a function of fluence. Let the subscript i denote the isotope initially present in the core, where as the subscript j labels those nuclides bred in. Hence $T_{ij}(F)$ [kg$_j$/kg$_i$] tracks the transmutation under fluence of the ith isotope into its daughters given a nominal reactor spectrum embodied by one-group cross sections. The daughters tracked include both fission products (FP) as well as transuranics (TRU). Figure 2.1 displays an example of this transformation data: the concentration in kilograms of tracked isotopes that are present in a sodium-cooled FR core as a function of 1 kg of the initial isotope (^{239}Pu). In the figure, only one isotope is non-zero at zero fluence (*i.e.* zero time in the reactor). For each reactor and fuel form, similar data are required for all transmuting nuclides initially present. Note that not all

Figure 2.1: ^{239}Pu Transformation as a Function of Fluence for a Sample Fast Reactor
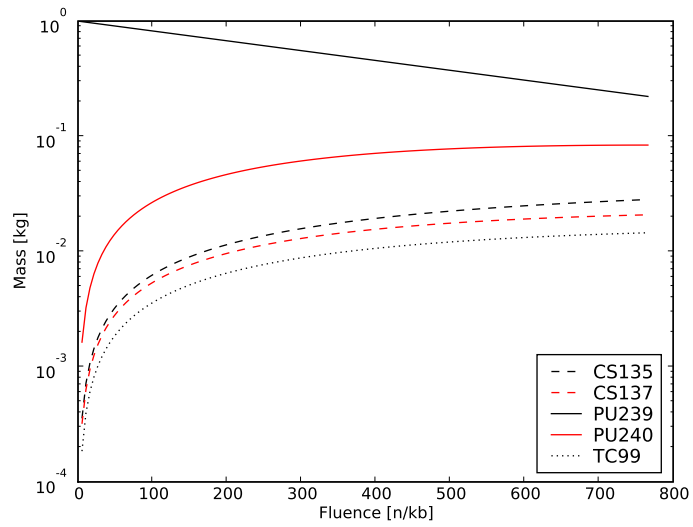
species that ^{239}Pu transforms into are displayed in Figure 2.1.

Since this example is for fast reactors, a constant flux of 2×10^{15} [n/cm2/s] was used when generating the transformation matrices. For PWRs a constant flux of 4×10^{14} [n/cm^2/s] was assumed. The units of fluence (F) here are [neutrons/kilobarn], abbreviated [n/kb], while the flux (ϕ) is again [n/cm^2/s], and time (t) is given in [days].

$$F = \int_0^t \phi dt' = \phi \int_0^t dt' = \phi \times t \cdot \frac{24 \cdot 3600 \cdot 10^3}{10^{24}} \tag{2.1}$$

In practice, the T_{ij} data need only exist for the actinides because coolant and structural material transmutation does not significantly impact core neutronic performance.

From here it is simple to apply initial isotopic weight fractions and the principle of superposition to Figure 2.1 and its analogies for all isotopes initially present in the core. This superimposed result then describes how 1 kg of fresh fuel transforms as a function of fluence within the core. Once the burnup model is applied, the output fluence will also be known (described below). Plugging the discharge fluence into the superimposed data yields the isotopic composition of the fuel at removal.

2.2.2 Neutron Production & Destruction Rates and Burnup

Other fuel cycle parameters that are required to perform burnup calculations are the neutron production and destruction rates, $p_i(F)$ and $d_i(F)$ [n/s/flux/kg$_i$]. These are given as functions of fluence for each isotope initially

Figure 2.2: Sample Neutron Production and Destruction Rate Figure as a Function of Fluence for an Initial Unit Mass of ^{239}Pu in a Sample Fast Reactor
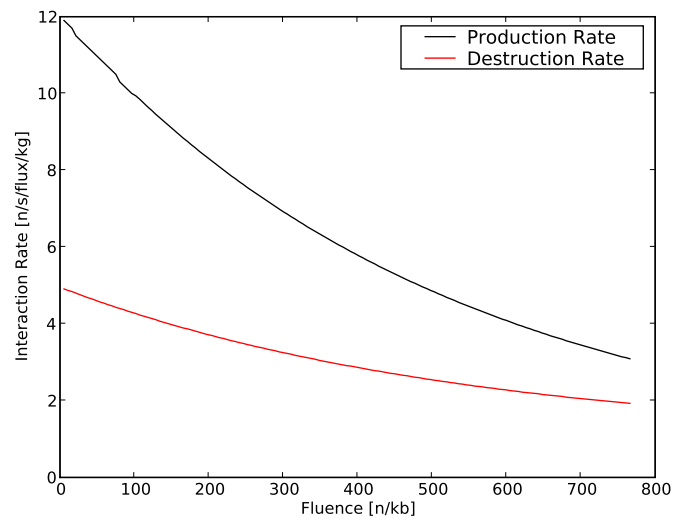
present in the core, just as with the isotopic transformation data. An example of these parameters is shown in Figure 2.2. This figure displays the production and destruction rates for one initial kilogram of ^{239}Pu in the sodium-cooled FR.

Figure 2.3: Burnup as a Function of Fluence for an Initial Unit Mass of Specific Nuclides in a Sample Fast Reactor
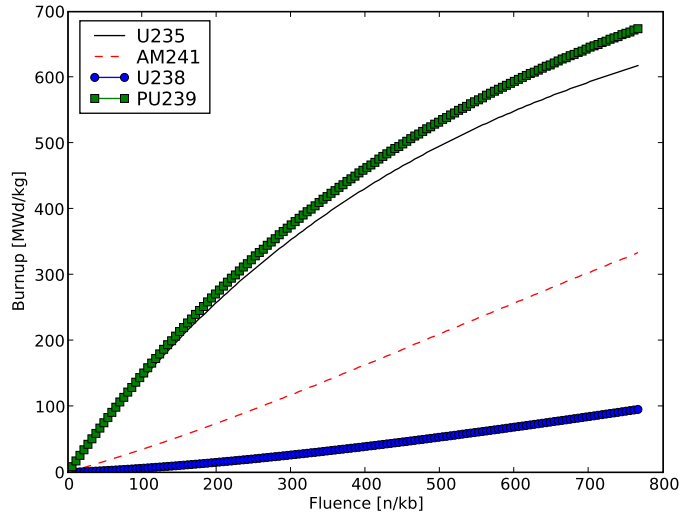
Lastly, the specific burnup for each isotope initially present, $\mathrm{BU}_i(F)$ [MWd/kg$_i$] must also be given to the burnup model. The burnup is defined in the same way as the neutron production and destruction rates. It is given as a function of fluence for each nuclide initially present in the core. Figure 2.3 displays $\mathrm{BU}_i(F)$ for a few actinides that may be present in the fresh fuel. Now that all input quantities have been outlined and defined, a description of

15

the algorithm that calculates the discharge burnup and the input and output fuel isotopics follows.

2.2.3   Solving for BUd and Isotopics

First, knowing only the $\mathrm{BU}_i(F)$, $p_i(F)$, $d_i(F)$, and $T_{ij}(F)$, the maximum achievable discharge burnup BUd [MWd/kgIHM] must be found. The burnup of the fresh fuel as a function of fluence is then computed as a mass-weighted linear combination of the burnups from the initial constituent isotopes. Similarly, the neutron production and destruction rates as a function of fluence for an arbitrary fresh fuel may be found. In the development below, it is assumed that the core consists of a lattice in which each cell contains two spatial regions, the fuel "F" and the coolant "C". (This formulation could generalize to additional regions.) Denote the mass of the ith isotope initially present in the fuel region "F" per unit mass of initial heavy metal (IHM) in the cell by m_i^F [kg$_\mathrm{i}$/kgIHM] and the mass of the ith isotope initially present in the coolant region "C" per unit mass of IHM by m_i^C [kg$_\mathrm{i}$/kgIHM]. Thus for the "Q"$^\mathrm{th}$ region, the mass weights are given by equation 2.2.

$$m_i^Q = \frac{N_i^Q}{N_\mathrm{IHM}} = \frac{n_i^Q A_i}{A_\mathrm{IHM}} \cdot \frac{\rho^Q \cdot \mathrm{MW}^F}{\rho^F \cdot \mathrm{MW}^Q} \frac{V^Q}{V^F} \tag{2.2}$$

Here, N_i is the number density, n_i is the atom fraction, A_i [amu] is the atomic weight, ρ [g/cm^3] is the density, and MW [g/mol] is the molecular weight.

Note that the volumes of the fuel and coolant regions, V^F and V^C [cm^3], are also needed to compute the IHM-normalized masses. An infinite

lattice made up of the unit cells mentioned above is used for this purpose. This two region method ignores the small effect of the cladding material on neutron capture. Call r [cm] the radius of the fuel pin and ℓ [cm] the pitch of the unit fuel cell. Additionally it is important to correct for the fact that not all fuel pin slots in a fuel assembly are filled with fuel. Denote S_T as the total number of pin slots in a fuel assembly and S_O as the open, non-fuel containing slots. The effective volumes are then given in equations 2.3 & 2.4.

$$V^F = \frac{\pi r^2}{\ell^2} \cdot \left(1 - \frac{S_O}{S_T}\right) \tag{2.3}$$

$$V^C = \frac{\ell^2 - \pi r^2}{\ell^2} \cdot \left(1 - \frac{S_O}{S_T}\right) + \frac{S_O}{S_T} \tag{2.4}$$

Hence the burnup of the core as a function of fluence $\mathrm{BU}(F)$ [MWd/kgIHM] is given by the following sum.

$$\mathrm{BU}(F) = \sum_i m_i^F \cdot \mathrm{BU}_i(F) \tag{2.5}$$

Once this burnup is known, the maximum discharge burnup can be computed via the fluence point for which the core ceases to be critical. The fluence-dependent neutron production and destruction rates for each constituent species are used to compute the multiplication factor, k.

When k drops below unity, a reactor full of this nuclide alone would no longer be able to sustain a chain reaction. $k(F)$ is approximated by calculating the full-core neutron production rate $P(F)$ [n/s/kgIHM] divided by the full-core average neutron destruction rate $D(F)$ [n/s/kgIHM].

$$k(F) = \frac{P(F)}{D(F)} \tag{2.6}$$

17

$k(F)$ may thus also be calculated, like $\mathrm{BU}(F)$, as a mass-weighted convolution of the $p_i(F)$ and $d_i(F)$. The method by which one obtains $P(F)$ and $D(F)$ from the isotope-specific rates is discussed in the following sections. Once computed, $k(F)$ is then set equal to unity and equation 2.6 is solved for the fluence. This point is the fluence at discharge and is denoted $F\mathrm{d}$ [n/kb]. $F\mathrm{d}$ may then be reinserted into equation 2.5 and the burnup of the fuel composition at discharge BUd [MWd/kgIHM] is attained.

Note that equation 2.6 can hold for a multi-batch fuel management scheme as well as a one batch core system. Extending this equation to a multi-batch system may be seen in §2.2.3.3.

Additional factors complicate the calculation of the core-average neutron production and destruction rates. A complete depiction of the neutron balance requires that $p_i(F)$ and $d_i(F)$ for non-fuel components of the core must also be known. These non-fuel components include the coolant outside of fuel regions and the non-actinide species in the fuel region (*e.g.* oxygen in UOX). Both of these classes of parasitic species serve to increase the full core destruction rate. Disadvantage factors also reflect that there is flux suppression in fuel regions, which needs to be accounted for in PWR cases. Furthermore, to account for spatial variation in the neutron flux when computing neutron interaction rates in non-fuel components, a general fuel assembly model is needed (as described above). For example, to reflect a standard PWR fuel assembly geometry values from the OECD Burnup Credit Criticality Benchmark [43] were used for LWRs and nominal values for fast reactors were taken from [10].

18

A walkthrough of how to calculate the core-average production and destruction rates, $P(F)$ and $D(F)$, from the known set of $p_i(F)$ and $d_i(F)$ for a given collection of m_i follows.

2.2.3.1 The Neutron Production Rate

The $p_i(F)$ and $d_i(F)$ are superimposed to build the full-core loading. These rates reflect the evolution of the neutron balance for an initial unit mass of the species i when exposed to the neutron flux spectrum in the reactor being studied. Therefore they are computed using cross sections prepared for a specific reactor and fresh fuel composition.

However as mentioned above, flux spectra and magnitudes are spatially dependent. The most basic geometric model is that of an infinite lattice of unit cells consisting of a central fuel region surrounded by a coolant-filled region. These two regions have neutron production and destruction rates that are distinct since the set of m_i that are used in each region is different.

The production rates for the fuel and coolant regions, $p^F(F)$ and $p^C(F)$ [n/s/flux/kgIHM], can be calculated in direct analogy to equation 2.5 for the burnup. The neutron production rate in the fuel region is

$$p^F(F) = \sum_i m_i^F \cdot p_i(F) \qquad (2.7)$$

and $p^C(F) = 0$ since the coolant contains no neutron producing isotopes.

The advantage of this algorithm is seen through equation 2.7. By assuming that isotopic production and destruction rates are known, superposi-

tion is then used combine the individual rates into full-core or region specific rates. This allows for fast recombining of initial core species without having to recalculate the isotopic rates from scratch. For instance, to calculate the burnups achievable from 2% and 4% ^{235}U enriched PWR fuel would typically require distinct computationally intensive runs because of differing initial fuel compositions. With this method all, that is needed is to change the m_i used in equation 2.7. For greater fidelity, one may obtain case-specific burnup parameters $p_i(F)$, $d_i(F)$ and $\text{BU}_i(F)$ and interpolate between a handful of precomputed sets.

However, the fuel region production rate is not equivalent to the full-core production rate. The core effect that is not seen at the fuel cell level is known as leakage. To capture this macroscopic effect a non-leakage probability P_{NL} is introduced. The P_{NL} effectively reduces the production rate of neutrons in the core. The P_{NL} used is characteristic of the reactor design and composition; it may be computed using macroscopic transport methods, but in practice it is used as a calibration parameter. Finally then, the full-core production rate is given simply as

$$P(F) = P_{NL} \cdot p^F(F) \tag{2.8}$$

Note that $P(F)$ here is normalized to a unit mass of IHM. Thus $P(F)$ has units of [n/s/kgIHM]. The neutron destruction rate must therefore be normalized in the same way.

2.2.3.2   The Destruction Rate

The full-core destruction rate $D(F)$ is calculated in the same manner as the fuel region production rate. However, the other nuclides in the reactor, while not contributing to fission, do contribute to neutron destruction in the core. In the fuel cell model used above, two other isotopes are present in a PWR core (^{16}O and ^{1}H) and one other main species in a FR core (^{23}Na).

To compute $D(F)$, the fuel region destruction rate $d^F(F)$, in analogy to the fuel region production rate equation 2.7, is required. Note that the units of $d^F(F)$ are [n/s/flux/kgIHM].

$$d^F(F) = \sum_i m_i^F \cdot d_i(F) \qquad (2.9)$$

Moreover, the coolant can strongly contribute to the destruction rate. However, it is important to take into account that for some fuel/coolant combinations the flux is not spatially uniform. For instance, in PWRs the thermal flux is generally higher in the coolant than in the fuel. To account for this, a disadvantage factor is introduced. For other reactor types, such as FRs, the flux profile is much flatter over the unit cell and a disadvantage factor is not necessary. The disadvantage factor ζ is qualitatively the average flux in the coolant divided by the average flux in the fuel. The fuel suppresses the thermal flux levels so ζ will always be greater than one. Since ζ is dependent on the composition of the fuel it is also a function of the fluence. A more complete examination of how to calculate $\zeta(F)$ is found in [13]. Figure 2.4 shows how $\zeta(F)$ changes with fluence for two LEU fuels with 3.2% and 4.3% ^{235}U. Thus

Figure 2.4: Disadvantage Factor as a Function of Fluence for LEU with a Three Batch Core
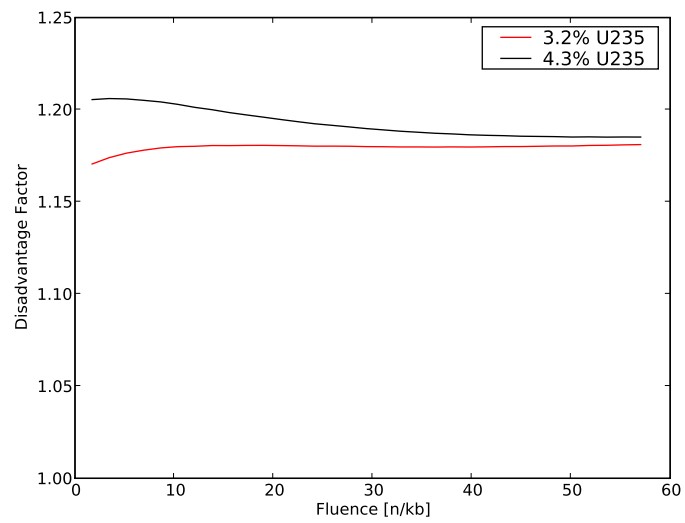
the coolant destruction rate is then given as

$$d^C(F) = \zeta(F) \cdot \sum_i m_i^C \cdot d_i(F) \tag{2.10}$$

Note that the volumetric weight in m_i^C for the coolant region already includes both empty and filled fuel pin slots. Therefore the full-core destruction rate $D(F)$ is given by the sum of the destruction rate in the fuel and the destruction rate in the coolant.

$$D(F) = d^F(F) + d^C(F) \tag{2.11}$$

Now that $P(F)$ and $D(F)$ are known, $k(F)$ may be calculated as per equation 2.6. Once again, Fd is defined such that $k(F\text{d}) = 1$ which yields the maximum discharge burnup $\text{BU}(F\text{d}) = \text{BUd}$.

2.2.3.3 Multiple Batch Cores

What has been shown above is how to find the discharge burnup with a given fuel composition for a one batch system. However, for multiple batches of fuel the process is less straightforward as the production and destruction rates are averaged over their end of cycle values for each batch. The strategy employed here is to perform these operations in reverse and then iterate over them. In other words, one picks a burnup and then solves for the multiplication factor. Then one picks another burnup that will yield a k closer to one and solves again for k. This process continues until a k is found that is acceptably close to one.

The bisection method is preferred to pick successively closer values of

k. It is not prone to the erratic behavior that arises when Newton's method is used with pointwise data. Furthermore, the bisection method ensures that the fuel is burnable. The bisection method requires that there must be both some fluence where $k < 1$ and a fluence such that $1 < k$. Since the multiplication factor is in reality continuous and roughly monotonic, these conditions imply that at some fluence $k = 1$. However, if these conditions fail then the fuel has too little fissile material to sustain a chain reaction.

Figure 2.5: Burnup as a Function of Fluence for Sample FR Fuel
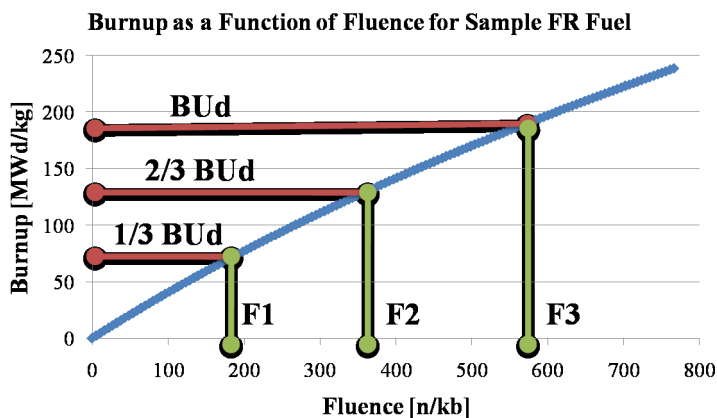
A walkthrough of this process for multiple batches follows. First, a maximum discharge burnup BUd is guessed. Say without loss of generality that the system at hand is concerned with a three batch refueling cycle. Then assuming equal inter-batch power sharing, the fluence must be found for three burnups, namely BUd, 2/3 BUd, and 1/3 BUd. Lines drawn on Figure 2.5 from the burnup axis to the curve and then down from the curve to the fluence

24

Figure 2.6: The Multiplication Factor as a Function of Fluence for Sample FR Fuel
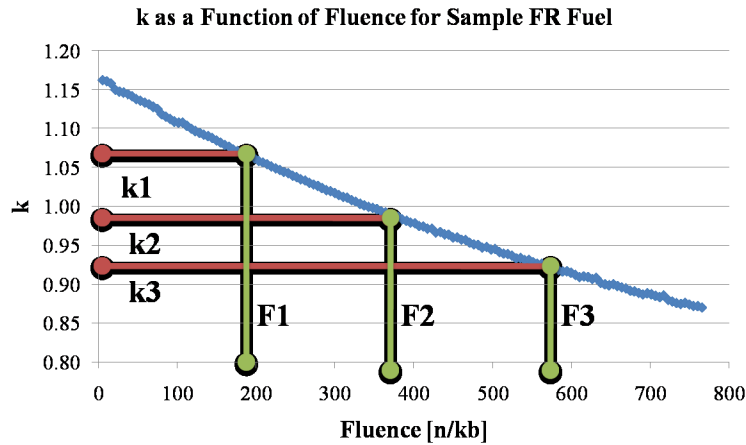
axis will give the fluence at the three points required. Note that the highest fluence ($F3$ here) is the fluence at discharge Fd. After the fluence for each of the burnups has been calculated, the multiplication factor of the system needs to be known.

To achieve this for a multi-batch core, a flux-weighted batch averaging procedure is followed. The multiplication factor at each fluence is determined by the $P(F)/D(F)$ ratio. Denote the batch number that a parameter is associated with by the subscript "b". In Figure 2.6, the three k_bs correspond to the three fluences chosen via the three burnup points on Figure 2.5, $k_b(F_b) = P_b(F_b)/D_b(F_b)$. These are interpreted as the multiplication factors if the full core was in fact composed entirely of fuel that had been exposed to this fluence. Thus the true multiplication factor of the core is the weighted

25

average of the production divided by destruction rates. With the flux as a weight for "B" batches,

$$k = \frac{\sum_b^B \frac{P_b(F_b)}{D_b(F_b)} \phi_b}{\sum_b^B \phi_b} \tag{2.12}$$

However, the average flux within each batch ϕ_b is not known. Moreover, because the batch power remains constant, ϕ_b does not. Yet the flux is by definition the time derivative of the fluence. Thus a good approximation of the flux is given in equation 2.13.

$$\phi_b \approx \frac{\Delta F}{\Delta t} \tag{2.13}$$

Here, ΔF can be measured at a given fluence by perturbing $\mathrm{BU}(F)$ by a small amount and finding the $\Delta\mathrm{BU}$. This is easily done as $\Delta\mathrm{BU}/\Delta F$ is identically the slope of the $\mathrm{BU}(F)$ graph at fluence F in Figure 2.5. Given the assumption of constant power density, a change in burnup yields a corresponding change in time such that

$$\Delta t = \Delta\mathrm{BU} \cdot \frac{T_{\mathrm{res}}}{\mathrm{BUd}} \tag{2.14}$$

Where BUd is the discharge burnup guess and T_{res} [days] is the residence time that the fuel took to obtain this burnup. Combining equations 2.13 & 2.14, ϕ_b is found to be

$$\phi_b \approx \frac{\Delta F}{\Delta\mathrm{BU}} \cdot \frac{T_{\mathrm{res}}}{\mathrm{BUd}} \tag{2.15}$$

By inserting equation 2.15 into equation 2.12, an expression for the effective multiplication factor for a multiple batch system at discharged time is ob-

26

tained.

$$k \approx \frac{\sum_b^B \frac{P_b(F_b)}{D_b(F_b)} \cdot \left.\frac{\Delta F}{\Delta \mathrm{BU}}\right|_b \cdot \frac{T\mathrm{res}}{\mathrm{BUd}}}{\sum_b^B \left.\frac{\Delta F}{\Delta \mathrm{BU}}\right|_b \cdot \frac{T\mathrm{res}}{\mathrm{BUd}}} = \frac{\sum_b^B \frac{P_b(F_b)}{D_b(F_b)} \cdot \left.\frac{\Delta F}{\Delta \mathrm{BU}}\right|_b}{\sum_b^B \left.\frac{\Delta F}{\Delta \mathrm{BU}}\right|_b} \tag{2.16}$$

Now that a batch-averaged k has been found, its value may be converged to unity via the bisection iterations. Another value of the maximum discharge burnup may then chosen and this process repeated until a BUd is found that yields a $k = 1$.

In the process of determining the maximum discharge burnup, Fd is also found. Analogously, a mass-weighted linear combination of the isotopic transformation matrices may be performed. The mass of the jth nuclide at fluence F is called $M_j(F)$ [kg$_\mathrm{j}$/kgIHM] and is given by

$$M_j(F) = \sum_i m_i^F \cdot T_{ij}(F) \tag{2.17}$$

Plugging in the fluence at discharge Fd into equation 2.17 will yield the mass of isotope j in the used fuel per kilogram of IHM. Performing this operation for all j isotopes of interest will yield the isotopic output vector for the core. Since fission product masses were included in the transformation matrices, the fission products at discharge are also known.

Figure 2.7 shows a graphical representation of the $M_j(F)$ for various isotopes present in a fast reactor. Each curve for each nuclide is the superposition of all of the transformation matrices. Some species, such as ^{238}U and ^{239}Pu, are burned out of the core faster than they are bred back in and are therefore represented by lines of negative slope. Other isotopes, namely fission

27

Figure 2.7: $M_j(F)$ for a Sample Fast Reactor for a Variety of Species
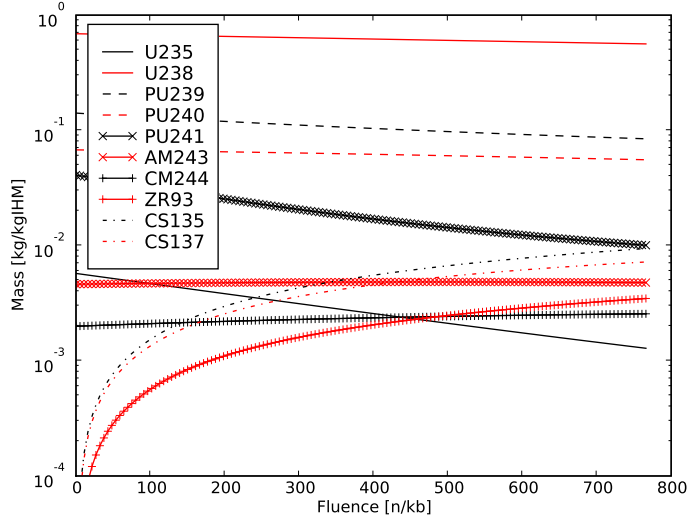
products, were not initially present and are bred into the core by any fissioning species. These are shown as the curves growing towards some asymptote. Still other nuclides, higher order species like ^{243}Am and ^{244}Cm, have a more dynamic effect. They grow into the core, peak, and start to burn out.

In conclusion, the above is an algorithm for finding the maximum discharge burnup and its discharge composition given only a fuel form represented by m_i^F, the pre-generated burnup parameters ($p_i(F)$, $d_i(F)$, $BU_i(F)$, and $T_{ij}(F)$), the number of batches in the core B, and the non-leakage probability P_{NL}. Methods for generating these burnup parameters are discussed in §2.2.4.

2.2.4 Burnup Parameter Generation

The burnup parameters $p_i(F)$, $d_i(F)$, $\text{BU}_i(F)$, and $T_{ij}(F)$ are typically calculated for a specific reactor design. However if the reactor type is perceived as being representative of all cores of that type, then the burnup parameters may be applied generally to all reactors of this type without having to recalculate new parameterizations. Qualitatively, what it means to be representative of a reactor type and fuel composition is that the neutron energy spectrum inherent in the few-group cross sections used to generate the burnup parameters is similar to that of other reactors of this type and other fuel compositions that will be studied.

In this study, the burnup parameters are calculated and tabulated based on the reactor-specific data libraries created from ORIGEN 2.2 [7] isotope-specific burnup analyses. The ORIGEN input libraries contain cross sections that are interpreted as generic to a reactor type and range of fuel compositions. For example, the libraries used here for fast reactors were prepared for a sodium cooled burner reactor with a target conversion ratio of 0.5. This reactor is described in more detail in [10]. The burnup model therefore utilizes pre-computed libraries of the $p_i(F)$, $d_i(F)$, $\text{BU}_i(F)$, and $T_{ij}(F)$ that were built up from ORIGEN runs. These libraries contain pointwise data as a function of fluence. Recall that all data in these libraries track the evolution of the parameter on a per unit mass basis.

More explicitly, ORIGEN 2.2 is run for a kilogram mass of a given nuclide with the characteristic input libraries. Therefore, the isotopic mass

29

balances and reaction rates obtained from this run reflect the evolution of one kilogram of this isotope within the core. The ORIGEN output is then parsed and placed in the appropriate libraries for usage by the burnup model. These ORIGEN runs are performed for all nuclides in the core. Naturally, if one were to use initial ORIGEN libraries for a different reactor type, then the tables and matrices generated here would be representative of this other reactor. These libraries only need to be generated once for a given reactor type, geometry and representative fuel composition.

In addition, the representative cycle-average neutron energy spectrum changes with BUd. This is because more initial fissile fuel is needed to achieve increased burnups. Even for an identical fuel to coolant volume ratio the spectral dependence on burnup is often too large to neglect. Thus for thermal-spectrum systems ORIGEN input libraries are prepared for a number of differing BUds. For PWRs libraries representative of 20, 33 and 50 MWd/kgIHM discharge burnups have been used. These libraries are interpolated to create customized libraries at any burnup in this range. They thus capture the dependence of the cycle-average cross sections on discharge fluence and initial isotopics. This is of more significance to PWRs as fast reactor spectra are relatively more stable. To investigate high-burnup PWR fuels additional libraries for BUd of 70 and 100 MWd/kgIHM have been prepared using assumed initial ^{235}U enrichments of 5.5 and 8 w/o, respectively.

Even systems whose spectra are less sensitive to initial composition and burnup must be treated using a number of cross section libraries prepared from

detailed transport calculations. For the sodium-cooled FR design a number of libraries are available. Distinct sets of libraries were prepared for 0.5 (used in this study) and 0.25 target conversion ratio cores. Additionally, separate libraries were prepared at each conversion ratio for fuels with higher and lower minor actinide (MA) content. The higher MA case is representative of the feed to a FR if Pu from used UOX is first burned in MOX, while the lower MA library, the one used in this study, reflects the TRU content with no MOX burn.

2.2.4.1 Hydrogen Cross Section Rescaling

The one group cross sections are functions of fuel burnup and therefore fluence, in some cases quite strongly so. The model supports the adjustment of ^{1}H cross sections, production and destruction rates, and transmutation rates as a function of fluence. For instance, the effective one group radiative capture cross section of ^{1}H in typical PWR coolant changes significantly as the flux spectrum in the core evolves to maintain constant power density. Just as with the interpolation of the ORIGEN input libraries, the hydrogen cross section may be parameterized around the burnup that the core has experienced. Moreover, hydrogen contributes about 10% to the total destruction rate in the core. Thus a significant change in the hydrogen cross section could yield an appreciable error in the model as formulated above. What follows is more of an adjustment to the hydrogen one-group cross section than a true multi-energy group response. However, this adjustment provides an easy to

calculate model to reduce the error induced into the neutron destruction rates by non-representative hydrogen cross sections.

To account for these spectral variations an f-factor is introduced that is a function of the burnup $BU(F)$. $f(F)$ is a unitless factor by which all hydrogen destruction rates $d_H(F)$ are multiplied by in equations 2.9-2.11. Two hydrogen cross sections are known for two burnups. These were taken from the ORIGEN cross section libraries prepared for 33 and 50 MWd/kgIHM in PWRs.

Thus $f(F)$ is the computed by drawing the line between these two points and dividing it by the cross section that was used for the ORIGEN runs. Since ORIGEN was run using the 33 MWd/kgIHM library, the line is simply divided by 0.03474 barns. The equation for $f(F)$ is therefore,

$$f(F) = 1.36927 - 0.01119 \cdot BU(F) \tag{2.18}$$

As is seen in this extrapolation, the per atom hydrogen neutron destruction rate can vary considerably. Multiplying $f(F)$ by $d_H(F)$ results in an increase of the accuracy of all destruction rate and multiplication factor data that is computed. The inclusion of the hydrogen rescaling factor and subsequent effects on BUd and initial compositions will be discussed in a later section with regards to the example of standard PWRs.

2.3 Fuel Cycles

The AFC R&D plan for domestic fuel cycles offers many possible pathways. With most of these options AFC R&D hopes to reduce the stockpile of United States transuranics (TRU) and obviate the technical need for a second repository during this century. Separated transuranics are moreover seen as dangerous to nuclear non-proliferation goals. Furthermore, most TRU species negatively impact repository performance as compared to an equivalent mass of natural uranium (NU). Two fuel cycles involving recycle - uranium recycle in PWRs and full TRU recycle in FRs - are examined here as case studies to which the method presented above is applied.

2.3.1 Uranium Recycle Fuel Cycle

The first of the fuel cycles that are analyzed here explores blending of RU with enriched NU to achieve sustained uranium recycle in light water reactors (LWR). Since RU is a product of reprocessing light water reactor used fuel (LWR UF), the front end for the RU creation process includes the back end of the reprocessing based LWR-NU fuel cycle. The application of the burnup model to the RU burning reactor will be demonstrated through the study of this fuel cycle.

Figure 2.8 depicts the RU blending option studied here. Red arrows in Figure 2.8 connote RU flow stemming from the UREX+ reprocessing component or the enrichment component. Black arrows that lead out of components indicate flows that do not comprise the mass input streams to the RU burning

reactor. Blending RU with enriched natural uranium is a method of increasing

Figure 2.8: RU Fuel Cycle
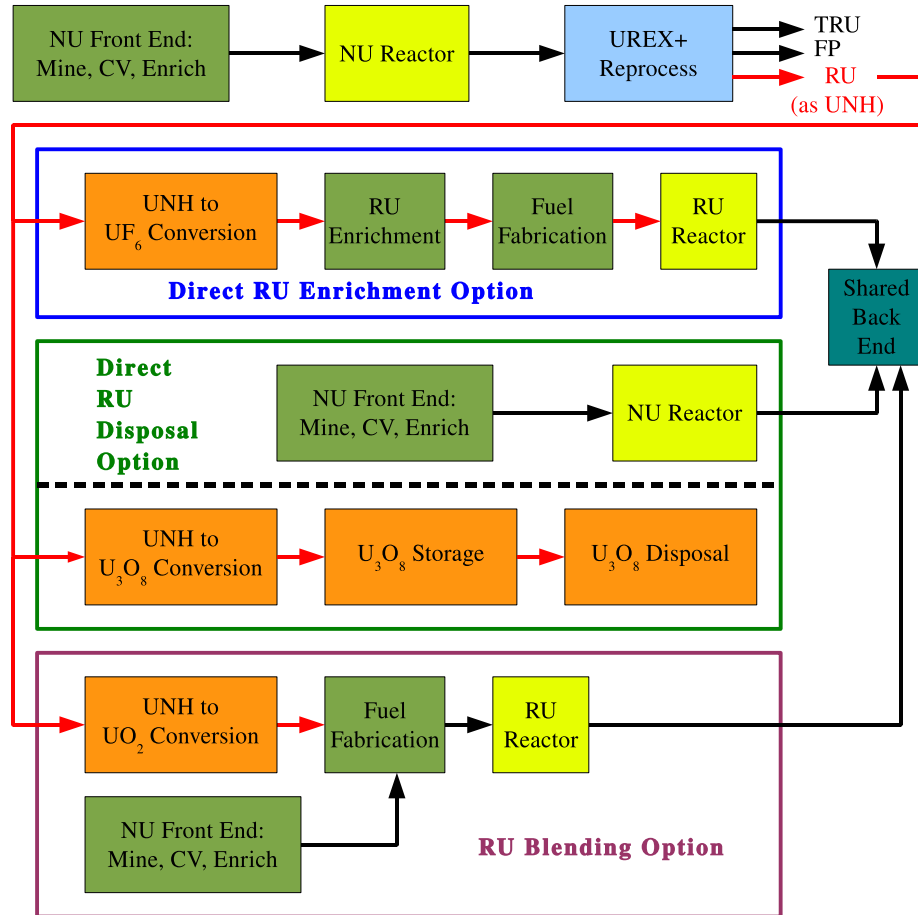
the fissile content of the RU while also impeding the buildup of ^{236}U, a neutron poison. From the standpoint of the fuel cycle material balance alone, if the utilization of RU is to be maximized the best material to serve as a blend stock with RU is highly enriched uranium (HEU). HEU is in limited supply as a blend stock and its use for civilian applications is undesirable. Therefore

if the blending strategy is to be implemented, the blend stock would be low enriched uranium (LEU).

LWR UF contains a higher enrichment of ^{235}U than NU; therefore RU blending may be economically advantageous over the once-through fuel cycle given that reprocessing is already taking place to recover TRU. The weight percent of ^{235}U in the legacy used fuel of the United States is between 0.8-0.9% [32]. However, LWR UF also has non-negligible amounts of ^{236}U bred into it, between 0.3-0.5%. As ^{236}U is a neutron poison, the advantage of the extra ^{235}U in RU is not immediately quantitatively obvious. Therefore, to increase the fissile content of an RU fuel form, it is blended with LEU. This LEU blend stock serves to dilute the ^{236}U and thereby decrease its negative impact on the neutron balance in the core.

Fuel that goes into the RU reactor must be assigned a target burnup; for reasons of simplicity and practicality, it will be assumed that it is desirable to achieve parity between the traditional LEU- and RU-bearing fuel burnups. Since the RU isotopic composition is set by the burnup in the initial reactor, the free parameters that are used to match the burnup of RU fuel to that of virgin LEU fuel in the reactor are the LEU enrichment and its mass fraction in the blended LEU-RU stream.

The first blending option is that the mass of LEU blend stock per unit mass of RU is held constant. Thus the fissile content of the RU-bearing fuel is controlled by the enrichment of the LEU. On the other hand, the LEU enrichment can be held constant and the mass that is mixed with the RU may

be varied. In this second case the LEU enrichment may be up to 19.9%.

It should be noted that higher LEU enrichment levels mean that more RU can be blended in. Near-future enrichment plants will not be licensed to produce LEU at greater than 8% ^{235}U enrichment. However, the LEU/HEU limit is 19.9% so it is conceivable that if RU recycle came to fruition civilian enrichment facilities would be allowed to manufacture 19.9% enriched product.

2.3.2   Fast Burner Reactor Fuel Cycle

A fuel cycle which features sustained TRU recycle is the second one examined. The basis of the model used here is a fast reactor (FR) with LWR UF top up. The purpose of this fuel cycle option is to reduce the global actinide inventory per unit energy as compared to the standard once-through fuel cycle, with the specific aim of reducing transuranics. To this end, the FR conversion ratio (CR) is less than unity. The nominal value for the conversion ratio in this study is taken to be 0.5, consistent with the baseline sodium-cooled fast transmuting reactor point design used in AFC R&D scoping studies [1].

Figure 2.9 depicts the FR fuel cycle that is studied. Once again, mass flows represented in red are the four mass streams that form the FR fresh fuel blend stock. The mass of each stream relative to the others may be varied by the burnup model to achieve a target burnup. The mass flows in black are the flows that are considered static to the burnup model and are not changed, though they may vary with fuel cycle pass number.

Because of the dynamic nature of the burnup model, the discharge

36

Figure 2.9: FR Fuel Cycle
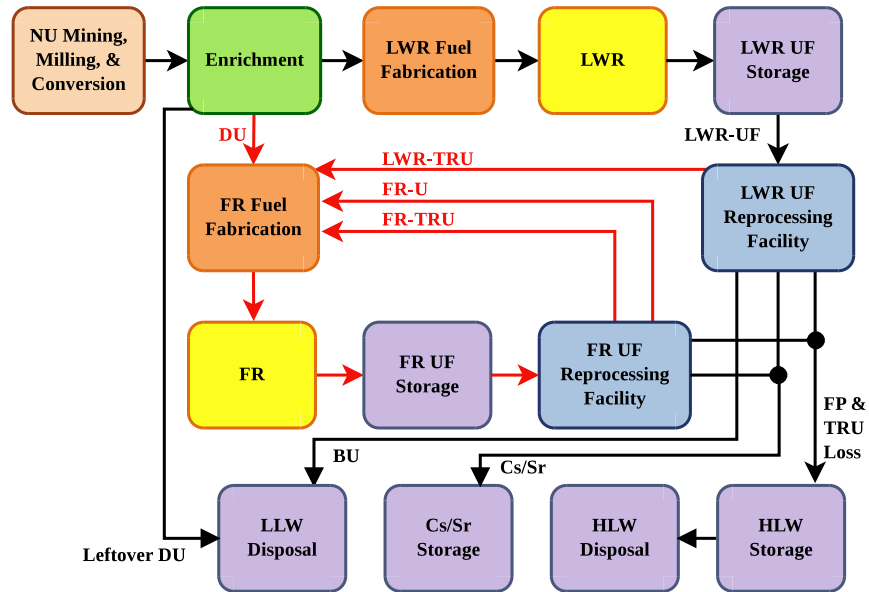
burnup is not fixed but rather a target BUd is set as a parameter within the model. Alteration of the BUd will change the balance of the FR input mass streams as well as all dependent isotopics. However, burnup values of 51 MWd/kg for the LWR and 170 MWd/kg for the FR are used unless otherwise stated. Both of these values were taken from the VISION [11] specifications for nominal LWR and FR cases. Similarly, used fuel from both the LWRs and FRs is allowed to cool for a time before being reprocessed. The time that used fuel of any sort is allowed to cool also affects the isotopics and mass stream material balances. The cooling time is again a parameter that may be specified within the fuel cycle model for which nominal values were taken here.

The input mass to the fast reactor is made up of four independent

37

streams: depleted uranium coming from the tails of enrichment (DU), the transuranics coming from light water reactors (LWR-TRU), the uranium coming from fast reactors (FR-U), the transuranics coming from fast reactors (FR-TRU). These streams are separated in the reprocessing facilities and then combined to form the input stream to the fast reactor. The fission products from these streams are also removed from the fuel at this point and sent off to a disposal facility.

It should be noted here that the reprocessing facility that deals with the light water reactor used fuel (LWR UF) and the reprocessing facility that handles the fast reactor used fuel (FR UF) would likely be collocated.

Lastly, Figure 2.9 represents a closed fuel cycle which implies that actinides may be recycled indefinitely or until they are eventually burned. The constraint is that there exist enough FRs to handle the mass throughput. As no separation process is perfect, some small actinide mass will be mixed with the fission products after reprocessing and be sent to the repository. It is known that the reprocessing separation efficiencies ultimately affect repository performance [46]. However, because the isotopics change with every pass of TRU through the fuel cycle, there arises a mass stream feedback between the reactor burnup, the cooling time, and the reprocessing efficiencies. The burnup model handles such feedback effects with ease.

The implication of a closed or partially closed fuel cycle is that mass may be sent through many recycles. For a specific target FR burnup and other fuel cycle parameters, the relative masses and the isotopics of the four mass

streams (DU, LWR-TRU, FR-U, FR-TRU) may change significantly as a function of pass number. However, one would eventually expect that equilibrium values for the mass balances and isotopics will be reached. Typically, such an equilibrium state is indeed obtained. For some species though, equilibrium is not reached even after many recycles. In practice many decades, even centuries, would elapse before an equilibrium scenario result would reflect reality. Therefore, equilibrium fuel cycle simulation results must be interpreted with caution. When equilibrium is achieved and how it is defined is discussed in a later section.

2.3.3 Cooling Model

Before reprocessing occurs, light water reactor used fuel (LWR UF) and fast reactor used fuel (FR UF) are typically stored and cooled. This process represents the "Storage" boxes in fuel cycle Figures 2.8 & 2.9. The cooling model computes the analytical solutions to the Bateman equations [41]:

$$m_j(t_C) = (m_1 \gamma_1 \lambda_1 \gamma_2 \lambda_2 \cdots \gamma_{j-1} \lambda_{j-1}) \sum_{g=h}^{j} \left[\frac{e^{-\lambda_g t_C}}{\prod_{k=h, k \neq g}^{j}} (\lambda_k - \lambda_g) \right] \quad \text{for } 1 < j$$

(2.19)

Here, t_C [years] is the time that the UF spends in storage cooling, $m_j(t_C)$ [kg] is the mass of the jth daughter of the parent species with mass m_1 [kg]. The λs [1/years] are the decay constants for the respective nuclides in the decay chain. The γs are the branch ratios that correspond to each decay constant for this decay chain.

Finally, these results are sent to the reprocessing model (where separa-

tion efficiencies are applied), output parameters are recorded, and (for the FR case) the next cycle starts.

2.4   Fuel Cycle Model Benchmarking & Results

The fuel cycle model is the computational wrapper that executes much of the calculation and analysis. The fuel cycles that are studied are specified by a large set of inputs extending to the various intrinsic parameters of the reactors that comprise it. For example, the P_{NL} of different reactors are specific to the underlying design and neutron transport characteristics. Other parameters include the target burnup, the amount of time that UF spends in storage cooling, and the fuel cell specifications that are used. Values for these parameters that were used in this study are presented in Table 2.1. Knowing this information, the fuel cycle model wraps around the reactor burnup model and invokes it when input streams need to be mixed or used fuel compositions must be found. The fuel cycle model then sends the results of the burnup model to the next fuel cycle component (as seen in Figures 2.8 & 2.9). Thus the fuel cycle model coupled with the burnup model developed here produce unique, physics-based values for the material balances for one or many recycle passes. This represents an advantage over recipe based simulations which are not able to alter any of the input parameters at will. In this model all inputs are allowed to change simultaneously.

It is important to point out that the burnup model is sensitive to the input parameters specified in Table 2.1. To select the non-leakage probability

Table 2.1: Reactor Parameter Specification

Parameter	LWR	FR
Target BUd [MWd/kgIHM]	51	170
Non-Leakage Probability, P_{NL}	0.98	0.65
Number of Fuel Batches, B	3	3
Fuel Density, ρ^F [g/cm3]	10.7	18.0
Coolant Density, ρ^C [g/cm3]	0.73	0.927
Fuel Cell Side Length, ℓ [cm]	1.3127	0.956
Fuel Radius, r [cm]	0.410	0.3115
Cladding Outer Radius, r_o [cm]	0.475	-
Total Fuel Pin Slots per Assembly, S_T	289	163
Open Fuel Pin Slots per Assembly, S_O	25	19
Cooling Time, t_C [years]	10	10
Fraction of LWR UF that is TRU, LWRtruF	0.01288	-
Convergent Isotopes for Equilibrium, Iso2Cvg	-	^{239}Pu, ^{240}Pu, ^{242}Pu
Uranium Separation Efficiency	0.99	0.99
Neptunium Separation Efficiency	0.99	0.99
Plutonium Separation Efficiency	0.99	0.99
Americium Separation Efficiency	0.99	0.99
Curium Separation Efficiency	0.99	0.99

P_{NL} and calibrate the model, enrichment and burnup combinations were taken from VISION [11] libraries for LEU for a 3 batch core. By thinly varying P_{NL} and the coolant density ρ^C [g/cm^3] and toggling the f-factor correlating cycle-average hydrogen cross sections with discharge burnup a wide range of enrichment values were generated. These are presented in Table 2.2 along with benchmark enrichment/burnup values taken from two other sources. The parameter set H was eventually chosen for the actual model as it most closely represents reality and the VISION targets. Note that the enrichment is in weight percent ^{235}U and BUd is in units of [MWd/kgIHM]. This calibration must be performed for each reactor system to be analyzed.

Table 2.2: Burnup Model Input Parameters for LWRs

Label	P_{NL}	ρ^C	f used?	%^{235}U at BUd=33	%^{235}U at BUd=51
VISION [11]				3.2	4.3
ORNL [22]					4.26 @ BUd=50
OECD [43]				3.6 @ BUd=40	
A	0.98	1.00	yes	3.38	4.85
B	0.98	1.00	no	3.29	4.89
C	1.00	1.00	yes	3.22	4.54
D	1.00	1.00	no	3.07	4.50
E	1.00	0.73	yes	2.88	4.21
F	1.00	0.73	no	2.77	4.23
G	0.95	0.73	yes	3.48	5.00
H (used)	0.98	0.73	yes	3.12	4.49
I	0.98	0.73	no	3.05	4.51

A series of benchmarks were carried out to verify both the fresh fuel composition and fuel burnup calculations. The OECD Burnup Credit Criti-

cality Benchmark [43] series is a composite of many international studies using independent, high fidelity neutronics codes acting on the same specifications. The study selected for benchmarking, Phase I for PWRs, uses an initial fuel vector (3.6 w/o ^{235}U with trace amounts of ^{234}U and ^{236}U) that is burned to 40 MWd/kg. The study lists output isotopics at various stages during the burn and post-removal cooling.

To benchmark the burnup algorithm developed here, the initial fuel vector and burn parameters are taken from the study but "generic" PWR cross section sets were used. In other words, the cross sections developed for a reference 17x17 PWR lattice were used with the burnup model and detailed transport calculations to create customized cross section sets for the benchmark case were not carried out. This situation reflects the procedure that might actually be carried in a fuel cycle scoping calculation, where it is desirable to treat all reactors of a single general type as represented by a generic archetype. Table 2.3 compares the computed isotopics to the isotopic vector reported in the OECD study for a 40 MWd/kgIHM burn with no cooling. The table also shows the standard deviation of the collected results for the 21 participants in the Phase-IB study. All values are given in terms of weight percent of initial heavy metal. These results show that the present method matches the Burnup Credit within two standard deviations for most actinides. The only species showing a much larger relative departure is ^{241}Am. ^{241}Am is formed almost exclusively through ^{241}Pu decay and there are two reasons for this departure. First, the fluence-dependent isotopic transformation matrices

Table 2.3: Isotopic Benchmark of the OECD Burnup Credit [43] to This Method

Isotope	OECD [43] [w/o]	σ of OECD [%]	Results [w/o]	% Difference
^{234}U	0.0178	9.0	0.0184	+3.6
^{235}U	0.8001	8.1	0.7079	-11.5
^{236}U	0.4840	2.6	0.4781	-1.2
^{238}U	93.3333	0.2	93.6109	+0.3
^{237}Np	0.0614	9.4	0.0584	-5.0
^{238}Pu	0.0226	13.9	0.0185	-18.1
^{239}Pu	0.5991	7.1	0.5104	+14.8
^{240}Pu	0.2389	5.3	0.2591	+8.5
^{241}Pu	0.1636	6.9	0.1445	-11.7
^{242}Pu	0.0602	8.4	0.0563	-6.5
^{241}Am	0.0047	5.3	0.0032	-30.8
^{243}Am	0.0148	10.4	0.0116	-21.3

were assembled using a constant flux 4×10^{14} [n/cm^2/s] that is representative of most PWRs. If the average flux and power density are somewhat lower, and hence the irradiation time is somewhat longer as is the case here, the model will under predict the ^{241}Am buildup in the core. Second, the model does not explicitly treat refueling downtimes when transmutation ceases but decay continues. Note that the deviation in long-term ^{241}Am content is smaller because the concentration of the much more abundant parent, ^{241}Pu, is reasonably accurate.

It is also necessary to benchmark the feed stream blending and discharge burnup calculations. This is best achieved in the context of a comparative fuel cycle material balance. Material balances of this type generated using

the high-fidelity material balance simulation package COSI [5] are available in a number of OECD systems studies [24]. A benchmark of the equilibrium material balance for a PWR/FR fleet has been carried out. In this benchmark, the methodology described here is used to find the enrichment of PWR fuel to achieve a specified burnup as well as to derive the equilibrium FR fresh and used fuel compositions through the cycle iteration procedure described above. Specific results benchmarked included the PWR/FR thermal power split, the isotopic composition of the burned fuel, and the fuel cycle cost derived from the material balance flowsheets.

2.4.1 The Recyclable Uranium Fuel Cycle

The RU fuel cycle described does not preclude multi-recycle of transuranics. Instead it focuses only upon the uranium component of an integrated recycle strategy. Moreover, for purposes of illustration only the first uranium recycle pass is considered. A second example applying the burnup model to a dynamic case will be covered in the FR fuel cycle section.

To further characterize what is happening in the burnup model, it is of interest to characterize the isotopic breakdown of the neutron production and destruction rates in the core. To do so, one simple case is considered.

For this illustrative case the ^{235}U enrichment is chosen at 4.0%, while the ^{236}U enrichment is set to 1.5%. Three batch fuel management is assumed and a graph of BU(F) is made in analogy to Figure 2.5. The discharge burnup BUd of this fuel is not known *a priori* but it is instead calculated via the burnup

model that was described above. BUd was calculated to be approximately 37 MWd/kgIHM. Figures 2.10-2.13 show the computed core-average neutron production and destruction rates for burnups of 0, 1/3 BUd, 2/3 BUd, and BUd. Zero burnup here indicates the neutron production and destruction rates for fresh fuel that has just been loaded into the reactor.

It is crucial to note that the production and destruction rates of the species shown in these figures reflect the isotope and all of its daughters. For example, by the end of life, most of the neutrons are coming from ^{238}U and its daughters. In fact very few neutrons are spawned from ^{238}U itself, but rather from its daughter ^{239}Pu. Similarly, by the time the fuel has reached BUd much of the ^{235}U has already burned off. These figures show that the neutron balance is well represented by a mass-weighted linear combination of initial isotopics; therefore the fluence dependent balance depends strongly on initial composition of the fuel. To scope the merit of RU blending strategies, It has been found to be useful to parameterize discharge burnups of RU-bearing fuels around this dependence.

To accomplish this the achievable burnup is parameterized as a function of the fresh fuel initial ^{235}U content, initial ^{236}U content, and the number of batches in the fuel management scheme. Note that given this small number of degrees of freedom, the whole parameter space may be comprehensively mapped. Therefore the discharge burnup can be found as a function of these three variables (^{235}U%, ^{236}U%, B). With the FRs, finding such a parameterization would be bulky and unwieldy if even computable. Moreover, it would

Figure 2.10: Neutron Production and Destruction Rates for a Sample RU Fuel with Isotopic Breakdown at Near Zero Burnup for PWRs

47
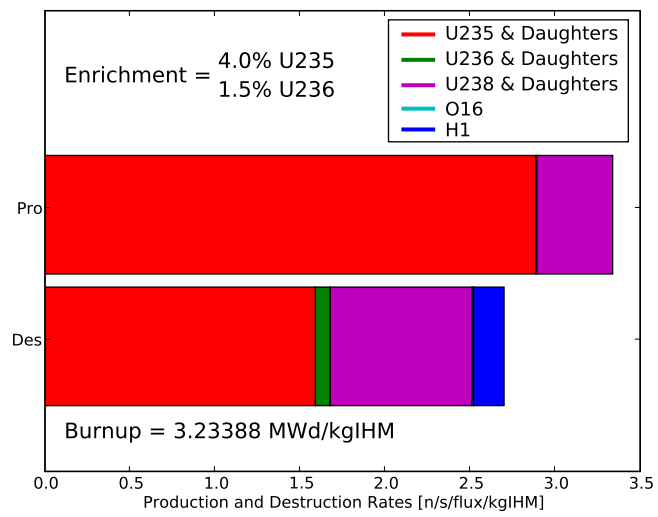
Figure 2.11: Neutron Production and Destruction Rates for a Sample RU Fuel with Isotopic Breakdown at 1/3 BUd for PWRs
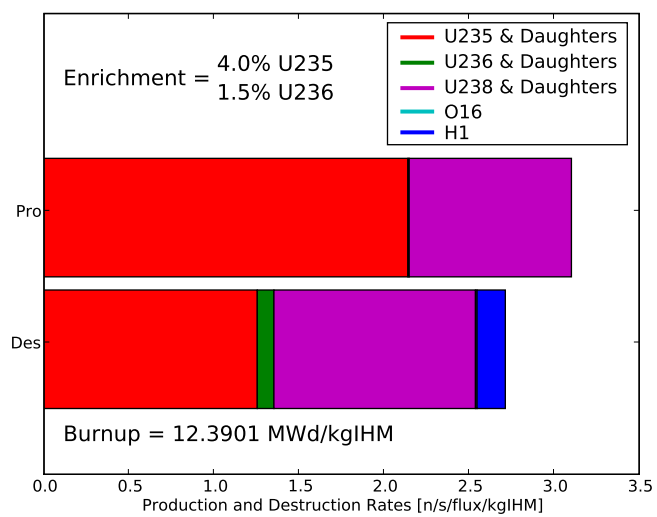
Figure 2.12: Neutron Production and Destruction Rates for a Sample RU Fuel with Isotopic Breakdown at 2/3 BUd for PWRs
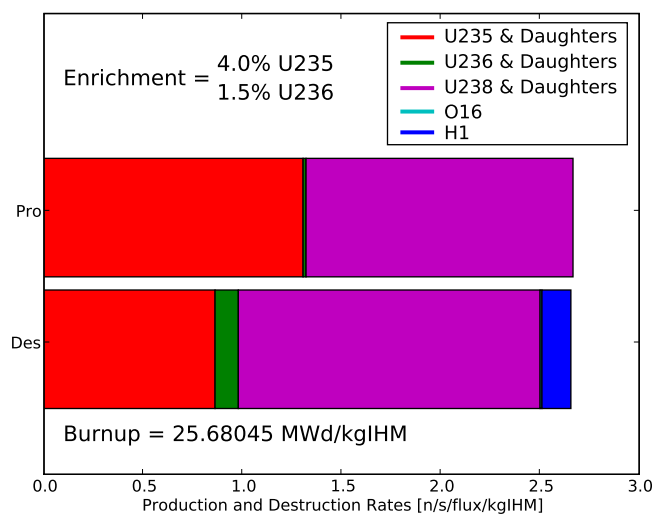
Figure 2.13: Neutron Production and Destruction Rates for a Sample RU Fuel
with Isotopic Breakdown at BUd for PWRs
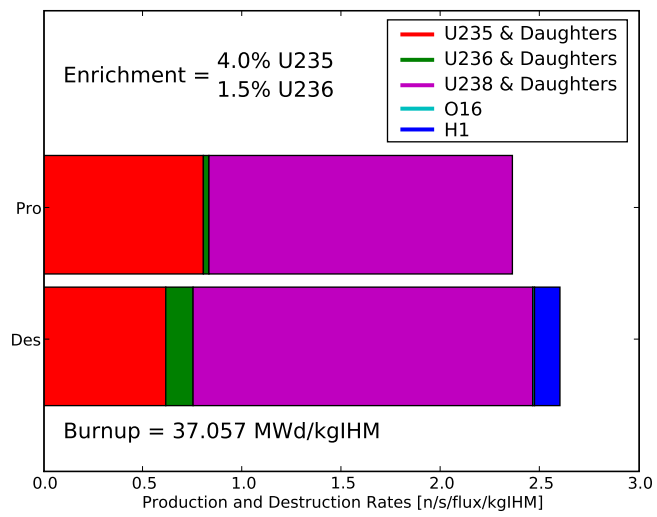
be prohibitive to try to do so for FRs since the parameter space of initial isotopes is larger by at least an order of magnitude.

The functional form of the equation that gives BUd is shown in equation 2.20. In this equation, BUd is the discharge burnup achievable [MWd/kgIHM], x is the weight percent of ^{235}U in the fresh fuel [(w/o)IHM], y is the weight percent of ^{236}U in the fresh fuel [(w/o)IHM], and B is the number of batches. All other letters appearing in equation 2.20 are parameters of the fit and have units appropriate to their placement. The values of these parameters that were obtained for the data set generated are given in Table 2.4.

$$\text{BUd}(x, y, B) = \frac{2B}{B+1} \cdot (j(x-h)^m + s \cdot y + t \cdot x + k) \qquad (2.20)$$

Table 2.4: Parametric Values for Burnup Model Fit for RU Burning LWRs

Parameter	Value
j	17.5
h	2.0
m	0.7
s	-2.5
t	-1.75
k	8.2

In equation 2.20, fit parameters and the dependent variables are based on physical meanings. First, the $2B/(B+1)$ dependence of BUd comes directly from the results of a linear reactivity model with the core burnup being an independent variable when calculating the reactivity. The proof of this dependence and its physicality are given in [8]. Moreover, the $j(x-h)m$ term

51

comes from the fact that the major trend for burnup follows a power law. One expects that the burnup would, as a function of fluence, asymptotically approach the maximum possible burnup (931.46 MWd/kgIHM). However, the power law, with $m < 1$, seen here is a good approximation for the relatively low burnups achieved in PWRs. j scales this term up to the valid burnup range and h slides the burnup over to the ^{235}U enrichment under which burning is not feasible.

Furthermore, at a given ^{235}U enrichment, BUd is seen to have a near-linear dependence upon ^{236}U content. Because the ^{236}U is a poison and is present in relatively small amounts, incremental changes in its enrichment yield matching changes in the burnup. More explicitly, s determines how much a given ^{236}U content affects the burnup. Additionally, s is negative because ^{236}U only destroys neutrons and does not directly increase the energy gained from the fuel per atom IHM. However, BUd also decreases linearly with the ^{235}U content. The tx term is a correction factor to the power law term. It slightly weights lower ^{235}U enrichments preferentially to higher burnups. This term exists because there is ^{236}U present. This term captures the poisoning effect of ^{236}U; with increased ^{236}U more ^{235}U is needed to achieve a given burnup. Lastly, the constant k term scales up the burnup to the appropriate base value.

Thus equation 2.20 satisfies the requirements of fitting the maximum discharge burnup data to ^{235}U content, ^{236}U content, and the total number of batches while having a physical interpretation.

Figures 2.14 & 2.15 show how the closed form equation with the given

parameters fits to the actual data that was generated for three and six batch cores respectively. These figures show that the fit with the data is quite good for ^{235}U enrichments between 2 - 6% and ^{236}U content from 0 - 4.5%. Having such a fit equation is useful as it allows for the near instant calculation of the burnup for a PWR bearing RU fuel.

There is a large advantage to this with respect to the RU fuel cycle. Recall that the fuel cycle model mixes an RU stream from LWR UF and an enriched NU stream. Thus using Equation 19, the maximum achievable burnup of the mixed fuel can be found with ease and without resorting to a lengthy calculation or resubmitting the relevant data to the burnup model. Moreover, given the ^{236}U enrichment, the number of batches, and a target burnup, the fit equation can then be easily iterated to find the ^{235}U enrichment required.

In Figure 2.16 the ^{236}U is held at a constant 1% while the number of batches is allowed to vary. Note that in all three of these figures the low burnups do not fit as well to equation 2.20. However, this region of discharge burnups of less than 20 MWd/kgIHM is of low concern for PWRs. Moreover, as a function of batch number Equation 19 fits very well to all cases save the unlikely single batch case.

Lastly, fuel cycle material balances may be expediently generated. As an example case, set the target burnups of the RU- and NU-burning reactors to 51 MWd/kgIHM. As discussed above, either the relative mass of RU/LEU or the LEU enrichment may be the free variable. Allowing the LEU enrichment

Figure 2.14: Burnup Model Fit with Data for 3 Batch Core for LWRs
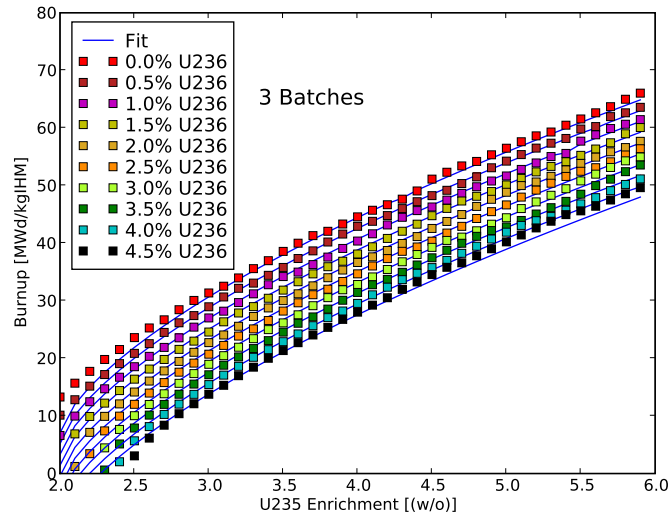
Figure 2.15: Burnup Model Fit with Data for 6 Batch Core for LWRs
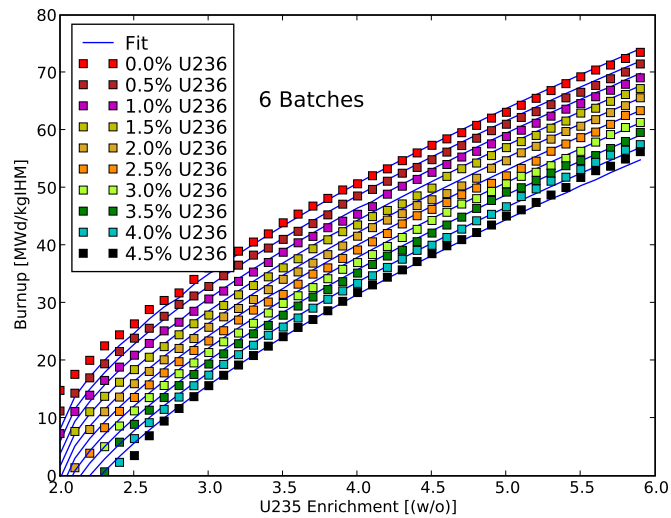
Figure 2.16: Burnup Model Fit with Data for 1% ^{236}U for LWRs
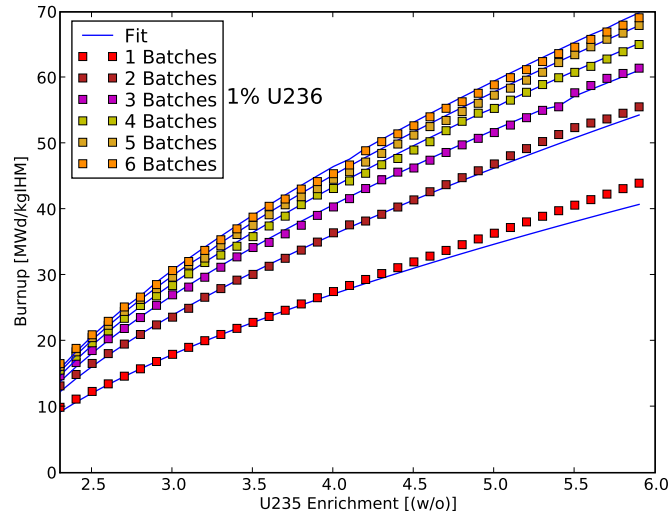
to be free and the mass of RU and LEU to be blended is the same, Figure 2.17 shows the mass balance of the fuel cycle just defined and it can be seen that the LEU enrichment needed to obtain the target burnup for the blended fuel is 8.5%. Note that this figure is in analogy to Figure 2.8, but with mass stream values included. Moreover, Figure 2.17 is normalized to 1 kgIHM in the RU reactor.

2.4.2 The Fast Reactor Fuel Cycle

A walkthrough follows of how to apply the burnup model algorithm to the closed fast reactor system described above. The first time a fast reactor system comes on-line, there exists no FR-U and FR-TRU streams from prior

Figure 2.17: Sample RU Fuel Cycle Mass Balance
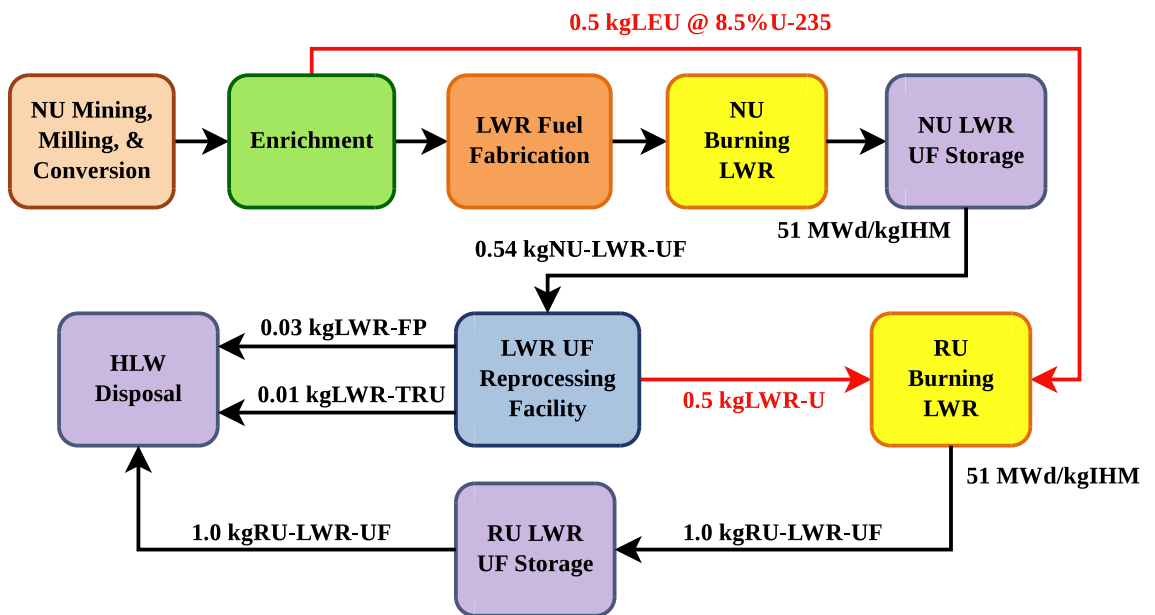
cycles so these mass flows and compositions are set to zero. This leaves only reprocessed DU and LWR-TRU streams to be mixed in order to obtain the burnup value specified for the fast reactor. These two parameters reduce to only one variable since DU = 1 - LWR-TRU. Therefore the system has only one degree of freedom.

It should be noted here that the DU and LWR-TRU internal isotopic compositions remain constant over all fuel cycle passes through the fast reactor. This is because the LWR burnup remains the same and thus identical LWR UF is always used to top up the fast reactor.

To obtain the DU/LWR-TRU ratio that achieves the target burnup, an initial guess of the ratio is made. This resulting fuel is then sent to the burnup model and maximum discharge burnup is calculated. A root finding method is then used to iterate over the ratio and BUd until a proportion of DU/LWR-TRU is found that generates the target burnup. The bisection method is once again applied due to its usefulness with regards to pointwise approximations of continuous data.

Two initial conditions are first calculated for the bisection method to be used. Firstly, a BUd is calculated (via the burnup model) for a fuel that is composed of entirely LWR-TRU. If this is not a valid fuel form (as discussed above) then an incremental amount of DU is added until a valid, burnable form is reached. The second initial condition is just the inverse. A BUd is found for a fuel that is primarily or all DU. These two conditions serve to bound the range of available burnups for the FR fresh fuel. If the FR

target burnup is outside of this range, then the remainder of the calculation is impossible. Otherwise, the bisection method may be applied with these two starting conditions. Upon reaching the target burnup, the amount of DU and LWR-TRU that go into the fast reactor on the first pass of the FR fuel cycle is now known.

The isotopic output of this first fast reactor burn is then sent to the cooling model. After the FR UF has been decayed for the appropriate amount of time the reprocessing separation efficiencies are applied. These separation efficiencies are set initially and are constant for the entire fuel cycle, although they may vary between individual chemical elements. Fuel cycle parameters are now calculated and recorded. This concludes the first cycle pass through the fast reactor.

The second and further passes proceed similarly to the first. However unlike in the first pass, the four mass streams (DU, LWR-TRU, FR-U, and FR-TRU) now all exist as the FR-TRU and U discharged from the fast burner will be reloaded in the next cycle. However, FRs convert 15-20% of their initial actinide mass into fission products over the course of their burn and considerable top-up of DU and LWR-TRU streams will be required.

However, the same problem remains as in the first pass case. The DU/LWR-TRU proportion that generates a burnup that equals the target burnup is not known *a priori*. Thus the same strategy that was used in the first cycle is employed to find this proportion. Once again, two guesses are made as to what the relative fractions are. These bound the burnups available

and the bisection method is applied to calculate the DU/LWR-TRU ratio that hits the target burnup.

Now that the target burnup has been reached and the fresh fuel burned, it becomes used fuel once more. The FR UF is again stored and cooled. These results are then sent to the reprocessing code where the separation efficiencies are applied. Fuel cycle parameters that are specific to this pass are now calculated and stored.

This process may continue indefinitely as there are an infinite number of cycles possible. However, fuel cycle parameters (such as isotopic concentrations in the fresh and used fuels, uranium and transuranic masses) typically come to "equilibrium" given enough passes through the system. Two approaches to determining equilibrium status were considered: the stabilization of certain tracked isotopes or the convergence of the FR fresh fuel transuranic fraction. This TRU fraction is tracked until it converges to within error, say a 1% change between the last cycle and the next-to-last cycle at which time equilibrium is declared. The advantage of this method is that, for all practical applications, it ensures that the four input mass streams have all converged on their own and the mass balance is in near-equilibrium.

If the fuel cycle study is concerned with the prevalence of isotopes having, for instance, a strong effect on repository performance it is wiser to develop a list of important species whose convergence is to be tracked. Then at the start of each pass after the first, the change of these isotopic concentrations in the used fuel is calculated. If all isotopes in the list have converged to

59

within some allotted error (perhaps 1%), then the fuel cycle as a whole is said to have converged. In the FR case considered here, ^{239}Pu, ^{240}Pu, and ^{242}Pu dominate the TRU by mass and converge after only a few cycles. Moreover, ^{242}Pu is the precursor isotope for production of most of the trans-plutonium elements. Even though other actinides affect the FR burnup, many either do so to a lesser degree or are present in such small amounts that they do not significantly impact the neutronics of the system. However depending on the application being studied the convergence criteria may differ. For instance, the radiologically significant isotope ^{244}Cm still has not converged by the above definition, even after ten cycles.

Now that the entirety of the fuel cycle over multiple passes has been computed via the prior algorithm, a number of cycle specific parameters may be calculated. The following example data was all produced using LWR UF isotopic vectors from VISION [11]. Moreover the following table displays initial parameters input into the computational burnup and fuel cycle models.

The first set of parameters displayed is the input fractions of the four input mass streams into the fast reactor: DU, LWR-TRU, FR-U, and FR-TRU. This is shown in Figure 2.18. The input mass of fuel into the fast reactor comes in some part from LWR used fuel (1 kg or less) and partially from recycled FR fuel. Note that all streams are normalized to 1 kgIHM for each cycle. The LWR streams here are the parameters that are explicitly iterated over in the fuel cycle model in order to achieve the target FR burnup. Note that the first cycle is comprised of only LWR used fuel (as discussed above) and then these

Figure 2.18: FR Input Mass Stream Fractions of 1 kgIHM
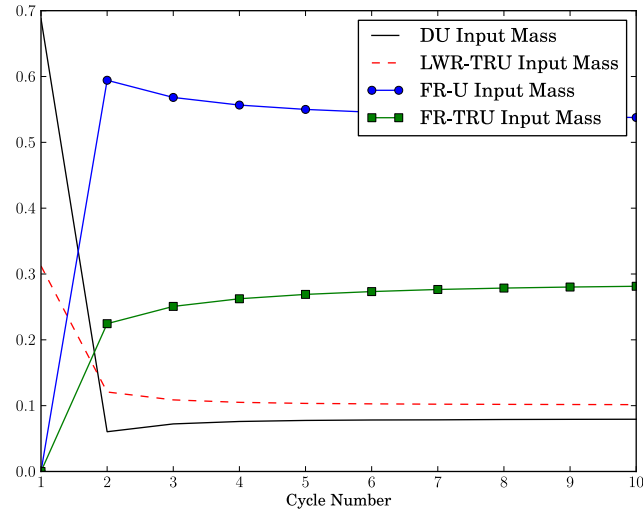
curves quickly level off. Also recall that all FR actinide mass (sans what is decayed away in storage and what is lost in reprocessing) returns to the FR on the next pass. Since the FR converts roughly 20% of its initial fuel to fission products, this explains why the sum of FR-U and FR-TRU levels off at about 0.8.

Unlike the LWRs, the fast reactor output stream is also a function of cycle number. Figure 2.19 plots the fraction of the uranium and transuranics relative to the total actinide content of the output stream. The parameters calculated here are the by-products of applying the burnup model to the fast reactor fresh fuel that was formed above.

There are various ways to define the conversion ratio of a reactor.

61

Figure 2.19: FR-U and FR-TRU Output Fractions
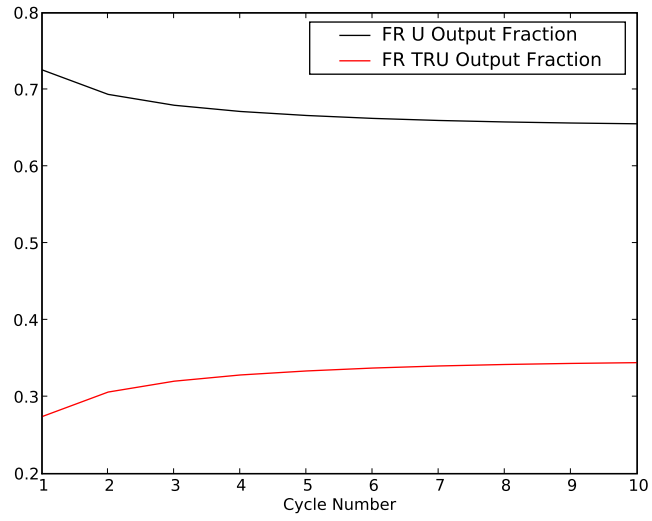
Figure 2.20: TRU Conversion Ratio
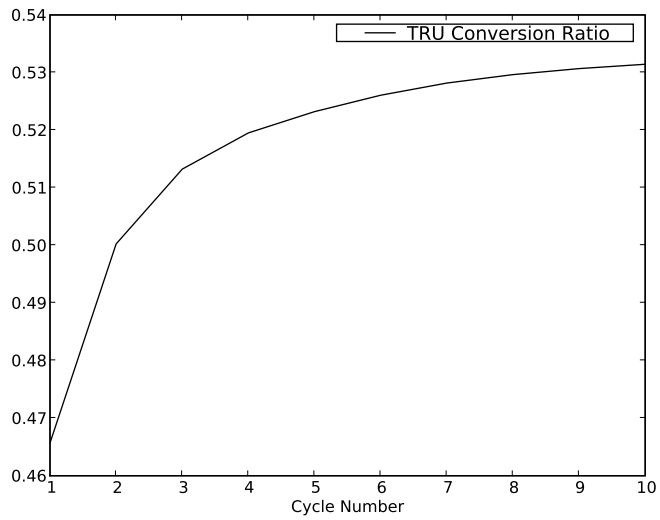
One of these is displayed in Figure 2.20. Specifically, this is known as the transuranic conversion ratio (TruCR). This is defined as one minus the change in the mass of TRU in the fast reactor core divided by the discharge burnup (BUd) of the core divided by the maximum possible burnup. Symbolically,

$$\text{TruCR} = 1 - \frac{\text{TRU}_{\text{in}} - \text{TRU}_{\text{out}}}{\frac{\text{BUd}}{\text{BU}_{\text{max}}}} = 1 - \frac{\text{TRU}_{\text{in}} - \text{TRU}_{\text{out}}}{\frac{\text{BUd}}{931.46\text{MWd/kg}}} \qquad (2.21)$$

TRU_{in} is defined as the sum of the LWR-TRU and FR-TRU streams as plotted in Figure 2.16. TRU_{out} is simply the mass of TRU in the output stream, or the FR-TRU fraction in Figure 2.19 multiplied by the actinide mass in output (80%). It should be noted that this is one of the possible ways to determine equilibrium. Waiting for the TruCR to converge is equivalent to waiting for the fast reactor fresh fuel uranium divided by the transuranic content to stabilize. More importantly, this curve does seem to equilibrate as a function of cycle number. Furthermore, the data is in the range of 0.5, which was the conversion ratio targeted for the fast reactor point design used by the burnup model.

Figure 2.21 shows the mass in kilograms of LWR UF that is required to generate the 1 kg of fuel that goes into the fast reactor. The first point will naturally be significantly higher than for subsequent cycle numbers. This is because the first cycle is made entirely of DU and recycled LWR fuel whereas other cycles use LWR UF only as top up.

Finally, individual graphs may be generated for every isotope that is tracked. The plots display the total mass of the given isotope in both the fresh (input) and used (output) fast reactor fuel streams. Note that the output

Figure 2.21: Mass of LWR UF Required for FR Fresh Fuel Top-Up
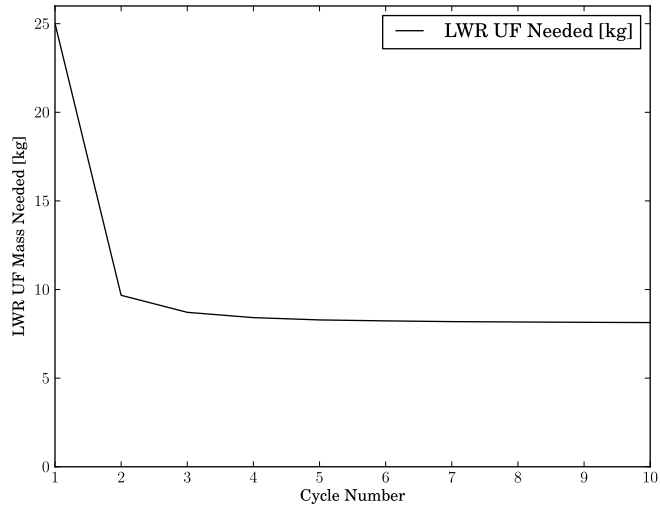
Figure 2.22: Fast Reactor Input and Output Mass Figure for ^{238}Pu
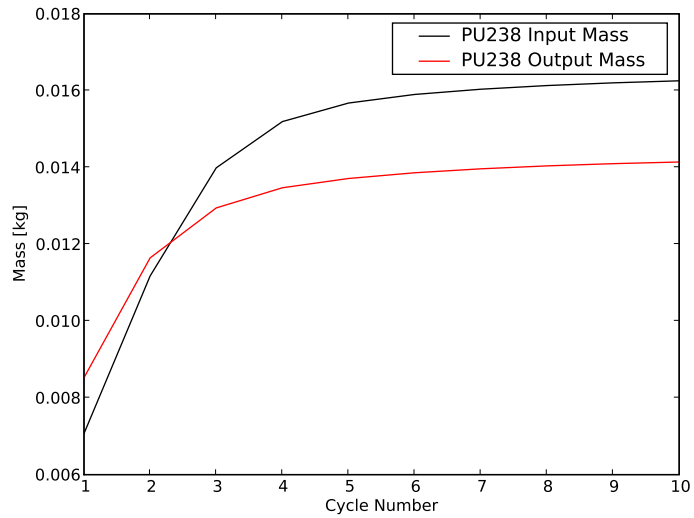
Figure 2.23: Fast Reactor Input and Output Mass Figure for ^{239}Pu
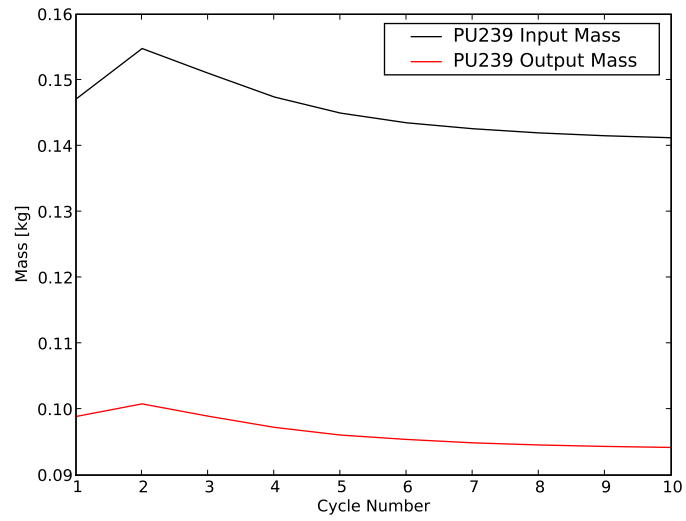
Figure 2.24: Reactor Input and Output Mass Figure for ^{240}Pu
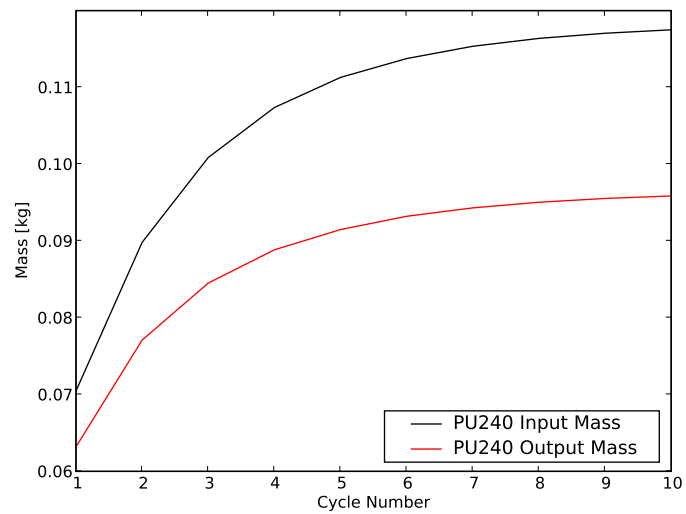
Figure 2.25: Reactor Input and Output Mass Figure for ^{244}Cm
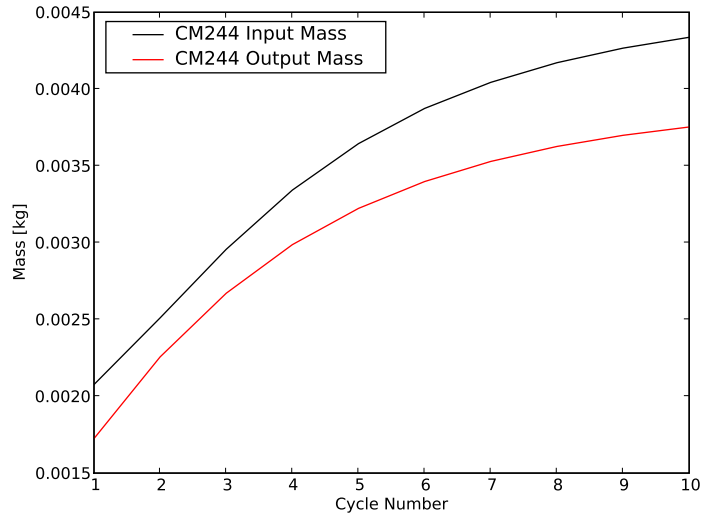
Figure 2.26: Reactor Input and Output Mass Figure for ^{246}Cm
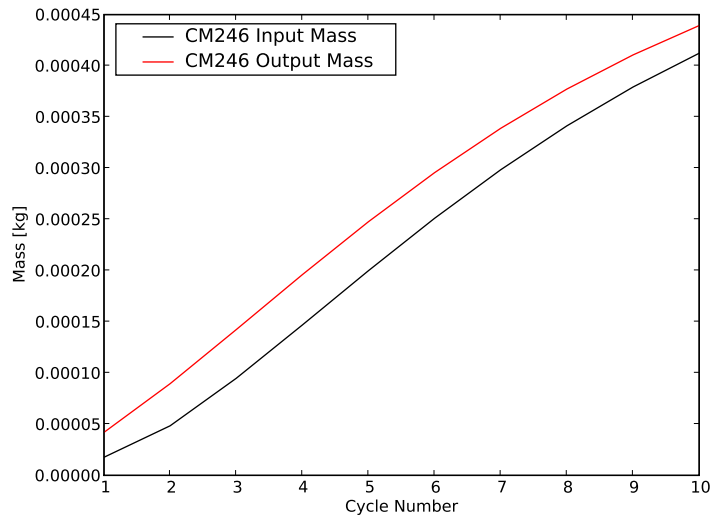
masses are given after the additional cooling time. Samples for ^{238}Pu, ^{239}Pu, ^{240}Pu, ^{244}Cm, and ^{244}Cm are shown in Figures 2.22-2.26 respectively. The plutonium figures serve to show that the system does appear to settle at an equilibrium state within the ten cycles considered here. However, the difference in the curvature of the ^{239}Pu graph to that of the ^{238}Pu and ^{240}Pu implies that the ^{239}Pu is being burned out while the other two nuclides are being bred in. Moreover, the ^{244}Cm and ^{246}Cm figures are examples of species that do not come to equilibrium after the given number of cycles. These nuclides are still being bred in via a long chain of parent species.

Table 2.5: Input and Output Concentrations into a Fast Reactor for Some Nuclides

Nuclides	1 In	1 Out	3 In	3 Out	10 In	10 Out
^{237}Np	1.48E-02	8.24E-03	1.30E-02	7.50E-03	1.16E-02	6.90E-03
^{238}Pu	7.07E-03	8.52E-03	1.40E-02	1.29E-02	1.63E-02	1.41E-02
^{239}Pu	1.47E-01	9.89E-02	1.51E-01	9.90E-02	1.41E-01	9.42E-02
^{240}Pu	7.05E-02	6.32E-02	1.01E-01	8.45E-02	1.17E-01	9.59E-02
^{241}Pu	4.26E-02	9.15E-03	2.27E-02	8.12E-03	2.26E-02	8.87E-03
^{242}Pu	2.10E-02	1.92E-02	3.04E-02	2.57E-02	3.75E-02	3.13E-02
^{241}Am	1.56E-03	1.23E-02	1.52E-02	1.58E-02	1.79E-02	1.77E-02
^{243}Am	4.81E-03	5.03E-03	8.31E-03	7.84E-03	1.19E-02	1.05E-02
^{244}Cm	2.08E-03	1.73E-03	2.96E-03	2.67E-03	4.34E-03	3.75E-03
^{245}Cm	1.39E-04	4.28E-04	6.88E-04	8.05E-04	1.25E-03	1.24E-03
^{246}Cm	1.77E-05	4.20E-05	9.48E-05	1.42E-04	4.12E-04	4.39E-04

Lastly, a numerical demonstration of this is shown in Table 2.5. This displays the input concentrations [kg$_i$/kgIHM] of selected actinides in the fresh fuel. The output values are after burning and cooling, as with the figures

above. Data is shown here for three fuel cycle pass numbers: 1, 3, and 10. Once again, it is demonstrated that convergence to equilibrium must be explicitly modeled as it will extend over many decades.

2.5 Conclusions

Given the proper the input libraries, this burnup model may be applied to nearly any reactor in any fuel cycle system. Moreover, the computational requirements are very light, with complete non-equilibrium fuel cycle material balances being generated in a few seconds.

The quickness of these burnup calculations allows for larger fuel cycle problems to be more accurately studied. Many of the variables set as static in this model may serve as future parameterizations. Iterating these may yield optimum values for various fuel cycle metrics. For example, the separation efficiencies and partitioning strategies may be changed in the FR case. This would have a significant impact on the FR-TRU stream if reprocessing efficiencies were not the same for all elements. This would not only alter the fresh fuel that the FR received, but repository performance and proliferation resistance would be affected as well.

In fact it is the very speed of the burnup model that allows the for the closed form equation that was derived for LWR performance. Calculating the hundreds of data points that went into solving for equation 2.20 would require a prohibitive amount of time using a full core transport or Monte Carlo method. Furthermore, fuel cycle studies associated with the uranium recycle strategy

could not be carried out in any meaningful sense in the absence of this kind of parameterization.

Still, this study only displayed the applicability of the burnup model to two fuel cycles. While this is important since it demonstrates that it is a useful tool for both open and closed cycles, many reactor types are available other than nominal LWRs and FRs. Furthermore, the number of fuel cycles associated with combinations of these reactors is very large. As discussed in §2.2.4, pre-computation via transport calculations of a representative set of cross section libraries will be necessary for each new coolant and fuel type that is to be studied. The representative set would span the spectral conditions to be expected in the reactor and would be interpolated on initial isotopics and discharge burnup, as is already being done for the UOX fueled PWRs.

Moreover, this method is best applied to systems where spectra do not shift significantly during irradiation. For reactors and fuels that have neutron energy distributions that change more significantly with burnup than a standard UOX fueled LWR, or for cases where the energy spectrum depends strongly on initial isotopics but the model needs to handle a wide variety of initial isotopic permutations, this new method will lose effectiveness. Mixed-oxide and very high burnup Inert Matrix Fuel (IMF), for example, would not be suitable for both of these reasons. Both evince strongly burnup dependent per-atom reaction rates for some species, *e.g.* ^{240}Pu, because of evolving energy and spatial self-shielding effects. Combined with the many degrees of freedom in the initial compositions of these fuels (*i.e.* plutonium and minor actinide

isotopics in the fresh fuels) that may be of interest in fuel cycle studies, an impractically large number of pre-computed cross section libraries would need to be prepared for use with the method presented here. Hence, §5 will extend this algorithm to a multi-group format so as to be able to treat these spectral effects at a higher level of fidelity using a reasonable number of pre-computed libraries.

Chapter 3

Fuel Cycle Sensitivity to Separation Efficiency

3.1 Introduction

As of 2008, the United States power reactor fleet had generated over 50,000 tonnes initial heavy metal (tIHM) of used fuel (UF). The quandary posed by this growing stockpile of UF, combined with the prospect of much larger inventories in the future, poses a considerable obstacle to the development of nuclear energy. While the technical difficulty of storing and disposing of the UF is considerable, it is public trepidation that may have the strongest effect upon the future of the industry.

Partitioning and transmutation will significantly reduce the nuclear waste disposal burden by recycling actinides from UF in advanced reactors and separating the most hazardous fission products for storage in dedicated facilities or target irradiation. Reprocessing technology is one of the key components shared by all advanced fuel cycle concepts. Notably, the efficiency of the reprocessing facilities will have a great impact on the performance of any advanced fuel cycle.

This chapter investigates a fuel cycle parameterization which is only possible because of the essential physics reactor and NFC models presented

71

in §2. how the properties of the reprocessing facility, In particular, the system characteristics of the fuel cycle to its separation efficiency for each of the partitioned elements are studied. The element-specific separation efficiency is defined as the mass ratio of the recovered product to its input mass to the reprocessing facility. The fuel cycle system performance is characterized via three metrics: fuel cycle cost, proliferation resistance and repository impact. To depict repository impact, the repository capacity is modeled as being limited by thermal output; projected dose rate, mass inventory and waste toxicity index are also quantified. The study considers a single-tier nuclear fuel cycle scenario in which light water reactors (LWRs) and 0.5 transuranic (TRU) conversion ratio (CR) sodium-cooled fast reactors (FR) are deployed in an equilibrium that results in zero net TRU production. Actinide management schemes ranging from recycle of plutonium to full TRU recycle are considered.

Using essential physics models at multiple scales, a technical basis for comparing the trade off between repository footprint, system economics, proliferation resistance and the performance characteristics of the reprocessing facilities man be established. This work is significant because target separation efficiencies must be identified at the earliest stages of reprocessing facility design and may be sensitive to other fuel cycle inputs. These models incorporate feedback between the separation efficiencies, reactor performance and fuel cycle mass balances. Therefore, this effort expands upon work that addresses the correlation between heat load and repository capacity [15].

Section 3.2 describes the simulation and metric evaluation methods

used to study the selected fuel cycle scenarios. In §3.3 the simulation approach is benchmarked against published results. §3.4 then applies this model to multiple proposed strategies. Finally, §3.5 presents and discusses the results of the analyses.

3.2 System Modeling Approach

The closed fuel cycle selected for study includes uranium-fueled LWRs as well as FR burners. This fuel cycle was examined in great detail in §2.4.2; a brief overview follows here. After uranium oxide (UOX) fuel is discharged from the LWRs, it undergoes aqueous reprocessing to retrieve transuranics and fission products (FP). A variety of UREX+ inspired partitioning schemes are considered for this step; some or all of the retrieved TRU elements are recycled into the FR TRU burner. In particular, Pu, Pu/Np, and full TRU recycle are studied. FR used fuel is reprocessed and actinide species identified are recycled. Reprocessed burned uranium (BU) and the remaining depleted uranium (DU) are treated as low level waste. Cs and Sr, as two strong heat contributors, are reprocessed from UF at an interim site before they decay to very low level radioactive materials. The other FP will be sent to repository with the residual TRU from reprocessing facility as high level waste (HLW). This scenario is equivalent to a case being considered by the AFC R&D systems analysis group [29].

3.2.1 Overview of Methods

The fuel cycle is specified by reactor material balances and material flows between reactors and fuel cycle facilities. Parameters related to the LWR, for instance burnup and spent fuel isotopic composition, are the reference values adopted in a recent OECD Nuclear Energy Agency (NEA) systems study [25]. The fuel cycle material balance strategy for FR multi-recycle is identical to that used in both the OECD and the AFC R&D studies: to reach the designated burnup level, the first core of the FR is loaded with only DU and retrieved TRU from LWR UF. The second and subsequent cycle are loaded with TRU and U from FR UF plus retrieved top-up TRU from LWR UF and DU. Cycles are continued until the equilibrium state is reached. It is important to dynamically simulate the FR fuel composition at each pass since critical system variables such as partitioning strategy, cooling time and separation efficiency exert a strong effect on the reactor physical characteristics of subsequent recycle passes.

Therefore, a dynamic fast reactor simulation tool is developed to simulate this process and calculate the isotopic composition of the FR fuel at each pass. This model is composed of three components: burnup, reactivity and decay. The reactivity module returns the fresh fuel composition for a specified discharge burnup given the number of batches in the fuel management scheme, while the burnup module calculates the isotopic composition of the burned fuel for a specified fresh fuel composition and discharge burnup target. The decay model applies the Bateman equations to a mass of fuel and returns

74

the isotopic output after a given decay time.

After the fuel isotopic compositions at each pass are determined, the inventory at each stage can be calculated and the system performance of the fuel cycle evaluated. System performance is characterized through fuel cycle cost, proliferation resistance and repository impact. Repository impact is represented by both repository capacity limited by thermal constraints and the projected dose rate from a fully loaded repository.

3.2.2 System Performance Assessment

A number of metrics are applied to the material balances to translate them into decision-relevant information. These metrics include the fuel cycle cost, proliferation resistance, repository capacity via thermal limits, dose release and toxicity.

The fuel cycle cost (FCC) is the cost to buy the fresh fuel to be loaded into the reactors and the cost for recycling and waste disposal. Its components include U ore purchase, U conversion, U enrichment, LWR fuel fabrication, FR fuel fabrication, UF storage, UF reprocessing, LLW (Low Level Waste) disposal, LLW-GTCC (Greater than Class C) disposal, HLW (High Level Waste) disposal.

Procedures for calculating the FCC are summarized briefly here. The FCC_t total charge is the sum of charges for all components of the fuel cycle

cost. It is calculated using the formulation

$$\text{FCC}_t = C_u \cdot s \qquad\qquad (3.1)$$

where C_u [\$/KgHM or \$/SWU] is the unit charge and s [kgHM/yr or SWU/yr] is the service amount. The FCC [\$/MWh] may then be obtained by dividing the FCC_t total charge [\$/yr] by the annual electricity production [MWh/yr].

A fuzzy logic based barrier method is used to evaluate the proliferation resistance of the fuel cycle system [17]. The proliferation resistance is defined as the ability of the system to intrinsically protect itself against proliferators seeking to construct a nuclear explosive device. The method relies upon a group of system-dependent, measurable or quantifiable variables to define proliferation barrier effectiveness of a system as fuzzy numbers. Table 3.1 lists the important variables required for the evaluation. Information at each stage of the fuel cycle system are collected and processed for the proliferation resistance evaluation. Table 3.2 shows the stages involved in the fuel cycle system, type and inventory of materials handled in the stage.

The repository impact is quantified through capacity limitations imposed by thermal constraints as well as the dose release from a fully loaded repository. The Yucca Mountain repository with footprint 1165.8 acres is used for this study [46].

The repository capacity is constrained by the thermal limits placed on the rocks to ensure the successful performance of the engineering barrier system employed in the repository. The thermal restraints considered in this study are

Table 3.1: Required Inputs for PR Evaluation

Item	Name	Unit	Comments
1	StageWeight		Concentration of sensitive materials
2	CriticalMass	kg	Bare sphere Critical Mass (CM)
3	Enrichment	%	Equivalent Enrichment (^{233}U, ^{235}U, ^{239}Pu)
4	SFN	n/s/kg	Spontaneous neutron generation rate
5	HeatRate	W/kg	Heat generation rate
6	Radiation	MeV/s/kg	Gamma Radiation
7	SeparationCost	$/kg	Cost to extract the fissile materials
8	DoseRate	mrem/hr/kg	Dose rate at 1-meter distance
9	Concentration	# of CM/kg	Concentration of fissile material
10	Detectability		Detectability levels (Five levels)
11	FacilityModTime	weeks	Modification time to produce 1 CM per year
12	AccessFrequency	days/yr	Frequency of possible access to facility
13	AvailableMass	# of CM	Available fissile materials
14	MeasureUncert	# of CM/yr	Uncertainty of measurement
15	Knowledge	yr	Time to apply skills to weapons programs
16	Time	yr	Residence time of the materials

Table 3.2: System Material Characteristics

Stage #	Description	Material Form
1	U Ore	U_3O_8
2	U Conversion	UF_6
3	U Enrichment	UF_6 (Enriched)
4	LWR Fuel Fabrication	UOX
5	FR Fuel Fabrication	IMF
6	LWR	UOX
7	FR	IMF
8	Reprocessing	TRU
9	UF Storage	UF (UOX & IMF)
10	LLW Disposal	BU DU
11	LLW GTCC Disposal	CS/SR
12	HLW/TRU Disposal	FP, Residual TRU

200°C on drift walls and 96°C midway between drifts. The repository capacity is estimated using both a simplified repository thermal analysis (SRTA) tool and mass based prediction model. The SRTA is a code based on analytical solution of models of the Yucca Mountain repository [18]. The code calculates the temperature of a given location in the repository and this function is used to determine the repository capacity.

3.3   Benchmarking

The OECD Nuclear Energy Agency has gathered participants from several countries to perform system evaluation of several advanced fuel cycle designs [25]. In this study, the advanced fuel cycles are compared with the reference once-through thermal reactor system.

3.3.1   Benchmark Cases

The system simulation tool developed in this study is applied to the two scenarios defined in the NEA study for benchmark. The scenarios are notated "scheme 1a" and "scheme 3a". Scheme 1a is a once-through LWR system. Enriched uranium (4.9% ^{235}U) is burned in an LWR to 60 MWd/kgIHM. The UF is sent to a storage facility for 7 years of decay. Another 50 years cooling is assumed before the UF is disposed in the repository. The key fuel cycle parameters describing this case are presented in Table 3.3.

Scheme 3a is a closed fuel cycle design using a fast reactor burner to consume recycled TRU from the LWR UF. The precise isotopic composition

Table 3.3: Scheme 1a System and Reactor Design: 0.71% NU is enriched to 4.90% for UOX with tail enrichment 0.25%; Designed capacity of the LWR is 1450 MWe. The load factor is 90%. The burnup is 60 MWd/kgIHM.

Stage #	Description
Mass Flows for Scheme 1a (kgIHM/TWh$_e$)	
NU	20723
DU	18673
UOX	2050
Element in UF after 7 years of Decay	
U	1890
Pu	26
Np	1.9
Am	1.6
Cm	0.28
FP	130

of this fuel was not provided in the study; therefore ORIGEN was used to calculate it. The results, which act as an input to the FR burnup calculations, are given in Table 3.4. For this calculation, as stipulated in the OECD study, the uranium was enriched to 4.2% ^{235}U and burned in the LWR to 50 MWd/kgIHM.

The retrieved Pu and other MA are used for fast reactor fresh fuel. The TRU from the FRs is decayed for 3 years before the used fuel is fully reprocessed and recycled. The fission products and actinides lost in reprocessing are sent to repository as high level waste after 50 years cooling. The load factor is 90% for LWRs and 85% for FRs. In this benchmark scenario, the separation efficiency for all species is 99.9%. The top-level system parameters for Scheme 3a are presented in Table 3.5.

Table 3.4: Nuclide Composition [kg$_i$/kgIHM] of LWR TRU feed to FR after 6 years of Cooling

Nuclide	LWR Fresh	LWR UF
^{241}Am		4.74E-04
^{243}Am		2.13E-04
^{242}Cm		3.80E-09
^{243}Cm		6.97E-07
^{244}Cm		7.21E-05
^{245}Cm		4.38E-06
^{246}Cm		6.91E-07
^{247}Cm		9.03E-09
^{248}Cm		6.36E-10
^{237}Np		7.62E-04
^{238}Pu		2.95E-04
^{239}Pu		5.89E-03
^{240}Pu		2.73E-03
^{241}Pu		1.31E-03
^{242}Pu		8.59E-04
^{234}U		1.64E-05
^{235}U	4.20E-02	6.83E-03
^{236}U		5.65E-03
^{238}U	9.58E-01	9.23E-01

Table 3.5: Scheme 3a System and Reactor Design: 0.71% NU is enriched to 4.20% for UOX with tail enrichment 0.25%; capacity of the LWR is 1450 MWe. The load factor is 90%. The burnup is 50 MWd/kgIHM for LWR and the UF is decayed for 6 years before it is reprocessed. The retrieved TRU is mixed with DU for FR fresh fuel. The FR burnup is 140 MWd/kgIHM and the FR UF is reprocessed after 3 years of decay. The capacity of the FR is 600 MWe and the load factor is 85%. 36.8% of fleet electricity comes from FR.

Stage #	Description
Mass Flows for Scheme 3a (kgIHM/TWh$_e$)	
NU	12991
UOX	1513
FR FF	289
Element in HLW after Separation	
U	1.588
Pu	0.084
Np	0.0027
Am	0.006
Cm	0.0026
FP	117.5

The unit costs used are summarized in Table 3.6. The disposal costs for HLW and UF are calculated from the information available in an earlier OECD NEA report [24]. This report recommends 210,000 \$/m^3 and 400,000 \$/m^3 for the disposal charges of UF and HLW respectively. After conditioning, 1 tIHM UF will result in 2 m^3 waste, or 420 \$/kgIHM. For vitrified HLW, a canister of volume 0.18 m^3 is taken to contain 47.6 kg fission products and 3.55 kg actinides. Therefore the disposal charge for HLW becomes 1408 \$/kgIHM.

Table 3.6: Unit Costs used in Benchmark Study

Item	Unit	Value
U Ore (yellow cake)	\$/kgHM	50.0
U Conversion	\$/kgHM	5.0
U Enrichment	\$/SWU	100.0
LWR Fuel Fabrication	\$/kgHM	250.0
FR Fuel Fabrication	\$/kgHM	2600.0
Reprocessing for LWR Used Fuel	\$/kgHM	800.0
Reprocessing for FR Used Fuel	\$/kgHM	2500.0
UF Storage	\$/kgHM	90.0
LLW Near Surface Disposal	\$/kgHM	3.60
LLW GTCC Disposal	\$/kgHM	381.0
UF Disposal	\$/kgHM	420.0
HLW Disposal	\$/kgHM	1408.0

3.3.2   Benchmark Results

The composition of FR fuel at equilibrium is calculated with the dynamic FR simulation tool described in §2 and compared to results published in the OECD study. The fuel cycle cost is also benchmarked using the unit costs shown in Table 3.6 The inventory and FCC comparisons are shown in Table

3.7 for both schemes. As mentioned above, ORIGEN was used to compute the LWR material balance.

The inventories of major actinides in the HLW in scheme 1a from both studies are in close agreement with relative errors of less than 10%, except Cm which has a smaller absolute inventory in the system. The mean value of FCC from OECD study is approximately 4.7 $/MWh for scheme 1a from the sensitivity result in the OECD report. The value of 4.27 $/MWh here is within 10% error. This variation stems from minor differences in the cost assessment methodology and back-end unit costs.

Scheme 1a does not benchmark the dynamic FR simulation tool; however it does provide the TRU isotopics that serve as the starting point for the calculations carried out by the tool. The procedure described in §2 was used to perform cycle iterations until the FR fuel composition converged to equilibrium. Good agreement on the LWR to FR power split, charge and discharge inventories and the FCC for scheme 3a can be observed. Whether the difference observed for scheme 3a can be ascribed to the FR simulation tool, or to inconsistencies in the LWR feed arising from the absence of isotopic data in the OECD study, cannot be established. However in view of the complexity of the fuel cycle system the agreement is strong. For instance, the design parameters of the FR were not given in sufficient detail to perform transport-burnup calculations, so a case-specific cross section library could not be prepared and available data for a FR that shares many properties of the OECD study reactor (*e.g.* sodium-cooled, metallic fuel, similar pitch and fuel pin radius) were

used instead.

Table 3.7: Scheme 1a Benchmark Results

Parameter	OECD 2006	Results	% Difference
UOX FF [kg/TWh$_e$]	2050	2050	0.0
NU [kg/TWh$_e$]	20723	20722.8	0.0
U in HLW [kg/TWh$_e$]	1890	1896	0.3
Pu in HLW [kg/TWh$_e$]	26	24	-8.86
Np in HLW [kg/TWh$_e$]	1.9	2.0	4.29
Am in HLW [kg/TWh$_e$]	1.6	1.7	8.55
Cm in HLW [kg/TWh$_e$]	0.28	0.24	-15.17
FP in HLW [kg/TWh$_e$]	130	127	-2.61
FCC [\$/MWh]	4.7	4.27	-9.15

The OECD group has also conducted repository performance studies for their schemes 1a and 3c, where 3c is a FR only closed fuel cycle. Because the HLW from both scheme 3c and 3a is mainly composed of FP, the repository performance assessments for schemes 3a and 3c can be expected to yield nearly equivalent results.

The energy that has been produced by disposed waste in a fully loaded salt-based repository is given as 6615 TWh for scheme 1a and 26930 TWh for scheme 3c. In other words, the waste from closed fuel cycle 3c would have generated 4.0 times as much electricity as scheme 1a waste placed in the same repository. Using the repository capacity assessment methodology described in §3.2.2, the energy that has been produced by disposed waste in a tuff-based repository in this study is 28286 TWh for scheme 1a and 186365.3 TWh for scheme 3a. Therefore, the current work predicts that scheme 3a can,

Table 3.8: Scheme 3a Benchmark Results

Parameter	OECD 2006	Results	% Difference
Electricity Share: LWR [%]	63.2	66.1	4.59
Electricity Share: FR [%]	36.8	33.9	-7.88
UOX FF [kg/TWh$_e$]	1513	1583	4.63
NU [kg/TWh$_e$]	12991	13593.2	4.64
UOX FF [kg/TWh$_e$]	289	266.2	-7.88
U in HLW [kg/TWh$_e$]	1.588	1.6361	3.03
Pu in HLW [kg/TWh$_e$]	0.084	0.0814	-3.10
Np in HLW [kg/TWh$_e$]	0.0027	0.0030	10.52
Am in HLW [kg/TWh$_e$]	0.006	0.0073	21.62
Cm in HLW [kg/TWh$_e$]	0.0026	0.0020	-21.8
FP in HLW [kg/TWh$_e$]	117.5	119.3	1.59
FCC [$/MWh]	5.5	5.13	-6.73

when compared to scheme 1a, generate 6.6 times as much electricity given a repository of specified thermal capacity. This is higher than the 4.0 ratio calculated in the OECD study, but the difference in the geologic medium – salt versus tuff – complicates the comparison.

3.4   Case Study and Results

For the study of system sensitivity to separation efficiency and partitioning strategy, we consider a fleet in which LWRs and CR 0.5 FRs are in equilibrium. This is the same concept as was put into practice in scheme 3a of the OECD study.

3.4.1 Definition of the Cases

The present-day industrial scale reprocessing technology, PUREX, retrieves U and Pu from UF. Fuel cycle strategies developed under the AFC R&D called for extraction of Np with Pu to ease proliferation concerns, material accountability and tracking procedures for the product stream. It has been convincingly established [46] that separation of Am and Cm as well is necessary to maximize the benefit of increasing the capacity of a repository that is constrained by thermal limits. The repository capacity can be further expanded by removing Cs and Sr for interim storage. Therefore, in this study, four partitioning strategies are compared:

- Stra1: Separation of U and Pu to be reused in FR

- Stra2: Separation of U, Np and Pu to be reused in FR

- Stra3: Separation of U, Np, Pu, Am and Cm to be reused in FR

- Stra4: Separation of U, Np, Pu, Am and Cm to be reused in FR, and separation of Cs and Sr for interim storage

In a scenario involving multi-recycle of spent fuel, the cumulative effect of reprocessing losses at each recycle can become quite significant, so that only with high separation efficiencies can the full benefit of the multi-recycle strategy be realized. For example, the NEA study indicated that for their cases 3a and 3c that less than 0.01% loss is needed to reach a factor of 100

86

reduction in the high level waste heat burden to the repository. Therefore, to develop an understanding of the sensitivity of the system performance metrics to separation efficiency, four levels are studied:

- Level1: 90%

- Level2: 99%

- Level3: 99.9%

- Level4: 99.99%

The separation efficiencies of all elements are assumed to be the same. There is no *a priori* reason to make this assumption as no aspect of reprocessing facility design or operation imposes such a constraint. Instead, this assumption was made to simplify the analysis and prevent an egregious proliferation of cases to be studied. In addition, and for similar reasons of clarity, the aqueous LWR fuel reprocessing and the electrochemical FR metallic fuel separations share the same efficiencies. Four partitioning strategies and four separation efficiency levels generate the 16 cases defined in Table 3.9. Table 3.10 shows the elemental separation efficiencies for the cases; an entry of zero indicates that the element remains with the repository-bound waste stream.

3.4.2 Results and Discussion

The 16 cases defined in previous chapter have each been modeled through the transient phase to equilibrium with the FR material balance tool described

Table 3.9: 16 Case Definitions

	Stra1	Stra2	Stra3	Stra4
Level1	Case01	Case02	Case03	Case04
Level2	Case1	Case2	Case3	Case4
Level3	Case11	Case12	Case13	Case14
Level4	Case21	Case22	Case23	Case24

Table 3.10: Separation Efficiencies by Case and Element

Case	U	Np	Pu	Am	Cm	Cs	Sr
case01	0.9	0	0.9	0	0	0	0
case02	0.9	0.9	0.9	0	0	0	0
case03	0.9	0.9	0.9	0.9	0.9	0	0
case04	0.9	0.9	0.9	0.9	0.9	0.9	0.9
case1	0.99	0	0.99	0	0	0	0
case2	0.99	0.99	0.99	0	0	0	0
case3	0.99	0.99	0.99	0.99	0.99	0	0
case4	0.99	0.99	0.99	0.99	0.99	0.99	0.99
case11	0.999	0	0.999	0	0	0	0
case12	0.999	0.999	0.999	0	0	0	0
case13	0.999	0.999	0.999	0.999	0.999	0	0
case14	0.999	0.999	0.999	0.999	0.999	0.999	0.999
case21	0.9999	0	0.9999	0	0	0	0
case22	0.9999	0.9999	0.9999	0	0	0	0
case23	0.9999	0.9999	0.9999	0.9999	0.9999	0	0
case24	0.9999	0.9999	0.9999	0.9999	0.9999	0.9999	0.9999

in §2. In addition, the performance metrics defined in §3.2.2 have been calculated. Table 3.11 lists the fraction of equilibrium reactor fleet electrical power generated by the FRs. Note that for neutronic purposes Stra3 is the same as Stra4 in which Cs and Sr are partitioned. For each strategy, higher separation efficiency leads to higher FR share because more TRU are reused from LWR UF and FR UF.

Table 3.11: FR Share of Fleet Electricity Generation [%]

	Stra1	Stra2	Stra3	Stra4
Level1	26.0	26.0	25.6	25.6
Level2	33.0	33.0	33.0	33.0
Level3	33.8	33.8	33.9	33.9
Level4	33.9	33.9	34.0	34.0

The system performance of the fuel cycle for the 16 cases will be discussed separately for material balance and isotopics, FCC, proliferation resistance and repository performance.

3.4.2.1 Material Balance and Isotopics

Table 3.12 displays the parameters input to the FR material balance tool. Note that the partitioning strategies and separation efficiencies are also vital inputs to the model. FR operations are simulated until equilibrium is attained.

Figure 3.1 shows the mass fraction [kg/kgIHM] of each of the four input streams (DU, LWR-TRU, FR-U, and FR-TRU) to FR fuel fabrication as a function of FR recycle number. Self recycle of FR UF begins on pass 2.

Table 3.12: Input Parameters to FR Material Balance Model

Parameter	Value
FR Discharge Burnup (BUd)	140 MWd/kg
Number of FR Fuel Batches	3
FR Non-Leakage Probability (P_{NL})	0.65
Cross Section Library	§2
Isotopes to Converge for Equilibrium	^{239}Pu, ^{240}Pu, ^{242}Pu
Post-discharge Cooling Time	3 years

It can be seen that the top-up is drawn predominantly from the recycled LWR-TRU. However, the mass fraction of each of the four streams converges quickly toward an apparent equilibrium after only a few cycles. The criterion described in Table 3.12 leads to equilibrium being reached at cycle 10. Therefore Figure 3.1 is very similar to the corresponding Figure 2.18 in §2.

The fast reactor output stream is a function of cycle number. Individual isotopes contained in the FR fuel do not necessarily converge after only a handful of cycles. Figure 3.2 shows the mass fractions at discharge of ^{237}Np, ^{239}Pu, ^{241}Am and ^{244}Cm. It can be seen that the higher A number actinides have not yet converged even after 10 cycles. Also noteworthy is the dependence of the isotopic composition of the FR fuel upon separation efficiency. The higher A number species are especially strongly affected by the efficiency. The ^{244}Cm inventory, for example, differs by 20% at equilibrium for the 90% efficiency case versus the 99.99% case. Figure 3.3 plots the fraction of uranium and transuranics relative to the total actinide content of the output stream.

Figure 3.1: Input Streams to FR Fuel Fabrication [kg/kgIHM]
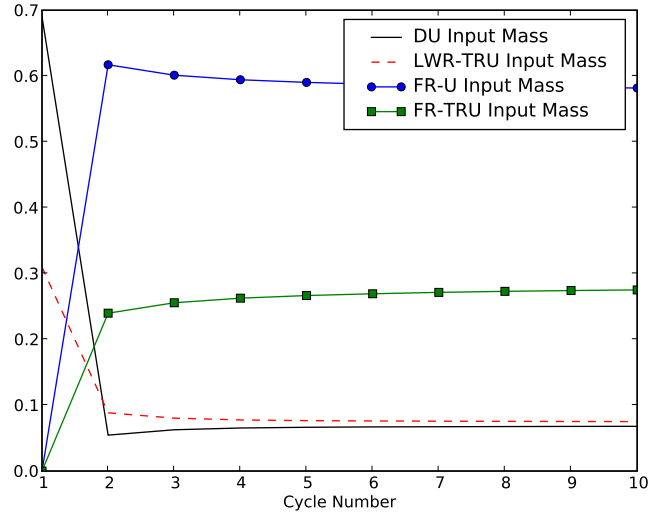
The transuranic conversion ratio (TRU CR) is defined in equation 2.21. Here, TRU_{in} is set as the sum of the LWR-TRU and FR-TRU stream mass fractions as plotted in Figure 3.1. TRU_{out} is the TRU mass fraction in the FR UF stream, as seen in Figure 3.3. Figure 3.4 shows that the TRU CR equilibrates at around 0.495. Note that the CR is not an input to the model, but rather a derived quantity that is a consequence of the reactor configuration and discharge burnup. The FR power fraction is likewise a derived quantity.

3.4.2.2 Fuel Cycle Cost

Table 3.13 shows the FCC computed using the unit costs described above. For all strategies, higher separation efficiencies (SE) lead to lower

Figure 3.2: Input and Output Mass [kg/kgIHM] for Selected Actinides at Two
Separation Efficiencies
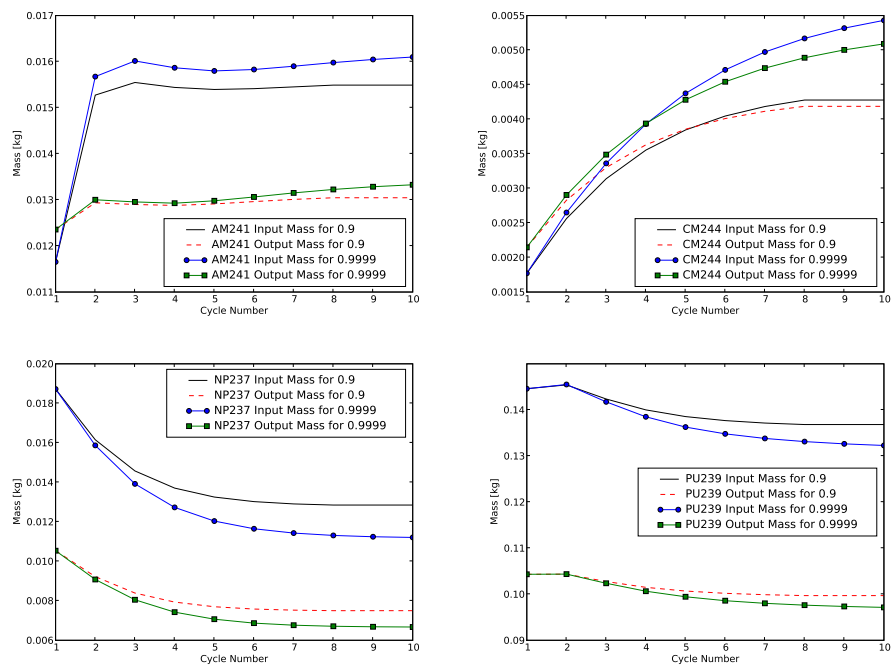
Figure 3.3: FR-U and FR-TRU Output Mass Fractions [kg/kg discharged heavy metal]
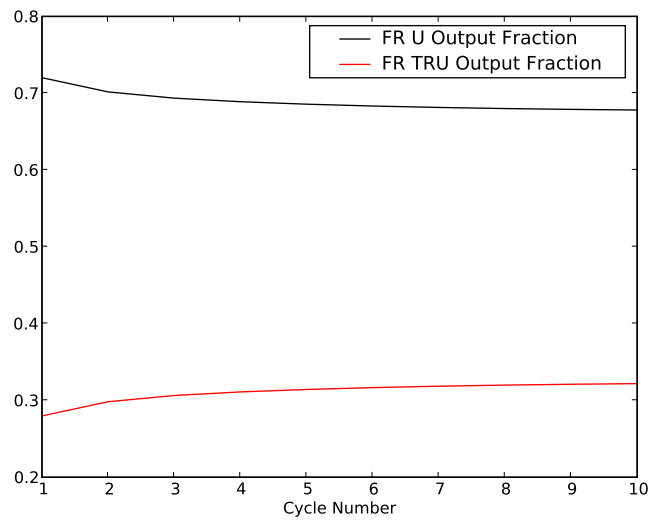
Figure 3.4: TRU Conversion Ratio
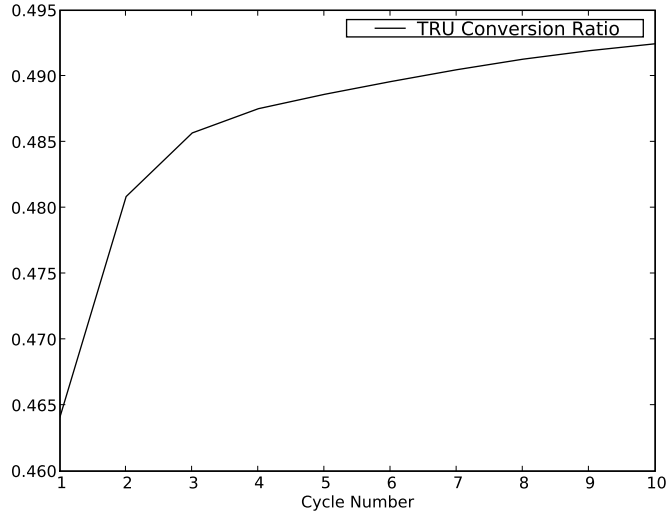
FCC while there is no advantage for 99.99% SE compared to 99.9% SE. Note that the reprocessing cost is of necessity assumed to be independent of the separation efficiency. It is recognized that higher efficiencies will require more separation stages and operation time, almost inevitably leading to more costly plant operations. However a review of literature shows that the difficult task of correlating process costs to separation efficiency has not yet been undertaken.

Table 3.13: FCC with Fixed Disposal Charge [$/MWh]

	Stra1	Stra2	Stra3	Stra4
Level1	5.51	5.51	5.50	5.50
Level2	5.18	5.18	5.16	5.16
Level3	5.15	5.14	5.13	5.12
Level4	5.14	5.14	5.13	5.12

94

The FCC components are listed in detail in Tables 3.14-3.17. At Level1, lower separation efficiency results in more mass is reprocessed in the reprocessing facility; hence the difference from the reprocessing charge component dominates the small difference in FCC as one progresses to more complex actinide partitioning strategies (Stra1 to Stra4). When the separation efficiency increases from 90% to 99% or 99.9% the annual charge for reprocessing service drops by around 10%, commensurate with the process mass reduction. It is expected that the unaccounted for cost premium associated with achieving the higher efficiencies would counteract this effect.

Table 3.14: Cost Components for Cases 01-04

Components [$/MWh]	case01	case02	case03	case04
U Ore (yellow cake)	0.76	0.76	0.76	0.76
U Conversion	0.08	0.08	0.08	0.08
U Enrichment	1.11	1.11	1.11	1.11
LWR Fuel Fabrication	0.44	0.44	0.44	0.44
FR Fuel Fabrication	0.53	0.53	0.53	0.53
Reprocessing	1.93	1.93	1.93	1.93
UF Storage	0.17	0.17	0.17	0.17
LLW Disposal	0.05	0.05	0.05	0.05
LLW GTCC Disposal	0.00	0.00	0.00	< 0.01
HLW/TRU Disposal	0.44	0.44	0.43	0.42

3.4.2.3   Proliferation Resistance

The intrinsic proliferation resistance varies weakly between the cases due to the separation efficiency and more strongly as a consequence of partitioning strategy. Table 3.18 lists the system proliferation resistance value for

Table 3.15: Cost Components for Cases 1-4

Components [$/MWh]	case1	case2	case3	case4
U Ore (yellow cake)	0.69	0.69	0.69	0.69
U Conversion	0.07	0.07	0.07	0.07
U Enrichment	1.00	1.00	1.00	1.00
LWR Fuel Fabrication	0.40	0.40	0.40	0.40
FR Fuel Fabrication	0.67	0.67	0.67	0.67
Reprocessing	1.93	1.93	1.93	1.93
UF Storage	0.16	0.16	0.16	0.16
LLW Disposal	0.05	0.05	0.05	0.05
LLW GTCC Disposal	0.00	0.00	0.00	< 0.01
HLW/TRU Disposal	0.21	0.21	0.19	0.18

Table 3.16: Cost Components for Cases 11-14

Components [$/MWh]	case11	case12	case13	case14
U Ore (yellow cake)	0.68	0.68	0.68	0.68
U Conversion	0.07	0.07	0.07	0.07
U Enrichment	0.99	0.99	0.99	0.99
LWR Fuel Fabrication	0.40	0.40	0.40	0.40
FR Fuel Fabrication	0.69	0.69	0.69	0.69
Reprocessing	1.93	1.93	1.93	1.93
UF Storage	0.16	0.16	0.16	0.16
LLW Disposal	0.05	0.05	0.05	0.05
LLW GTCC Disposal	0.00	0.00	0.00	< 0.01
HLW/TRU Disposal	0.19	0.18	0.17	0.16

Table 3.17: Cost Components for Cases 21-24

Components [$/MWh]	case21	case22	case23	case24
U Ore (yellow cake)	0.68	0.68	0.68	0.68
U Conversion	0.07	0.07	0.07	0.07
U Enrichment	0.99	0.99	0.99	0.99
LWR Fuel Fabrication	0.40	0.40	0.40	0.40
FR Fuel Fabrication	0.69	0.69	0.69	0.69
Reprocessing	1.93	1.93	1.93	1.93
UF Storage	0.16	0.16	0.16	0.16
LLW Disposal	0.05	0.05	0.05	0.05
LLW GTCC Disposal	0.00	0.00	0.00	< 0.01
HLW/TRU Disposal	0.19	0.18	0.17	0.16

all cases. Recall that higher numbers imply a greater intrinsic proliferation resistance for the system. As an example, when applied to the OECD benchmark case scheme 1a this model generates a proliferation resistance value of 0.2416.

The differences between cases arise from the reprocessing and HLW disposal stages. UF storage and HLW disposal handle similar materials and both represent pure storage sites. Hence they share same level of proliferation resistance. The large difference in inventory at HLW disposal site as the partitioning strategy is varied generates relatively large proliferation resistance differences at this stage. FR fuel fabrication, LWR reactor, FR reactor and reprocessing facility have lower proliferation resistance value in the fuel cycle system due to the large inventory of actinides Pu, Np, Am and Cm. Especially in the reprocessing stage, the pure Pu in case01, case1 and case11 negatively impact the proliferation resistance value. The benefit of co-extraction of Np,

97

Am and Cm with Pu is shown to lead to the best proliferation resistance value.

Table 3.18: System Proliferation Resistance Value

	Stra1	Stra2	Stra3	Stra4
Level1	0.1850	0.1874	0.2421	0.2422
Level2	0.1853	0.1870	0.2418	0.2418
Level3	0.1852	0.1865	0.2414	0.2414
Level4	0.1852	0.1865	0.2413	0.2410

3.4.2.4   Repository Performance

The heat load based repository capacity is shown in Table 3.19. The benefit accrued by separating Am, Cm, Cs and Sr from the spent fuel is considerable. At all three levels, by separating Am and Cm only, the repository capacity doubles and further separation of Cs and Sr make the repository capacity 3.7 times (level 1), 25.8 times (level 2), 228.5 times (level 3) and 1221.2 times (level 4) greater compared to strategy 1.

Table 3.19: Repository Capacity [tIHM/Repository]

	Stra1	Stra2	Stra3	Stra4
Level1	9342	9383	28766	34609
Level2	4849	4755	23341	124877
Level3	4388	4291	22555	1002783
Level4	4342	4244	22478	5302541

The benefit of higher separation efficiency can be clearly appreciated from the result in Table 3.20 where the repository capacity is represented as the total electricity generated from the HLW that may be placed in a fully

loaded repository. Higher separation efficiency leads to greater economy of repository usage in all cases, but it is especially noteworthy that only for Stra4, where Cs/Sr partitioning is pursued, does it become worthwhile to achieve 99.99% efficiency for all species. This result is simply a consequence of the capacity-limiting species for each strategy. In strategies 1 through 3, once 99.9% efficiency is reached, Cs and Sr become limiting, so that there is no further benefit to reaching 99.99% actinide separation efficiency unless Cs and Sr are partitioned as well.

Table 3.20: Repository Capacity [GWh/Repository]

	Stra1	Stra2	Stra3	Stra4
Level1	2.96E+07	3.00E+07	9.39E+07	1.15E+08
Level2	3.26E+07	3.26E+07	1.71E+08	9.63E+08
Level3	3.30E+07	3.30E+07	1.86E+08	8.81E+09
Level4	3.30E+07	3.30E+07	1.88E+08	4.72E+10

Note that the dramatic increase in the heat-based capacity of the repository is not matched by commensurate decreases in HLW volume or dose. Table 3.21 shows the mass of HLW generated by each unit of electricity produced. Therefore, the capacity enhancement shown in Table 3.19 may not be accompanied by a proportionate decrease in disposal cost. Likewise, the potential dose of materials placed in a fully loaded repository is many times higher for Stra4 than for the other cases.

Table 3.21: HLW Mass Per Unit Energy Produced [gHM/GWh]

	Stra1	Stra2	Stra3	Stra4
Level1	315.5	312.9	306.4	300.0
Level2	148.8	145.8	136.9	129.7
Level3	133.2	130.2	121.0	113.8
Level4	131.6	128.7	119.5	112.2

3.5   Conclusions

A modeling framework which couples essential physics models for fuel cycle and reactor material balance generation, repository capacity, dose and toxicity assessment, economics, and proliferation resistance has been developed and benchmarked. The model suite was created to investigate the sensitivity of these important fuel cycle outcomes to changes in partitioning strategies and elemental separation efficiency in reprocessing plants.

The modeling framework is unique because it links reactor burnup and reactivity calculations with a repository thermal analysis tool and multi-zonal transport model to treat repository performance and an economic module. The linkage is significant because perturbations to system input variables such as separation efficiencies are propagated through all the submodels. For instance, the material balance tool recalculates the transient and equilibrium FR cycle material balances.

This new framework was applied to an AFC R&D-inspired LWR and transmuter FR fuel cycle architecture. Partitioning strategies were varied with Np, Am/Cm, and Cs/Sr alternatively being partitioned for recycle or storage

or sent to the repository with the low heat emitting fission products. Elemental separation efficiencies were also varied with values of 90% to 99.99% being considered. It was shown that the efficiency of repository space usage, measured by the energy produced by the fuel from which the HLW placed in the repository was derived, can be improved by more than two orders of magnitude if 99.99% separation efficiency is achieved and Cs/Sr are partitioned. If Cs/Sr are not partitioned, it was not seen to be worthwhile to exceed 99.9% efficiency. On the other hand, drastic increases in the loading of the low heat releasing fission products to the repository may limit the potential benefit of the transmutation scheme by increasing the dose, toxicity, and mass to be interred.

In the short term, it is of interest to consider the separation efficiency for individual elements. Perhaps capacity enhancement goals can still be met even if 99.9% or 99.99% efficiency is not met at each step. For example, if Cs/Sr efficiency is limited to 99.9%, it appears that achieving an equivalent TRU separation efficiency may not be necessary. 99% could suffice with the same repository benefit.

As the understanding of the variation of disposal cost with these parameters and the response of the reprocessing cost to efficiency improves, system design sensitivities will emerge as an important area of study. This self-contained, physics-based tool executes and incorporates needed feedbacks between components. As such, a stochastic system wrapper that invokes this new fuel cycle tool could efficiently search the parameter space. This wrap-

per would be capable of generating a large number of histories such that an information-theoretic approach would also be needed to extract the relevant analyses from the data set.

Chapter 4

Information Theoretic Fuel Cycle Analysis

4.1 Introduction

Technology development and deployment (TD&D) decisions will play a key role in establishing the array of diverse, interconnected technologies that might comprise future nuclear fuel cycles (NFCs). These decisions are made in view of one or more objectives for the NFC the technology will support. As §3 discusses, objectives include minimizing electricity production costs, increasing the efficiency of resource or geologic repository utilization, and mitigating the risk of safety incidents or misuse of technologies or materials.

TD&D decisions are justified by weighing their costs against the expected benefits, monetary, monetizable or otherwise, that follow when they come to fruition. To that end, multiple NFC simulation models [11, 26] have been devised, including one in §2. One aim of these models is enable these hypothetical outcomes to be quantified. Two major challenges associated with this goal are the uncertainties in the deployment and performance of other NFC technologies and the nuclear energy industry as a whole, and the complex interdependence between the technology being considered, other NFC technologies and their own (uncertain) characteristics, and NFC outcomes.

One method of addressing these challenges is by applying entropy-based statistical methods of information theory to describe outcomes produced by an NFC model. Past efforts at sensitivity and uncertainty analysis on such a system have largely been limited to deterministic approaches. For instance, brute-force techniques of linear sensitivity analysis have been used to give rise to sensitivity coefficients, *i.e.* the change in an outcome divided by the change in an input. In principle, these coefficients are valuable inputs to the TD&D decision-making process since they can inform the return on an investment. For example, the incremental gain in heat-limited repository capacity per unit change in the efficiency of separating, say, americium from used fuel.

However, coefficients generated in this way have a limited range of validity since they are departures from a 'base case' where each input is varied singly, holding others fixed. Returning to the above example, the gain in repository capacity might be found to be quite small if the separation efficiency of plutonium is low (since Pu dominates the heat load borne by the repository). On the other hand the repository capacity gains would be large if the Pu separation efficiency is high (and Am dominates the heat load). Many other parameter combinations of this type can be imagined, each contingent on and affecting the characteristics of one of the fuel cycle technologies. Comprehensive, brute-force evaluation of a parameter space of this size may not be feasible.

Since the system being simulated is complex, it is appropriate to treat it as a 'black box' and use statistical measures to characterize its behavior. This

paper subjects an NFC simulator to a contingency table analysis, that in turn unlocks functional-form independent, entropy-based measures of input-output dependence. The contingency tables are generated by stochastically invoking the NFC simulator. Each scenario realization consists of thirty technology-defining inputs sampled from distributions encompassing physically meaningful values. Computed from the contingency tables, the entropy statistic establishes the strength of correlation between any input and any output without defining a 'base case' or set of reference technology properties.

To capture joint sensitivities, like the simultaneous and complex interdependence of the above mentioned Pu and Am separation efficiencies on repository capacity, a novel statistical measure is defined. This measure, a coefficient of variation, uses three-dimensional contingency table data to describe the change in the variance of an outcome with respect to one input, over the range of admissible values of a second input. A high value for this statistic indicates that the impact of one input on the outcome is strongly dependent on the value of the second input. This measure supports fuel cycle analysis and TD&D decision-making by identifying inputs (and their parent technologies) that can, if also altered, augment or reduce the effect of the decision being considered.

The remainder of this paper is organized as follows. §4.2 provides a brief overview of the field of information theory and its underlying metrics, which are relied on heavily in this paper. §4.3 presents an algorithmic summary of the methodology employed to carry out the fuel cycle study. §4.4

describes the fuel cycle simulations and method for sampling the input parameters to be varied, while §4.5 presents the theoretical background underpinning the entropy-based statistical measures. §4.6 provides results for the statistical measures applied to the scenario space outlined in §4.4 and offers several case studies that illustrate the interpretation of the statistical outcomes. §4.7 concludes with options for future work.

4.2   Information Theory Overview

The field of Information Theory is often said to have formed with C. E. Shannon's seminal 1948 publication entitled "A Mathematical Theory of Communication" [38]. In this treatise he detailed a parameter known as *entropy* and applied it to the challenge of conveying messages using the minimal amount of information. He applied this entropy-based framework to discrete and continuous, noisy and noiseless communication systems.

Shannon's entropy is a probabilistic quantity named in analogy to the thermodynamic property. The statistical dynamic entity was first formulated via the H-Theorem set down by L. Boltzmann [4]. This theorem shows that the entropy of a collection of particles may only increase with time until the state of maximum entropy. This state is described by the kinetic energy of the particles having Gaussian distribution.

Both the physical and Shannon entropy are measures of a complex system given a set of micro-states or probabilities. They therefore can be used as a way to correlate the system as a whole to its underlying independent

106

variables [45]. As Science, Engineering, and Technology have progressed to problems of greater complexity such statistical measures have found many applications.

In Biology, particularly in the sub-field of bioinformatics, information theory plays a central role [31, 49]. The advent of computers has enabled new analysis tools in Linguistics, which often use entropy-based measures [20]. Moreover, information theory continues to have broad reaching applications within Cryptography [2].

One method of constructing discrete probability distributions are known as contingency tables. These were first formulated by K. Pearson in a biological context [27]. Contingency tables are intended to be used to determine correlations between the variables on their axes. Coupled with entropy-based measures, contingency tables provide a scalable substitute for linear 1D sensitivity studies of complex systems. Here they will be applied to the nuclear fuel cycle.

4.3 Methodology

Statistical performance measures are applicable to a nuclear fuel cycle simulation model that is amenable to stochastic execution under variation of several independent parameters. Values for each input are to be chosen stochastically from a predefined, physically-valid range. By generating many inputs and tabulating the corresponding results from an underlying physics-based fuel cycle model, the fuel cycle undergoes a Monte Carlo simulation.

An input-output vector constitutes a single fuel cycle realization. From here, relevant statistical metrics on the set of realizations yield information on how the system as a whole performs. Two independent parameters (x and y) and one response (R) variable are examined. This methodology may be seen graphically in Figure 4.1.

To further system analysis objectives, 'standard' statistical metrics (such as the mean response over all runs) may be calculated. However, the usual correlation coefficients imply a linear relationship between input and response. Given the complexity of the system, linearity is not a safe assumption for many system metrics. Thus, novel information theoretic measures have proved more valuable to ranking the importance of input parameters [19].

Additionally, it is useful to extend the information theoretic metrics from their typical 2D formulations to the three dimensional equivalents. If 3D metrics are constructed such that they relate two input parameters to a response, then joint sensitivity or co-variance information can be computed from a single set of stochastically-generated data. Conditional covariances (sensitivity of sensitivity) can thus be measured for two inputs to one response. To maintain a realistic physical interpretation of this type of covariance, a combination of entropy-based metrics extended to 3D metrics can be formulated (discussed in §4.5.1.4). Any statistical analysis along these lines, though, must be built around a model of the flow of materials through the nuclear fuel cycle, and the transformations that constituent NFC technologies apply to the material flow.
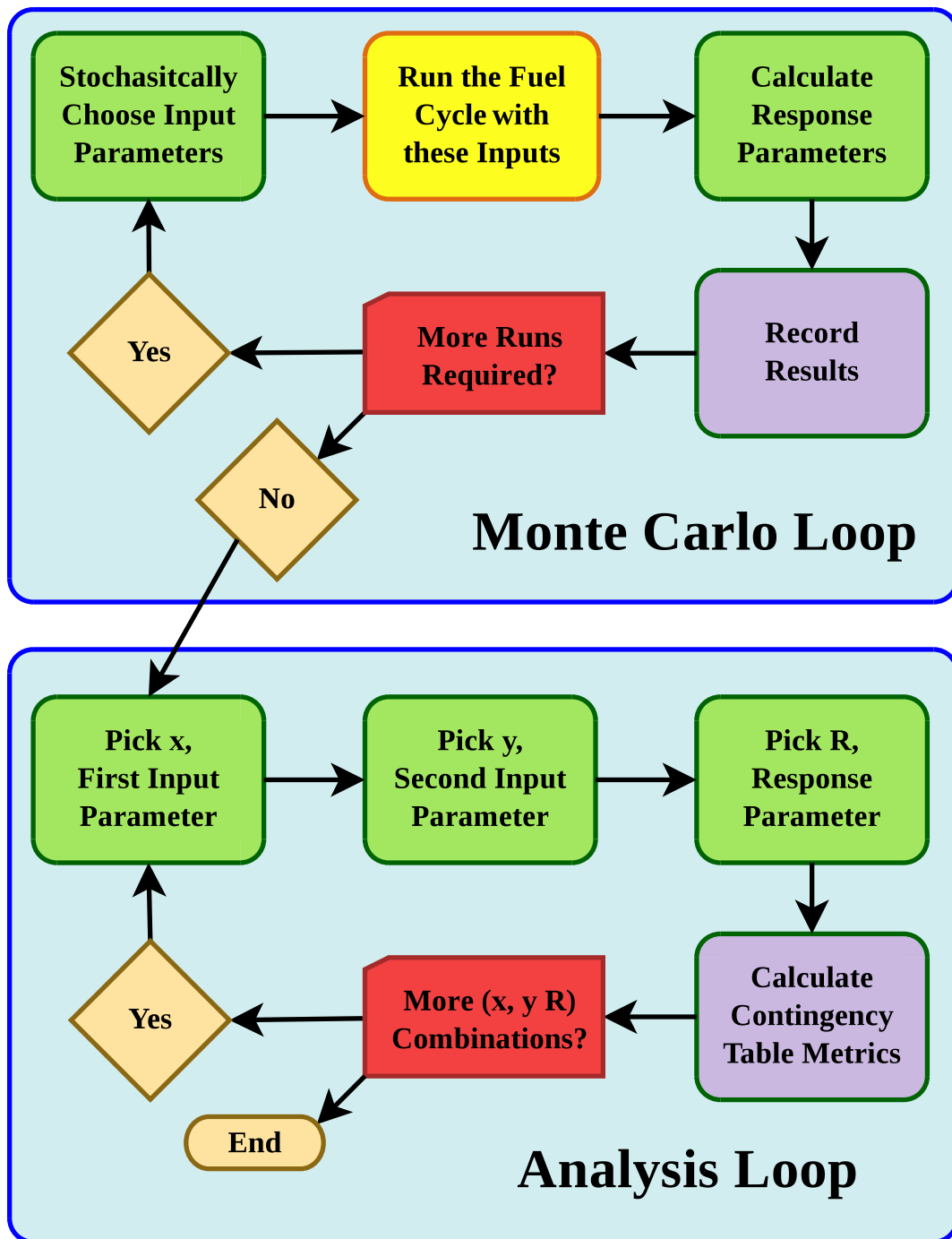
Figure 4.1: Monte Carlo Methodology & Analysis Diagram

4.4 Nuclear Fuel Cycle Simulation

A fuel cycle simulation package that incorporates essential physics sub-models of reactor burnup [35] and repository performance [17] served as the platform for this analysis. The approach taken in each submodel is briefly summarized below. Full fuel cycle execution time, including all transients in a closed cycle scenario, takes between 10-30 seconds on a modern computer processor.

The importance of essential physics models (as opposed to curve fits or other parameterizations that are valid only under specific conditions) in a sensitivity study of this type must be stressed. Given the number of degrees of freedom associated with a fuel cycle scenario, it is not feasible, for example, to parameterize reactor burnup with respect to transuranic isotopic stream compositions. Nor would it be possible to do so for repository performance with respect to changes in host medium physical properties or geometry.

The reactor submodel couples burnup and criticality calculations as seen in §2. The burnup portion of the model uses pre-tabulated physical data for each initially-present nuclide (neutron production and destruction rates, burnup, and isotopic transformation) that are functions of fluence. These input curves are specific to a given reactor and fuel type. The reactor model then uses mass-weighted superposition to recombine these isotopic parameters as needed to calculate the multiplication factor and maximum discharge burnup. This result is then folded in with a linear reactivity model for multi-batch criticality calculations that derive viable fresh fuel compositions. Since the

burnup, criticality, and transmutation information is parameterized per nuclide, this essential physics reactor submodel is more precise and perturbable than full-core linear correlation coefficients.

The repository thermal analysis model was developed based on the analytical solution of a thermal conduction model for the presence of loaded nuclear waste in a geologic repository [18]. The repository is modeled as a homogeneous hosting medium with constant properties. The nuclear waste packages were assumed to be loaded into parallel waste emplacement drifts. Each drift is treated as an infinite line heat source. The temperature increase at the critical location is the superposition of temperature increase from each drift. The undisturbed temperature field was assumed to be known, and the repository capacity was determined according to the appropriate thermal design constraints.

4.4.1 Fuel Cycle Schema

A sodium cooled fast burner (FR) - light water reactor (LWR) symbiotic cycle is studied here. It is more fully detailed in [16] and the corresponding flowchart is seen in Figure 4.2. Although the model computes recycle passes leading up to equilibrium [35], data (*i.e.* the system wide performance assessment metrics) are taken only after the fuel cycle has achieved its mass-balance equilibrium. The statistical techniques discussed below could be applied to any type of fuel cycle; in this study, the LWR and Na-cooled FR technologies were chosen for the fuel cycle simulation model in order to strike a reasonable
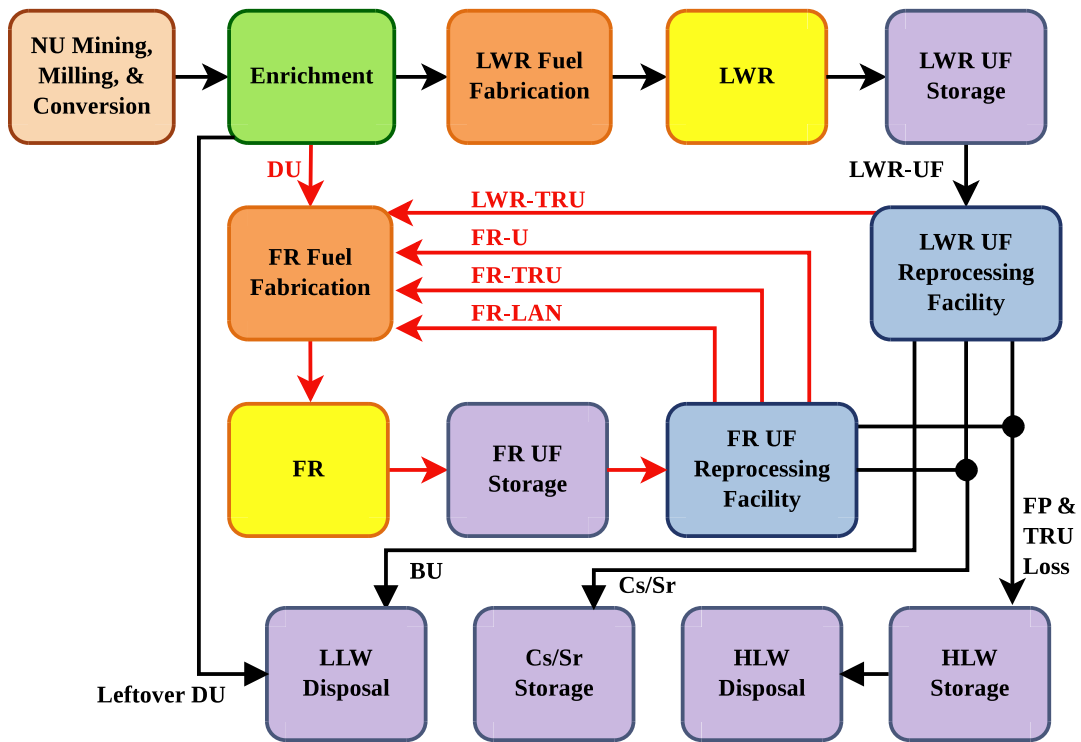
Figure 4.2: LWR-FR Symbiotic Fuel Cycle Scenario

balance between input space richness, complexity, and familiarity to readers.

The fast reactors exist in support of the current and near-future fleet of light-water reactors. The LWR used fuel (UF), after a cooling period, is sent to an aqueous reprocessing facility. Here the transuranics (TRU) are separated out from the fission products (FP) and the burned uranium (BU). The FP stream is further partitioned at the LWR fuel reprocessing plant. The cesium and strontium are separated out from the remaining FP. The Cs and Sr are then emplaced in a storage facility built for medium-lived isotopes while the BU goes to a low-level waste (LLW) disposal facility. The remaining FPs and any losses from the other streams (TRU, U, Cs/Sr) are treated as high-level waste (HLW) and sent to the repository for permanent disposal.

Meanwhile, the recovered transuranics from the LWR are mixed with depleted uranium (DU), and recycled FR uranium, TRU, and lanthanides (LAN). In this schema, all of the U and TRU discharged from a FR (less reprocessing losses) are recycled into the fast reactor. Additionally, the LAN are allowed to be recycled up to a certain maximal amount, if available. The remaining LAN mass joins the HLW stream and is sent to the repository. Hence the DU and LWR-TRU streams act as a top-up. By mixing in appropriate proportions (as calculated in [35]), new fuel for the fast reactors is created.

After being re-burned in the FR, the used fuel once again goes into cooling for three to thirty years. From here the fuel is sent to a FR fuel reprocessing facility. At the FR fuel reprocessing facility the actinide mass of FR-UF is separated from the fission products present. Again, the Cs and

113

Sr are separated from the remaining FP. The actinides and some of the lanthanides are sent back to the fast reactor, the Cs/Sr stream is disposed of in its own storage facility, and the non-Cs/Sr fission products and losses from other streams are sent to the deep geologic repository. After reprocessing but prior to emplacement in the repository, the high level waste stream is cooled for between one and three hundred years. The deep geologic repository itself is modeled after Yucca Mountain.

4.4.2 Implementation

The fuel cycle model has been benchmarked against OECD and Idaho National Laboratory (VISION) scenario analyses. When compared against the LWR-FR symbiotic cycle defined in Scheme 3a of the 2006 OECD fuel cycle system study [25], agreement to within 5% on the LWR-to-FR support ratio and uranium and plutonium isotopics in the equilibrium mass flows was seen. Full benchmark results are reported in §2-3. For further details on this LWR-FR symbiotic cycle refer to [39]. The LWR and FR input parameters defined in [39] and reproduced above are points of departure for the statistical analyses.

The essential physics methodology allows reactor performance and fuel cycle mass balances to be rapidly recalculated under perturbations to design and operating parameters, where feedbacks to the operation of the cycle may have global reach.

4.4.3 Parameter Specification

Stochastic parameters are sampled either in a linearly uniform, log uniform, or one-minus-log uniform fashion. The one-minus-log uniform distribution is useful for choosing separation efficiencies and is known as sampling in the 'nines'. Table 4.1 defines all thirty fuel cycle input parameters along with the six responses computed by the model. The scale column lists the sampling function and the binning method implemented (see §4.6.1) for each input parameter.

In the case where a set of input parameters is chosen such that the cycle is not physically calculable, internal variables inside of the models are adjusted to a point such that the fuel cycle is feasible. For example, suppose a vector of inputs specifies a high value of the LWR burnup as well as other default internal parameters. The reactor model will adjust the non-leakage probability, the initial enrichment of the fresh fuel, and the discharge fluence until these are tuned such that the stochastically declared burnup value is obtained.

Thus every fuel cycle realization is its own distinct cycle, tuned for the stochastic parameters selected. However, by bounding the input parameters and comparing many realizations, this study shows that the output parameters are also bounded. The spread of the output parameters due to changes in the inputs determines the relative importance of that input.

Table 4.1: Fuel Cycle Parameter Definition

Input Parameter x	Abbreviation	Min	Max	Units	Scale
LWR Burnup Level	LWR_BUd	30.0	80.0	MWd/kgIHM	linear
LWR Fuel to Moderator Ratio	LWR_Fuel2Mod	0.28	0.36		linear
LWR UF Storage Time	LWR_UF_Storage_Time	3	30	years	linear
SE of U from LWR UF	LWR_SE_U	0.99	0.9999		nines
SE of NP from LWR UF	LWR_SE_NP	0.9	0.9999		nines
SE of PU from LWR UF	LWR_SE_PU	0.9	0.9999		nines
SE of AM from LWR UF	LWR_SE_AM	0.9	0.9999		nines
SE of CM from LWR UF	LWR_SE_CM	0.9	0.9999		nines
SE of CS from LWR UF	LWR_SE_CS	0.9	0.9999		nines
SE of SR from LWR UF	LWR_SE_SR	0.9	0.9999		nines
FR Burnup Level	FR_BUd	100.0	200.0	MWd/kgIHM	linear
FR TRU Conversion Ratio	FR_TRU_CR	0.25	0.95		linear
Lanthanide Fraction in FR Fresh Fuel	FR_LAN_FF_Cap	0.0001	0.005	Atoms/TRU Atom	linear
FR UF Storage Time	FR_UF_Storage_Time	3	30	years	linear
HLW Storage Time	HLW_Storage_Time	1	300	years	log
SE of U from FR UF	FR_SE_U	0.99	0.9999		nines
SE of NP from FR UF	FR_SE_NP	0.9	0.9999		nines
SE of PU from FR UF	FR_SE_PU	0.9	0.9999		nines
SE of AM from FR UF	FR_SE_AM	0.9	0.9999		nines
SE of CM from FR UF	FR_SE_CM	0.9	0.9999		nines
SE of CS from FR UF	FR_SE_CS	0.9	0.9999		nines
SE of SR from FR UF	FR_SE_SR	0.9	0.9999		nines
Density of Host Rock	Rock_Density	2317	2869	kg/m^3	linear
Specific Heat of Host Rock	Rock_Specific_Heat	590	1270	J/kg-K	linear
Thermal Conductivity of Host Rock	Rock_Thermal_Conductivity	1.9204	3.2856	W/m-K	linear
Heat Loss Factor During Ventilation	Heat_Loss_Factor	0.806	0.914		linear
Drift Diameter	Drift_Diameter	4.5	6.5	m	linear
Ventilation System On Time	Vent_Stystem_On_Time	10	300	years	log
Ambient Environment Temperature	Ambient_Temp	12.82	32.82	C	linear
Distance Between Drifts	Drift_Space	56	106	m	linear
Response Parameter R					
Repository Capacity	Capacity	10^4	10^8	MTHM/Repository	log
Fuel Cycle Cost	Cost	4.0	8.0	\$/MWh	linear
LWR-FR HLW Ratio	HLW_Ratio	4.0	44.0	gHM/GWh	linear
LWR-FR Support Ratio	Support_Ratio	0.0	3.0	LWR cores/FR cores	linear
Total Electricity per Repository	Total_Electricity	5×10^8	5×10^{12}	GWh/Repository	log
Toxicity Index	Toxicity_Index	10^6	10^8	m^3/MTHM	log

4.5 Contingency Tables

After the stochastic generation of set of input parameters, the analysis loop of Figure 4.1 is entered. Since all inputs are varied simultaneously, the response from single input parameter is implicitly a function of all other inputs as well. With thirty inputs, all outcomes exist in a 31 dimensional space.

Therefore, if a deterministic sampling approach were used and one hundred points were chosen per input parameter, then 10^{60} fuel cycle realizations would be needed to have full coverage over all space.

Hence the stochastic method achieves much better coverage much faster. However, even one hundred thousand points may not *a priori* be enough. A mechanism for measuring the quality of the data will be discussed in §4.6.1.

Contingency tables (CT) [9, 30, 48] *associate* two parameters of a complex system in a way that is independent of the functional form of the actual system. Given that CTs have a rich history of their own, the authors seek not to fully characterize them. Rather, this analysis presents the use of contingency tables as a fuel cycle performance assessment tool.

A simple example illustrates the CT concept valuable to understanding the following analyses. For a fictitious sample population, a biologist may be interested in the correlation between hair color and sex. They might then set up a 2×2 tabulation similar to Table 4.2. Structurally, the matrix of data itself sits in the center, while marginal sums are displayed along the right and bottom.

Table 4.2: Hair Color to Sex Contingency Table

	Blonde	Brunette	Totals
Female	18	17	35
Male	11	14	25
Totals	29	31	60

Of note for Table 4.2 is that both sex and hair color can be interpreted as responses to underlying human biological mechanisms. Since the body is being treated as a black box, contingency tables do not distinguish between input and output parameters.

Additionally, Table 4.2 uses categorical, discrete variables. However, CTs may also be implemented using data that is a function of a continuous real variable, equally partitioned on the scale of interest. For instance, exponential data could have one bin per decade.

For the NFC and input parameter family considered here, all parameters are functions of a real (stochastic) continuous variable. This approach can support discrete variables too (e.g., a boolean flag indicating the availability of mixed-oxide fuel), but that avenue is not developed her. For the continuous variables, more than two bins are required to be able to demonstrate a meaningful association. It will be shown that 7 bins per axis on the contingency tables give rise to acceptable statistical fidelity. However, even seven bins becomes unwieldy for visualization. Table 4.3 displays a 4×3 fuel cycle CT from the data set computed in the Monte Carlo loop. This example compares the FR plutonium separation efficiency (SE) to the repository capacity,

Table 4.3: Contingency Table for FR Plutonium SE to Repository Capacity [MTHM/Repository].

	0.9 <SE< 0.99	0.99 <SE< 0.999	0.999 <SE< 0.9999	
$10^4 <$ Capacity $< 10^5$	739	43	27	809
$10^5 <$ Capacity $< 10^6$	31510	21611	19469	72590
$10^6 <$ Capacity $< 10^7$	2648	13095	14430	30173
$10^7 <$ Capacity $< 10^8$	0	213	1053	1266
	34897	34962	34979	104838

irrespective of what the values the other 29 system inputs take on.

The zero entry in Table 4.3 implies that for low plutonium separation efficiencies a high repository capacity is impossible. Additionally, some regions arise rarely, assumedly only for extreme values of one or more other inputs. High plutonium SE and low repository capacities occur with a vanishingly small probability. The combination of these two restricted regimes leads to a table that is largely banded down the diagonal. The statistical measures chosen for examination should capture these effects.

As mentioned previously, contingency tables are not restricted to a two-way formulation. Three dimensional tables may also be constructed from the same fuel cycle realizations. In an effort to capture co-variant system effects, this paper examines two independent parameters (x and y) and one response (R). For instance, if the SE of plutonium coming from the FR changes, it is expected that the relative benefit from the HLW storage period will also change. Thus the repository capacity must be expressed as a combination of these two parameters together.

Table 4.4: 3D Contingency Table Relating FR Plutonium SE and the HLW Storage Time [years] to the Repository Capacity [MTHM/Repository].

Slice for $1 <$ HLW_Storage_Time < 6.694				
	$0.9 <$ SE < 0.99	$0.99 <$ SE < 0.999	$0.999 <$ SE < 0.9999	
$10^4 <$ Capacity $< 10^5$	419	23	14	456
$10^5 <$ Capacity $< 10^6$	11145	9970	9553	30668
$10^6 <$ Capacity $< 10^7$	110	1556	2085	3751
$10^7 <$ Capacity $< 10^8$	0	0	0	0
	11674	11549	11652	34875
Slice for $6.694 <$ HLW_Storage_Time < 44.814				
	$0.9 <$ SE < 0.99	$0.99 <$ SE < 0.999	$0.999 <$ SE < 0.9999	
$10^4 <$ Capacity $< 10^5$	273	19	11	303
$10^5 <$ Capacity $< 10^6$	10859	7527	6373	24759
$10^6 <$ Capacity $< 10^7$	484	4157	5175	9816
$10^7 <$ Capacity $< 10^8$	0	2	24	26
	11616	11705	11583	34904
Slice for $44.814 <$ HLW_Storage_Time < 300				
	$0.9 <$ SE < 0.99	$0.99 <$ SE < 0.999	$0.999 <$ SE < 0.9999	
$10^4 <$ Capacity $< 10^5$	47	1	2	50
$10^5 <$ Capacity $< 10^6$	9506	4114	3543	17163
$10^6 <$ Capacity $< 10^7$	2054	7382	7170	16606
$10^7 <$ Capacity $< 10^8$	0	211	1029	1240
	11607	11708	11744	35059
Summary for summation over HLW_Storage_Time				
	$0.9 <$ SE < 0.99	$0.99 <$ SE < 0.999	$0.999 <$ SE < 0.9999	
$10^4 <$ Capacity $< 10^5$	739	43	27	809
$10^5 <$ Capacity $< 10^6$	31510	21611	19469	72590
$10^6 <$ Capacity $< 10^7$	2648	13095	14430	30173
$10^7 <$ Capacity $< 10^8$	0	213	1053	1266
	34897	34962	34979	104838

Table 4.4 has a $4 \times 3 \times 3$ bin structure relating the R response to x & y inputs. Here, it is essential to note that every y bin is itself a 2D contingency table for x to R. Additionally, the bottom slice in Table 4.4 represents the marginal sums over the y axis. Because x here was chosen the same as in the 2D case (FR_SE_PU), the last slice in Table 4.4 *is* Table 4.3. Moreover, the 2D CT

for `HLW_Storage_Time` to `Capacity` is represented by the right-hand column of Table 4.4. Since there are thirty inputs, of which two are examined, there are $_{30}C_2 = 435$ three dimensional contingency tables that may be constructed for every response.

4.5.1 Statistical Metrics

This section describes the statistical measures used to quantify the strength of association between input parameters and responses in contingency tables. This allows the system designer to determine the most 'important' input parameters to this response. For example, one could quantitatively state the degree of importance of FR plutonium separations relative to the repository drift diameter in the sense of how each affects the repository capacity.

4.5.1.1 Entropy

The *entropy H* of a parameter or CT is a measure of how evenly spread out the data is over all bins. This metric can be thought of in analogy to the thermodynamic property of the same name. For contingency tables, maximum entropy implies that all entries in the table have exactly the same value. Conversely, zero entropy implies a fully ordered system. In contingency tables, zero entropy implies that every row and every column have exactly one non-zero entry. All independent input parameters x should have maximum entropy since they are randomly sampled.

To calculate the entropy, the probability table corresponding to the

CT is needed. If there are N total Monte Carlo runs, then any bin in the contingency table may be represented by the matrix element N_{ab}. Here a indexes the number of response bins A, while b indexes the number of x input parameter bins B. For the three dimensional table, N_{abc} represents a matrix element where c indexes the number of y input parameter bins C. Thus the probability table may be defined such that:

$$p_{ab} = \frac{N_{ab}}{N} \; \forall a, b \in A \times B \tag{4.1}$$

Additionally, marginal sums are represented by a subscript dot notation. The 'dotted' index or indices are the rows or columns that are summed over. For example,

$$p_{\cdot b} = \sum_{a}^{A} p_{ab} \tag{4.2}$$

$$N = N_{\cdot\cdot} = \sum_{a,b}^{A,B} N_{ab} \tag{4.3}$$

Then, the entropy is defined as the sum of $p \log p$ for any parameter or parameter combination:

$$H(R) = -\sum_{a}^{A} p_{a\cdot} \ln(p_{a\cdot}) \tag{4.4}$$

$$H(x) = -\sum_{b}^{B} p_{\cdot b} \ln(p_{\cdot b}) \tag{4.5}$$

$$H(R, x) = -\sum_{a,b}^{A,B} p_{ab} \ln(p_{ab}) \tag{4.6}$$

The last entropy in the equations above, $H(R, x)$, is known as the *joint entropy* since it measures the entropy of the contingency table as a whole. Three

Figure 4.3: Relationship between the Mutual Information and Entropy [30]
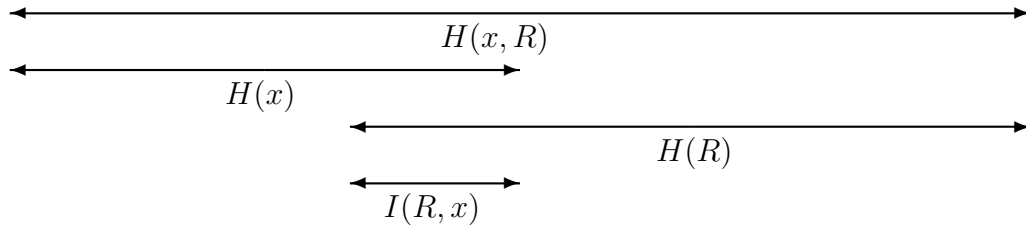
dimensional expressions for entropy may be extrapolated from the equations above.

Entropy is not neatly bounded on the range $[0, 1]$. Rather the maximum value for the entropy is given as the natural logarithm of the total number of bins K of any table or slice such that the entropy is defined on the range $[0, \ln(K)]$.

4.5.1.2 Mutual Information

The next metric is the *mutual information I*. The mutual information is defined as the overlap in the entropies of various parameters. Figure 4.3 graphically displays the relationship between the various entropies and the mutual information. This figure is based on a similar one presented in [30]. As a physical example, consider the DNA sequences of a parent and a child. The sequence of the child (R) is some unknown function of the DNA of the parent (x). $I(R, x)$ then measures the mutual dependence of the sequences, in entropy space.

123

The mutual information indicates how much of a response is determined by a particular input. As an illustration, FR UF separations might account for half of the variation in fuel cycle costs. However, FR burnup may also account for half of the variability. Yet, these halves likely have a significant overlap since both affect the amount of TRU top-up required on the next pass. The maximum possible overlap could be inferred by comparing the mutual information values for each of these two inputs.

The mutual information may be calculated in two- and three-dimensional senses as follows:

$$I(R, x) = -\sum_{a,b}^{A,B} p_{ab} \ln\left(\frac{p_{ab}}{p_{a\cdot} \cdot p_{\cdot b}}\right) \tag{4.7}$$

$$I(R, x, y) = -\sum_{a,b,c}^{A,B,C} p_{abc} \ln\left(\frac{p_{abc}}{p_{a\cdot\cdot} \cdot p_{\cdot b\cdot} \cdot p_{\cdot\cdot c}}\right) \tag{4.8}$$

The minimum value of I is zero, indicating that x and R share nothing in common. This occurs when x and R are fully independent. On the other hand, the maximum value of the mutual information depends on the structure of the contingency table and may not be easily expressed in general.

4.5.1.3 Uncertainty

The uncertainty U is the first metric to be used to rank the relative value of input parameters to a response. Informally, the uncertainty is defined as the mutual information divided by the entropy because it represents the fraction of the response which is predictable given an input.

More exactly, the *uncertainty coefficients* are used to rank inputs. They are specified with the conditional notation $U(x|R)$. Such coefficients are calculated via [48]:

$$U(x|R) = \frac{I(R, x)}{H(x)} \tag{4.9}$$

$$U(R|x) = \frac{I(R, x)}{H(R)} \tag{4.10}$$

Equation 4.9 measures the extent to which knowing the input x is the same as knowing the response R. As such, $U(x|R)$ has the following properties:

1. Defined on the range $[0, 1]$.

2. $U(x|R) = 0$ implies that $I(R, x) = 0$, which indicates that the parameter is unassociated with the response.

3. $U(x|R) = 1$ requires that $I(R, x) = H(x)$. This implies that the system response $R(x)$ is solely determined by x.

It is important to note that both $H(R)$ and $H(x)$ do not change as a function of x. $H(R)$ is itself not a function of x. Moreover since all of the x are chosen stochastically, $H(x)$ always has its maximal value. Thus the rankings of x from $U(x|R)$ are the same as the rankings from the, perhaps more natural, uncertainty coefficient $U(R|x)$. Hence, the scaling factor seen in equation 4.11 is the same for all inputs.

$$U(x|R) = \frac{H(R)}{H(x)}U(R|x) \tag{4.11}$$

This scaling factor is obtained by combining equations 4.9 & 4.10 via the mutual information term.

Moreover, a related uncertainty coefficient may be calculated for the three dimensional case of two inputs to one response. $U(x, y|R)$ is computed from:

$$U(x, y|R) = \frac{I(R, x, y)}{H(x, y)} \qquad (4.12)$$

The reason for choosing $U(x, y|R)$ as opposed to $U(R|x, y)$ follows analogously to the two dimensional case.

The interpretation of $U(x, y|R)$ is much the same as the meaning of $U(x|R)$. The difference here is that input parameter pairs are being compared to all other (x, y) combinations. For instance, by ranking with this 3D metric, the fuel cycle analyst may quantitatively state that the FR plutonium and americium SEs together are more important to the repository capacity than the repository drift diameter together with the LWR neptunium SE.

4.5.1.4   Sensitivity of Sensitivity Metrics

In so far as the uncertainty coefficient is a surrogate for sensitivity, a suitable replacement for covariance should be found. This sort of association is called a *sensitivity of sensitivity* because it seeks to quantify the sensitivity of x given the sensitivity of y to the response R.

To obtain such a metric, recall that each slice of a three-way table is itself a 2D contingency table. It is therefore possible to compute the uncertainty

coefficient $U(x|R)$ for every slice over y. In doing so, a set of C uncertainties are generated such that,

$$\{U(x|R)|y\} = \left\{ U(x|R)|_{l_0}^{l_1}, U(x|R)|_{l_1}^{l_2}, \ldots U(x|R)|_{l_{C-1}}^{l_C} \right\} \tag{4.13}$$

where l is a sequence of $C + 1$ points that defines the bin boundaries of y. From here, the mean μ and standard deviation σ of the set seen in equation 4.13 may be calculated.

$$\mu(\{U(x|R)|y\}) = \frac{1}{C} \sum_{c}^{C} \{U(x|R)|y\}_c \tag{4.14}$$

$$\sigma(U(x|R)|y) = \sqrt{\frac{1}{C} \sum_{c}^{C} (\{U(x|R)|y\}_c - \mu(\{U(x|R)|y\}))^2} \tag{4.15}$$

However, the choice of slicing along y is somewhat arbitrary. One could instead slice along x and compute $\mu(\{U(y|R)|x\})$ and $\sigma(\{U(y|R)|x\})$ by analogy to the equations above.

Dividing the standard deviation by the mean yields a *coefficient of variation* c_v:

$$c_v(\{U(x|R)|y\}) = \frac{\sigma(\{U(x|R)|y\})}{\mu(\{U(x|R)|y\})} \tag{4.16}$$

Unlike the uncertainty coefficient, $c_v(\{U(x|R)|y\})$ is not symmetric with respect to x and y. Thus the same pair will have a different rank when measuring with $c_v(\{U(y|R)|x\})$ instead. A symmetric expression of the coefficient of variation is obtained by taking the average of the non-symmetric terms:

$$c_v(x|y|R) = \frac{1}{2} \left(c_v(\{U(x|R)|y\}) + c_v(\{U(y|R)|x\}) \right) \tag{4.17}$$

This measure has the following properties:

1. Defined on the range $[0, 1]$ since $0 \leq U \leq 1$.

2. $c_v(x|y|R) = 0$ implies that $\sigma = 0$, which indicates that $U(x|R)$ shows no dependence on y. Thus there are no covariant effects observed.

3. $c_v(x|y|R) = 1$ indicates that $\sigma = \mu$. This connotes that the value of x soley governs the response R from y.

The difference in ranking parameter pairs using $U(x, y|R)$ rather than using $c_v(x|y|R)$ is that the uncertainty coefficient measures the magnitude of the effect on R while the coefficients of variation measure the interdependence of x and y on the response. For example, the HLW storage time together with the LWR UF storage time are not of global importance to the repository capacity (low $U(x, y|R)$ value). However, changing one input has a great effect on the impact of other input to the repository capacity (high c_v value). Therefore, both metrics are needed to have a complete description of the three dimensional contingency tables.

4.6 Results & Case Studies

The goal of using CTs, similar to other sensitivity studies [34] or uncertainty analyses [3], is to quantitatively rank fuel cycle inputs against their effect on the chosen response. Here, the two dimensional uncertainty $U(x|R)$ takes the place of a traditional sensitivity. Likewise, the three dimensional $U(x, y|R)$ may be seen as a sensitivity for a pair of parameters. Lastly, the coefficient of variation $c_v(x|y|R)$ is taken as a measure of covariance effects

between x and y. The covariance metric shows that some parameter pairs have a significant joint effect on the fuel cycle. Hence, x and y may exhibit a greater (or less than) commensurate response on the fuel cycle response than the sum of x and y effects individually.

A brief examination of the binning structure and how it was determined follows. Then, an illustration of the rankings of all fuel cycle metrics for the 2D & 3D sensitivities and covariant analyses is presented. The final portion of this section reviews case studies about particular parameters and parameter pairs of interest.

4.6.1   Binning Structure

Inevitably when performing Monte Carlo calculations the question of 'good statistics' arises. At the root of this question is the concern that enough runs have been performed to ensure that the subsequent analysis can be made with confidence.

Moreover, contingency tables exhibit dynamic effects as a function of the number of bins used to generate them, even for the same underlying data set. An example from thermodynamics demonstrates this behavior. Take a chamber the moment after a piston has been suddenly removed, as in a Carnot heat engine. This system is not at its highest entropy. Most of its fluid lies in the part of the chamber that was not compressed by the piston while most of the chamber remains evacuated.

Now, to capture the state of the piston, impose imaginary partitions at

129

Figure 4.4: Abstract Piston with Representative Partitions: Blue Line for 2 Bins, Red Line for 5 Bins.

equidistant points in the chamber. A diagram of this is seen in Figure 4.4. The blue dotted line represents partitioning the piston chamber into two distinct bins. The particle distribution is heavily weighted to the leftmost bin since this is where the large majority of the fluid (yellow dots) falls.

The red dotted lines in Figure 4.4 represent the same chamber partitioned into five bins. The left most red partition runs through the densely populated region, adding information about the distribution that was not available under the more coarsely-binned structure.

From this one might conclude that only an infinite number of partitions and bins would converge to the 'true' value of the entropy. However, this is not necessary for contingency tables. The metrics (entropy, uncertainty, *et cetera*) rely on the relative populations of the bins. An infinite number of partitions would result in zero or one particle per bin, thereby giving poor statistics.

Thus there is a balancing act between the number of bins and the number of stochastic simulation executions. This study uses a symmetric seven bins per axis formulation. (Two dimensional tables have $7^2 = 49$ bins

while the three dimensional tables have $7^3 = 343$ bins.) Such behavior is consistent with other Monte Carlo techniques [30].
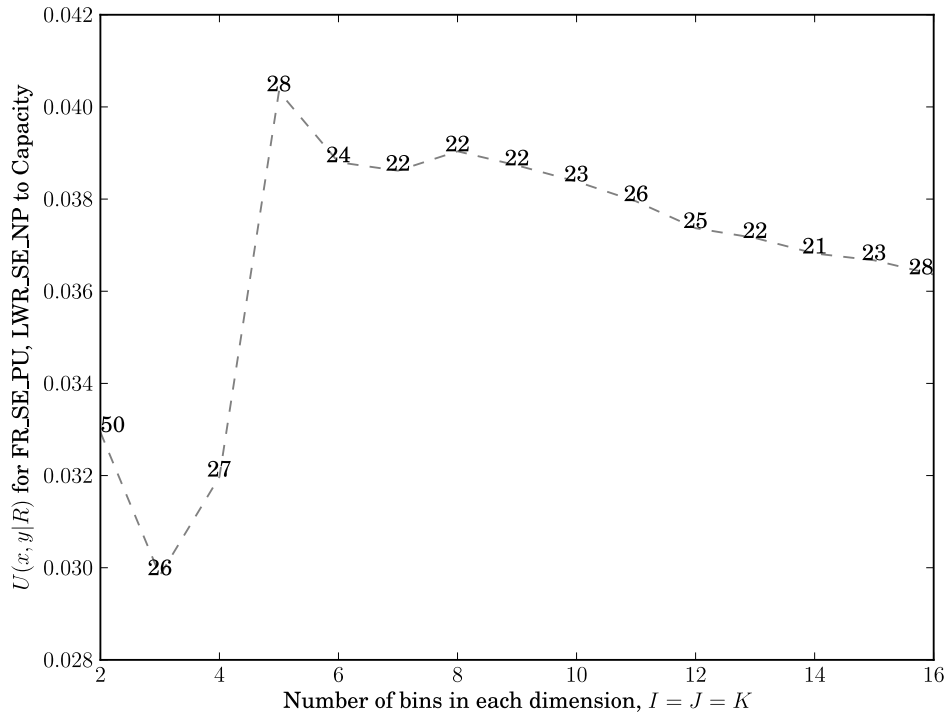
Figure 4.5: Dynamic Effects of Binning Structure Example: $U(x, y|R)$ for the parameter pair (FR_SE_PU, LWR_SE_NP) to repository capacity.

Seven bins per axis were chosen since the uncertainty rankings for moderately important parameter pairs stabilize at approximately this point. While the choice of binning resolution is system-specific – it depends on the dynamics of the underlying simulation model – important parameters are always going to dominate the top ranks and non-important ones will change ranks rapidly,

but randomly. Therefore it is necessary to examine the parameters which are most sensitive to the binning effects.

Figure 4.5 shows how the 3D sensitivity $U(x, y|R)$ for FR plutonium separation efficiency and LWR neptunium separation efficiency given the repository capacity changes as a function of symmetric bin structure (*i.e.* $A = B = C$). It is known that FR_SE_PU is very important while LWR_SE_NP is not. Therefore the combination of these two inputs has some modest impact largely driven by the plutonium vector.

Figure 4.5 displays both the value of the uncertainty metric for this parameter pair as well as its relative ranking to all other pairs. Lower ranks $(1, 2, \ldots)$ indicate more important parameters while higher ranks $(\ldots, 29, 30$ or $\ldots, 434, 435)$ mean that the parameter has less overall impact. From this figure, the importance of (FR_SE_PU, LWR_SE_NP) fluctuates significantly from 50 to the mid-twenties for low symmetric bin number. However once 7 bins are reached, the rank stabilizes at 22. This stability indicates that the repository capacity response to changes in FR_SE_PU and LWR_SE_NP, relative to the response for similarly important parameter pairs, becomes well-captured at 7-bin resolution.

After 10 bins, the rank creeps up and down. This is expected as the number of fuel cycle realizations remains constant for all bin numbers. Thus higher bin numbers relate to correspondingly worse statistics for the contingency table (see below). The goal, therefore, is to pick the lowest bin number after which the rankings have become stable. Such a point for this study seems

to lie at approximately 7 bins per axis. Studies have been made of several other parameter pairs to support this conclusion.

The mutual information may be used to ensure that the binning structure offers satisfactory statistics given the number of stochastic realizations available. Since every input parameter is independent of every other input parameter, $I(x, y)$ should be zero for all combinations of x and y in the limit as N becomes large.

Call t the maximum acceptable tolerance along any stochastic axis. For instance, $t = 0.01$ indicates a 1% intrinsic uncertainty. Then the threshold mutual information for 'good' statistics goes as $I(x, y) \approx t^2$, since two stochastic parameters are being compared. The approximate number of runs required to achieve t is thus:

$$N \approx \frac{1}{t^2} BC \tag{4.18}$$

Thus by equation 4.18, it is a factor of 25 times easier to achieve 5% uncertainty than to get to the 1% level for the same binning structure. Given 10^5 runs performed here and seven bins on each axis, equation 4.18 implies that the induced uncertainty is approximately 2.2%. Seven bins per axis are used for the remainder of this analysis.

4.6.2 Rankings: One Input to One Response

Determining the impact of a single input parameter on a nuclear fuel cycle outcome is the first step in a screening study. Using the contingency

Table 4.5: Input Parameters Ranked by $U(x|R)$ for `Capacity` [MTHM/Repository]

Rank	x	$U(x|R)$
1	FR_SE_PU	0.07667
2	HLW_Storage_Time	0.05264
3	FR_SE_AM	0.04148
4	Heat_Loss_Factor	0.01548
5	LWR_SE_PU	0.01343
6	FR_TRU_CR	0.008895
7	LWR_SE_AM	0.007304
8	FR_BUd	0.003773
9	LWR_SNF_Storage_Time	0.003551
10	Rock_Specific_Heat	0.003085
11	FR_SE_CM	0.002522
12	Rock_Thermal_Conductivity	0.001954
13	Ambient_Temp	0.001353
14	LWR_BUd	0.001053
15	LWR_SE_CS	0.001033
16	LWR_SE_SR	0.001024
17	FR_SNF_Storage_Time	0.0005559
18	Drift_Space	0.0004421
19	LWR_SE_U	0.0002899
20	Rock_Density	0.0002718
21	FR_SE_CS	0.0001331
22	FR_SE_SR	0.0001073
23	Vent_System_On_Time	0.0001016
24	Drift_Diameter	9.648E-05
25	LWR_SE_NP	9.575E-05
26	LWR_SE_CM	7.969E-05
27	LWR_Fuel2Mod	7.833E-05
28	FR_LAN_FF_Cap	6.559E-05
29	FR_SE_NP	6.212E-05
30	FR_SE_U	6.207E-05

table methodology above, the uncertainty coefficient $U(x|R)$ measures the importance of x. Table 4.5 displays the input parameters, ranked by uncertainty, for the repository capacity response.

As expected, the fast reactor plutonium separation efficiency is shown to be the driver of the system. How much more important this parameter is that the other inputs may be quantitatively stated by taking the ratio of the two $U(x|R)$. For instance, LWR_SE_AM, the parameter at rank 7, has an uncertainty of 0.007304. Meanwhile FR_SE_PU has an uncertainty of 0.07667. The ratio of these uncertainties, and thus the magnitude of the effects on relative repository capacity, is 10.5.

From Table 4.5, most inputs have at least an order of magnitude less impact than the most important one, FR_SE_PU. This bottom heavy distribution indicates that there are only a handful of fuel cycle parameters which strongly drive repository capacity over even part of the range on which they are varied. Namely, they are the LWR & FR plutonium SE, the HLW storage time, the FR americium SE, and the repository heat loss factor.

However, this only addresses a single response in a large and coupled system. Similar rankings could be computed in analogy to Table 4.5 for all other responses. For example, even fewer inputs were found to be drivers of the LWR/FR support ratio than drive the repository capacity. The sole parameter above 0.1 uncertainty is, predictably, the fast reactor conversion ratio. The only two inputs on the range $[0.001, 0.01]$ are the LWR & FR burnups. Thus all 27 other inputs are at least two orders of magnitude less important than

the top one for the `Support_Ratio`.

Even though the input rankings may change dramatically for different responses, a short list of the most important may be determined from the union of all top inputs for all responses. Moreover, some responses tend to produce similar rankings because their values are derived from other responses. This also limits the overall number of top parameters.

One non-intuitive result from the 2D study is that the cesium and strontium separation efficiencies do not appear higher in the ranks. Indeed, the reason for partitioning these species is *because* of their large impact. They are ranked relatively low here because by the point of 0.9 separations for these species (the lower bound of the SE range) has been achieved, most of their repository impact has been mitigated.

4.6.3   Rankings: Two Inputs to One Response

The analysis of three dimensional contingency tables follows in two parts. The first is a ranking of associations of input parameter pairs, analogous to the 2D case. Second, covariance effects between the two inputs are measured.

4.6.3.1   3D Sensitivity

The three dimensional expression of the uncertainty coefficient, $U(x, y|R)$, is used to capture the strength of association from a parameter pair to the response. Therefore a table similar to Table 4.5 would show the rankings of all 435 parameter pairs to the repository capacity.

136

However, from the previous 2D study, the `FR_SE_PU` is known to be the most important single parameter to repository capacity by a wide margin. Because of this overwhelming impact, `FR_SE_PU` appears as a member of 29 of the top 30 pairs in the 3D sensitivity study. In fact, the only pair in the top thirty which does not contain FR plutonium SE is the rank 3 pair (`FR_SE_AM`, `HLW_Storage_Time`), which simply matches the rank 2 & 3 inputs from the two-dimensional contingency tables. Thus if an input is important by its own merits, any pair that this input is a member of is likely to also have a large system-wide effect. Since little additional information is added here over the 2D study, the 3D sensitivity tables are not displayed.

4.6.3.2 3D Sensitivity of Sensitivity

As was seen in section 4.6.3.1, the three dimensional uncertainty coefficient did not reveal fundamentally different information about the system than the two dimensional rankings. $U(x, y|R)$ coupled important inputs together, but which inputs were important remained the same. This was due to the fact that inputs were still being measured against a response.

How one input affects the impact of another input is a critical issue to the system designer. For example, one would want to know that the gains made by changing the `FR_SE_PU` would thrust another, previously unimportant, system design parameter to the fore. As a second example, if `HLW_Storage_Time` and `LWR_UF_Storage_Time` are seen to have a strong joint effect, it may mean that pursuing a strategy of extensive pre-emplacement storage would require

137

Table 4.6: Top 10% Input Parameter Pairs Ranked by $c_v(x|y|R)$ for `Capacity` [MTHM/Repository]

Rank	x	y	$c_v(x|y|R)$
1	FR_SE_AM	HLW_Storage_Time	0.02318
2	FR_SE_AM	FR_SE_PU	0.02316
3	HLW_Storage_Time	LWR_UF_Storage_Time	0.01557
4	FR_SE_PU	HLW_Storage_Time	0.01556
5	HLW_Storage_Time	LWR_SE_PU	0.01155
6	FR_SE_AM	FR_TRU_CR	0.01061
7	FR_SE_PU	LWR_UF_Storage_Time	0.008192
8	FR_SE_PU	LWR_SE_PU	0.008
9	FR_BUd	FR_SE_AM	0.007716
10	Ambient_Temp	FR_SE_PU	0.007489
11	Ambient_Temp	HLW_Storage_Time	0.007367
12	HLW_Storage_Time	LWR_SE_AM	0.007248
13	Ambient_Temp	FR_SE_CS	0.007235
14	Ambient_Temp	LWR_Fuel2Mod	0.007066
15	Ambient_Temp	Heat_Loss_Factor	0.007044
16	Ambient_Temp	Rock_Specific_Heat	0.007013
17	Ambient_Temp	FR_SE_NP	0.00698
18	Ambient_Temp	Drift_Diameter	0.006958
19	Ambient_Temp	FR_SE_AM	0.006935
20	Ambient_Temp	LWR_SE_PU	0.006906
21	FR_SE_CM	HLW_Storage_Time	0.006894
22	Ambient_Temp	LWR_SE_CS	0.006864
23	Ambient_Temp	Drift_Space	0.006842
24	Ambient_Temp	FR_SE_U	0.006839
25	Ambient_Temp	FR_SE_CM	0.006795
26	Ambient_Temp	FR_SE_SR	0.006792
27	Ambient_Temp	FR_LAN_FF_Cap	0.006775
28	Ambient_Temp	LWR_SE_CM	0.006773
29	Ambient_Temp	LWR_SE_AM	0.006763
30	Ambient_Temp	LWR_SE_U	0.006726
31	Ambient_Temp	LWR_BUd	0.006714
32	Ambient_Temp	FR_UF_Storage_Time	0.006704
33	Ambient_Temp	LWR_SE_SR	0.006695
34	Ambient_Temp	Rock_Density	0.006676
35	Ambient_Temp	FR_BUd	0.006667
36	Ambient_Temp	LWR_SE_NP	0.006663
37	Ambient_Temp	Vent_System_On_Time	0.006651
38	Ambient_Temp	Rock_Thermal_Conductivity	0.006595
39	Ambient_Temp	FR_TRU_CR	0.006588
40	Ambient_Temp	LWR_UF_Storage_Time	0.006544
41	FR_BUd	FR_SE_PU	0.006506
42	HLW_Storage_Time	LWR_SE_CS	0.006502
43	FR_SE_CM	FR_SE_PU	0.006427
44	FR_SE_PU	FR_TRU_CR	0.006298

lengthier pre-separation used fuel storage to be most effective.

These sensitivities of sensitivities are measured in terms of the coefficient of variation c_v, as described in section 4.5.1.4. Table 4.6 shows the top 10% of 435 ranked parameter pairs for $c_v(x|y|R)$ for the repository capacity. As expected, the top parameters from before (FR_SE_PU, FR_SE_AM, & HLW_Storage_Time) all exhibit large effects on the impact of the others.

An input that is present in most of the top pairs in Table 4.6 is the ambient environment temperature of the repository. In many cases, this makes intuitive sense. The majority of the inputs that Ambient_Temp is paired with here are those that affect the composition of material in the repository (*i.e.* the various SE, the FR conversion ratio, the LWR fuel to moderator ratio). Moreover, the Ambient_Temp itself may be seen as a metric of remaining heat capacity in the repository while the material composition determines the heat load. Thus the fact that such parameter pairs exhibit strong covariances is not surprising.

4.6.4 Case Studies

4.6.4.1 Covariance of Plutonium & Americium Separations

Plutonium and americium separation efficiencies provide an intuitive example of the covariance measure. There is already known to be a strong coupling between these two parameters with respect to the repository capacity [36]. From the 2D sensitivity study, both FR_SE_PU and FR_SE_AM are highly ranked inputs. They exhibit a high covariance because ^{238}Pu and ^{241}Am are in direct competition for being the top heat load contributor to the repository.

Therefore, the degree to which plutonium is recycled in the FR relative to that of americium shifts repository performance in a way that may have a greater impact than when altering FR_SE_PU and FR_SE_AM in tandem.
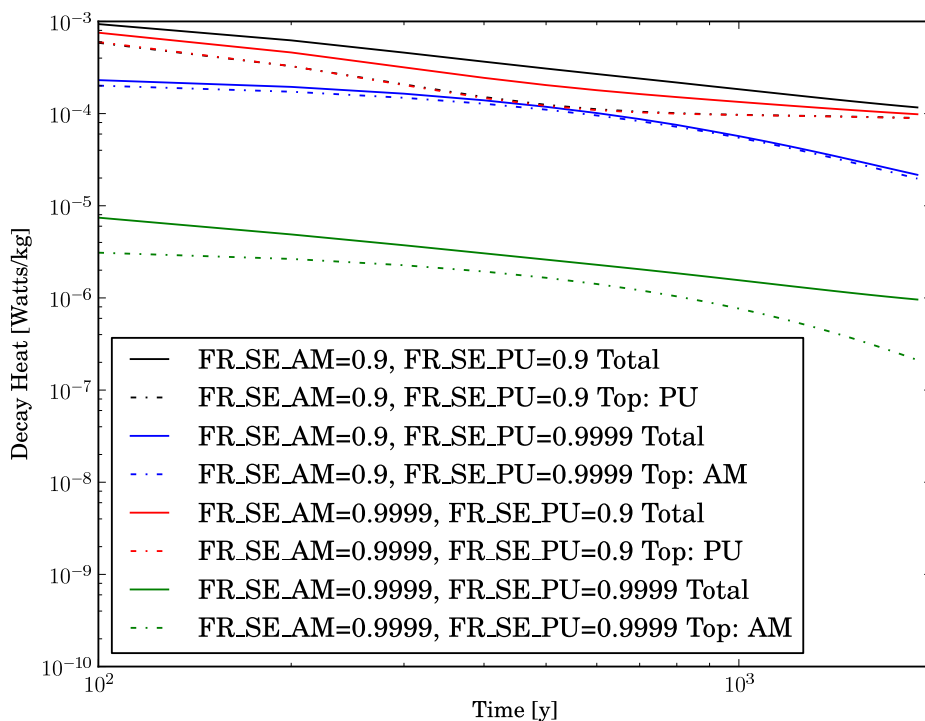
Figure 4.6: Total & Top Contributor Decay Heat [Watts/kg] of HLW for the parameter pair (FR_SE_AM, FR_SE_PU).

Such covariant effects are visible in Figure 4.6. Low values of FR_SE_PU and FR_SE_AM have high decay heats and high values have low decay heats. However, for the middle cases where one parameter is high and one is low, the top contributor takes on the value of the low separation efficiency. The switch

between Am/Pu and the two order of magnitude range in the decay heat is captured by the covariance metric.

4.6.4.2 Covariance of Americium Separations and FR TRU Conversion Ratio

Table 4.7: Probability Table for FR Americium Separation Efficiency & FR Transuranic Conversion Ratio to Repository Capacity [MTHM/Repository].

	$0.9 < $ FR_SE_AM < 0.99	$0.99 < $ FR_SE_AM < 0.999	$0.999 < $ FR_SE_AM < 0.9999	
Slice for $0.25 < $ FR_TRU_CR < 0.483				
$10^4 < $ Capacity $< 10^5$	2.10E-04	7.63E-05	5.72E-05	3.43E-04
$10^5 < $ Capacity $< 10^6$	8.94E-02	6.31E-02	5.97E-02	2.12E-01
$10^6 < $ Capacity $< 10^7$	2.14E-02	4.70E-02	4.71E-02	1.15E-01
$10^7 < $ Capacity $< 10^8$	1.91E-05	1.46E-03	4.12E-03	5.60E-03
	1.11E-01	1.12E-01	1.11E-01	3.34E-01
Slice for $0.483 < $ FR_TRU_CR < 0.717				
$10^4 < $ Capacity $< 10^5$	1.14E-03	4.20E-04	3.43E-04	1.90E-03
$10^5 < $ Capacity $< 10^6$	9.68E-02	7.09E-02	6.64E-02	2.34E-01
$10^6 < $ Capacity $< 10^7$	1.22E-02	4.01E-02	4.10E-02	9.33E-02
$10^7 < $ Capacity $< 10^8$	0.00E-00	7.25E-04	2.79E-03	3.51E-03
	1.10E-01	1.12E-01	1.11E-01	3.33E-01
Slice for $0.717 < $ FR_TRU_CR < 0.95				
$10^4 < $ Capacity $< 10^5$	3.37E-03	1.05E-03	1.06E-03	5.48E-03
$10^5 < $ Capacity $< 10^6$	1.02E-01	7.49E-02	6.92E-02	2.46E-01
$10^6 < $ Capacity $< 10^7$	6.00E-03	3.46E-02	3.84E-02	7.90E-02
$10^7 < $ Capacity $< 10^8$	0.00E-00	2.29E-04	2.74E-03	2.97E-03
	1.11E-01	1.11E-01	1.11E-01	3.33E-01
Summary for summation over FR_TRU_CR				
$10^4 < $ Capacity $< 10^5$	4.71E-03	1.55E-03	1.46E-03	7.72E-03
$10^5 < $ Capacity $< 10^6$	2.88E-01	2.09E-01	1.95E-01	6.92E-01
$10^6 < $ Capacity $< 10^7$	3.96E-02	1.22E-01	1.26E-01	2.88E-01
$10^7 < $ Capacity $< 10^8$	1.91E-05	2.41E-03	9.64E-03	1.21E-02
	3.33E-01	3.35E-01	3.33E-01	1.00E+00

The interplay between the FR americium SE and the FR transuranic conversion ratio exhibits a covariance to the repository capacity. As seen in Table 4.6, these two inputs display a relatively high sensitivity of sensitivity. The covariance effect here is confirmed by examining Table 4.7.

Table 4.7 displays the probability table, which is a normalized representation of the contingency table. This table shows that repository capacity

increases with increasing `FR_SE_AM`, a result consistent with the previous case study. On the other hand, with increasing `FR_TRU_CR`, the repository capacity *decreases*. Moreover, the peak of the repository capacity distribution as a function of americium separations increases with increasing `FR_TRU_CR`.

This covariance effect is due in part to the fact that the `FR_TRU_CR` is the major driver of the support ratio. As the conversion ratio increases, the mass of LWR UF required per kilogram of FR fresh fuel decreases. Therefore all components downstream from the FR become correspondingly more important; there are simply fewer LWRs. In specific, the relative impact of `FR_SE_AM` increases.

Due to increasing `FR_TRU_CR`, the americium contribution (as measured through ^{241}Am) negatively affects the repository capacity. At high conversion ratios, there is more high Am content FR UF per unit nuclear electricity produced. This in turn implies that the packing density of used fuel per meter of drift tunnel goes down. Therefore the total mass of heavy metal (`Capacity`) that may be stored in a fixed-size repository decreases.

4.6.4.3 Covariance of HLW Storage Time & Fast Reactor Plutonium Separations

`FR_SE_PU` and `HLW_Storage_Time`, the top two inputs from the sensitivity study, appear to exert a strong joint effect on the outcome. According to Table 4.6, this input pair is ranked fifth with respect to $c_v(x|y|R)$. Through an examination of the the 3D contingency table, high repository capacities are

only allowed when both FR_SE_PU and HLW_Storage_Time are high. Similarly, low capacities occur for low values of the two inputs. Middle values for either of the inputs yield middling capacities. Additionally, the entropy increases with increasing FR_SE_PU and HLW_Storage_Time.
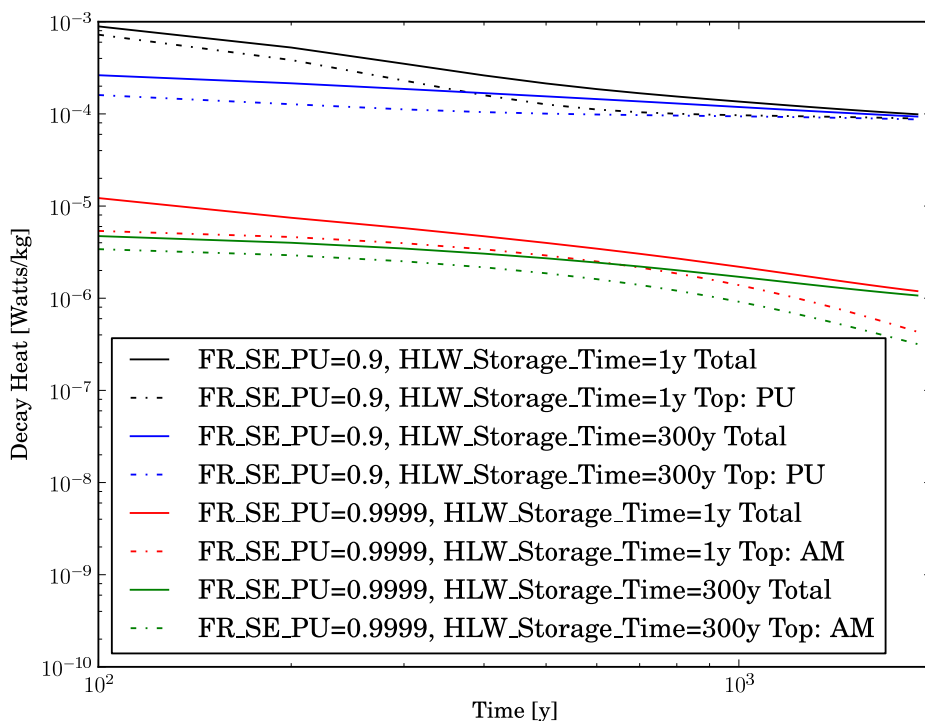
Figure 4.7: Total & Top Contributor Decay Heat [Watts/kg] of HLW for the parameter pair (HLW_Storage_Time, FR_SE_PU).

Physically, the reason for this covariance is because the HLW storage time effectively shifts the opening time of the repository. By having a long HLW_Storage_Time, the short- and medium-term repository temperature limits

143

may be avoided. Figure 4.7 displays the decay heat for the HLW and for the top elemental contributor to the decay heat as a function of time after emplacement in the repository. The curves here represent the four corner cases of the input values.

The time shift effect may be observed by holding `FR_SE_PU` constant and comparing curves on Figure 4.7 where `HLW_Storage_Time` is one year to the curves where the storage time is three hundred years. Points on the 1 year curves have roughly the same value as the 300 year HLW storage time curves, only 300 years farther in the future. By shifting the 1 year data three hundred years to the left, the two curves would nearly overlap. The statistical analysis confirms the strong importance to repository capacity of a strategy of 'waiting out' the decay of ^{238}Pu if plutonium separation efficiencies are low, and its much weaker importance if efficiencies are high.

4.7   Concluding Remarks & Future Work

The statistical techniques of contingency table and entropy analysis presented are widely-used tools for capturing the behavior of complex systems, particularly biological ones. Here they have been applied to a simulator of the nuclear fuel cycle. NFC outcomes, like those of any complex system, are shaped by intricate and highly nonlinear interactions between many inputs.

The strength of association between the inputs and the outcome studied here, the capacity of a Yucca Mountain-like repository, was quantified through uncertainty coefficients. Three-dimensional uncertainties were augmented by a

144

coefficient of variation to determine the system response inputs acting jointly. The latter is especially important because alternative approaches, for instance linear sensitivity analyses, can only capture the response to departures from a reference state. This reference state is defined by the values assumed by dozens or hundreds of system inputs, each of which may be varied by system or technology designers. It was shown that the coefficient of variation could illuminate dependencies where changes in one input have a strong effect on the system response to another.

This tool can aid system designers by helping them perceive which design variables matter. The contingency tables represent a (coarsely-gridded) importance map for the inverse problem. Conditioned on a specific system response, like repository capacity, the measure of the strength of response provided by the uncertainty coefficients can provide guidance to technologists designing system parameters in the face of uncertainty regarding the shape of the larger system. Illuminating joint dependencies, coefficients of variation can guide iterative technology development by showing which design features must be considered together.

The approach described here can be generalized to include boolean as well as continuous inputs. For example, if the technology ultimately chosen for the permanent repository is unknown, a boolean flag can allow each stochastic realization to follow one of several options. The outcome, still repository capacity, would now be conditioned on this boolean input as well. It would illuminate system design parameters that will be important regardless of tech-

145

nology ultimately chosen, those that have strongly technology-dependent effects, and those that are unimportant to determining capacity regardless of technology.

Still, the entropy-based analysis tools presented here are only as accurate as the underlying essential physics models. Therefore one method to increase the fidelity of CT-based analysis would be to address the assumptions made in the reactor model. By allowing multiple energy groups, spectral shifts in the core during burn could be adequately accounted for. §5 presents such adjustments to the reactor model, which in turn would propagate an increase in fidelity up through to the statistical metrics demonstrated above.

Chapter 5

Multigroup Reactor Methodology

5.1 Introduction

Previous studies have examined the use of quickly executing fuel cycle models focusing on capturing the essential physics [16]. Unlike analytic techniques which seek to solve fundamental physical systems (*e.g.* neutron transport) and then directly couple these models together, essential physics codes parameterize the system. Interpolations of parameterized results from precomputed analytic methods form a quick, run-time solution to the system at hand.

Such methods may be used for any fuel cycle component: enrichment, reactors, reprocessing, repositories, *etc.* However, their greatest advantage comes for such components whose analytic techniques are computationally intensive. Thus previous work has focused on reactors and repositories [18,35].

The quickly executing reactor methodologies to date have been one-energy group, fluence-based parameterizations [33]. Neutron production & destruction rates and transmutation matrices as a function of fluence (time-integrated flux) were recorded for each species initial present in the core. A linear combination of the initial nuclides was then used to compute the mul-

tiplication factor, fuel burnup, and used fuel vector at discharge.

Because the one-group cross sections used in a manner independent of burnup, the parameterizations in the previous model were not sensitive to changes in the flux spectrum over the course of the burn. The requirement of static cross sections limits the type of reactors that may be studied and is a severe restriction on the fidelity of such models. In seeking to enhance the fidelity of the parametric approach, the flux spectrum evolution and cross section changes must be folded back into the underlying parameterization.

Hence, a multi-energy group reactor model is proposed which will account for changes in the neutron flux spectrum as a function of burn time and other reactor attributes. Because the neutron flux is not constant, parameterization in terms of fluence is no longer an optimal choice. Instead, the reactor library contains cross section data as a function of burn time under a constant power irradiation. The reactor model uses perturbations of these cross sections to compute the same information as in the one-group formulation. Namely, the multiplication factor, fuel burnup, and fuel vector at all desired burn times are calculated. By necessity, the flux spectrum itself is also solved for.

The purpose of this new multiple energy group reactor model, like with the one-group model, is to execute as quickly as possible. Unlike in the one-group model, energy-dependent physics will be included. This will enable the inclusion of additional reactor types in an essential physics fuel cycle model (see discussion in [35]).

The multigroup reactor model is discussed in the following sections. In §5.2 there is an in depth treatment of the formulation of the cross section library and reactor parameterization. Then §5.3 explains the run-time reactor model that utilizes the cross section library. Following this, §5.4 presents a benchmark of this method to a standard light water reactor. Finally, §5.5 concludes this study with observations on current limitations of the method and presents opportunities for future work.

5.2   Multigroup Cross Section Generation

When seeking to parameterize nuclear power reactors as a function of initial conditions, the set of possible independent parameters quickly becomes large. In addition to geometric design considerations, the fuel characteristics of the reactor must also be accounted for.

In the one-energy-group reactor model (R1G), the initial loading was parameterized based on neutron production rates, neutron destruction rates, and transmutation matrices per nuclide [35]. All of these metrics are functions of fluence. (Under constant flux irradiation, fluence is a surrogate for time.)

A G-energy-group reactor model (RMG) seeks to re-parameterize the one-group formulation in terms of energy. While the multi-group formulation will remain on a per nuclide basis, fluence based metrics are no longer sufficient. Parameterizing based on fluence was successful in R1G because flux spectrum changes with respect to the buildup of new species were ignored, even as changes to the total flux were accounted for to achieve constant power.

149

However, spectral changes based on initial composition are precisely what the RMG seeks to capture.

To calculate the multigroup spectrum requires multigroup microscopic neutron cross-sections. Performing a spectral calculation followed by a group collapse generates burnup dependent group fluxes and cross sections, and thus burnup dependent reaction rates. This is seen in Equation 5.1

$$R = \sigma \cdot \phi \cdot 10^{-24} \tag{5.1}$$

where R [Hz] is the reaction rate, σ [barns] is the one-group cross section, and ϕ [n/cm^2/s] is the energy-integrated flux.

The remainder of this section is delineated into a discussion on notation, how initial reactor conditions are specified, the three methods that were used to compute the cross sections, and the validation technique used.

5.2.1 Notation

In the RMG, nuclides are indexed by i, times are indexed by τ (tau), perturbations are indexed by p, and energy is indexed by g with lower indices representing higher energy groups. Thus the group constants $\sigma_{i\tau g}$ or σ_{ipg} are themselves parameterized by nuclide, time or perturbation (see §5.2.2), and incident neutron energy. For reference, cross section indices may be seen in Table 5.1.

To fully describe a reactor, several neutron reaction types are required. The type also augments the group constant notation by being a comma-

Table 5.1: Cross Section Indices

Index	Symbol
Nuclide	i
Time	τ
Perturbation	p
Incident Energy Group	g
Exiting Energy Group	h
Reaction Channel, Table 5.2	r_x

Table 5.2: Neutron Reaction Types

Tally	Symbol	MT
Total	t	1
Scattering	s	2 + 4
Elastic Scattering	e	2
Inelastic Scattering	i	4 = sum(51, 91)
n^{th}-state Inelastic Scatter	$i\{n\}$	$50 + n$
(n, 2n)	$2n$	16
(n, 3n)	$3n$	17
Fission	f	18 = 19 + 20 + 21 + 38
First-chance Fission	$f19$	19
Second-chance Fission	$f20$	20
Third-chance Fission	$f21$	21
Fourth-chance Fission	$f38$	38
Absorption	a	27 = 18 + sum(102, 107)
Neutron Capture	γ	102
Proton	p	103
Deuterium	d	104
Tritium	^3H	105
Helium-3	^3He	106
Alpha	α	107
Metastable Neutron Capture	$\gamma*$	†
Metastable (n, 2n*)	$2n*$	†

151

separated preposition to the index. For example, the total cross section would be represented by the symbol $\sigma_{t,i\tau g}$. Table 5.2 displays the reactions used in this study, their symbolic abbreviations, and the corresponding MT number coming from ENDF specification [23]. Entries whose MT number is given as a † indicates that the generation of these tallies were performed in a special way (see below). Additionally, the group-to-group scattering cross section is denoted by the symbol $\sigma_{s,i\tau g \to h}$ where g denotes the incident neutron energy (as before) and h gives the exiting neutron energy. Lastly, let E_g [MeV] represent the group upper energy boundaries. Note that for G groups, there will be $G + 1$ boundaries.

5.2.2 Parameterization of Initial Conditions

The multigroup reactor model requires a library of pre-computed group constants which it uses to calculate run-time cross section values for the core. This library must therefore satisfy two conditions. The first is that it contain group constant information for all independent, mutable parameters of interest. The second is that the parameter values must span their corresponding range of interest.

Changes in the initial parameter conditions would then elicit changes in the cross section values. Such differences in the group constants would thus be picked up by the RMG. For example, take the case of neutron self-shielding in a material with a strong resonance absorption peak. As the number density of the absorber increases, the group constant around the peak may plummet

because the flux in the group decreases. In a relatively dilute medium, the group constant and the flux would increase because fewer neutrons (in an absolute sense) are consumed in this regime. That the cross section library allow such effects to be captured is the primary advantage of a multigroup model over the traditional one-group method.

Table 5.3: Char Parameters that Define a Perturbation

Parameter	Symbol	Units
Fuel Density	ρ_{fuel}	g/cm^3
Cladding Density	ρ_{clad}	g/cm^3
Coolant Density	ρ_{cool}	g/cm^3
Fuel Cell Radius	r_{fuel}	cm
Void Cell Radius	r_{void}	cm
Cladding Cell Radius	r_{clad}	cm
Unit Cell Pitch	ℓ	cm
Number of Burn Regions	b_r	
Fuel Specific Power	p_s	MW/kgIHM
Initial Nuclide Mass Fraction	T_{i0}	kg$_i$/kgIHM
Burn Times	s	days

The code which produces the cross section library is known as Char. Char currently has the ability to adjust a reactor template based on many initial parameters. These fall conceptually into three categories: geometric properties, material properties, and time. Table 5.3 lists the parameters that define a *perturbation* in Char.

Every parameter is specified with one or more values. The outer product of all parameter values defines the set of perturbations for which the group constants are calculated. The total number of perturbations, n_p, is therefore

Table 5.4: CHAR Outer Product Perturbations

$\rho_{\textbf{fuel}}$	$\rho_{\textbf{clad}}$	$\rho_{\textbf{cool}}$	$r_{\textbf{fuel}}$	$r_{\textbf{void}}$	$r_{\textbf{clad}}$	ℓ	b_r	p_s	$T_{\textbf{235}\textbf{U0}}$	s
10.165	5.87	0.73	0.41	0.4185	0.475	1.3127	10	0.04	0.03	0
10.165	5.87	0.73	0.41	0.4185	0.475	1.3127	10	0.04	0.03	100
10.165	5.87	0.73	0.41	0.4185	0.475	1.3127	10	0.04	0.03	200
10.165	5.87	0.73	0.41	0.4185	0.475	1.3127	10	0.04	0.03	300
10.165	5.87	0.73	0.41	0.4185	0.475	1.3127	10	0.04	0.03	400
10.165	5.87	0.73	0.41	0.4185	0.475	1.3127	10	0.04	0.05	0
10.165	5.87	0.73	0.41	0.4185	0.475	1.3127	10	0.04	0.05	100
10.165	5.87	0.73	0.41	0.4185	0.475	1.3127	10	0.04	0.05	200
10.165	5.87	0.73	0.41	0.4185	0.475	1.3127	10	0.04	0.05	200
10.165	5.87	0.73	0.41	0.4185	0.475	1.3127	10	0.04	0.05	300
10.165	5.87	0.73	0.41	0.4185	0.475	1.3127	10	0.04	0.05	400
11.235	5.87	0.73	0.41	0.4185	0.475	1.3127	10	0.04	0.03	0
11.235	5.87	0.73	0.41	0.4185	0.475	1.3127	10	0.04	0.03	100
11.235	5.87	0.73	0.41	0.4185	0.475	1.3127	10	0.04	0.03	200
11.235	5.87	0.73	0.41	0.4185	0.475	1.3127	10	0.04	0.03	300
11.235	5.87	0.73	0.41	0.4185	0.475	1.3127	10	0.04	0.03	400
11.235	5.87	0.73	0.41	0.4185	0.475	1.3127	10	0.04	0.05	0
11.235	5.87	0.73	0.41	0.4185	0.475	1.3127	10	0.04	0.05	100
11.235	5.87	0.73	0.41	0.4185	0.475	1.3127	10	0.04	0.05	200
11.235	5.87	0.73	0.41	0.4185	0.475	1.3127	10	0.04	0.05	300
11.235	5.87	0.73	0.41	0.4185	0.475	1.3127	10	0.04	0.05	400

given by the product of the lengths of the parameter arrays. Table 5.4 displays the perturbations when the fuel density has two reference values, the initial ^{235}U mass fraction also takes two values, the group constants are calculated at five burn steps, and all other parameters are single valued. The group constants are calculated for each perturbation case (row) defined in Table 5.4.

While Table 5.4 spans a limited set of initial conditions, this formulation allows for the easy expansion and extension of input parameters and perturbations. Including additional values for any parameter would extend the number of rows in the table. Including other parameters, such as initial ^{236}U concentration, would expand the number of columns in the perturbation table, effectively increasing the dimensionality parameterized. Fuel forms which may contain many initial nuclides in varying concentrations would be parameterized by changing the mass fractions of all actinides initially present in the core.

Table 5.5: Energy Group Boundaries E_g

g	E_g [MeV]	g	E_g [MeV]
1	10	11	2.15E-5
2	1	12	1.29E-5
3	0.1	13	7.74E-6
4	0.01	14	4.64E-6
5	3.16E-3	15	2.78E-6
6	1.00E-3	16	1.67E-6
7	3.16E-4	17	1.00E-6
8	1.00E-4	18	1.00E-7
9	5.99E-5	19	1.00E-8
10	3.59E-5	20	1.00E-9

For the remainder of the this study the perturbations presented in Table 5.4 demonstrate the validity of the multigroup method. Table 5.5 displays the group structure implemented. This group structure is designed to capture the resonance region more finely than the fast and thermal regions.

Figure 5.1: Unit Fuel Pin Cell
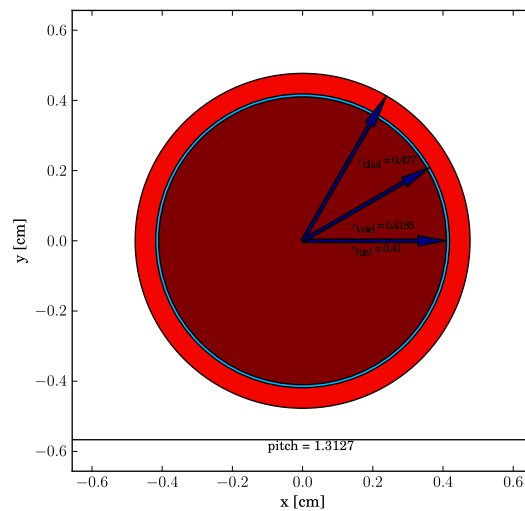
Additionally, though the geometry could be varied, it was fixed for this study. Figures 5.1 & 5.2 show the fuel pin cell as well as the 17x17 lattice that were used to generate the precomputed cross section library (see §5.2.3). Reflecting boundary conditions were applied to the edges of the lattice.

Lastly, default materials are specified. Table 5.6 shows the uranium-oxide fuel mass fractions for initial heavy metal (IHM) with a 4.5% ^{235}U enrichment. Table 5.7 gives the mass fractions for the cladding, where the elemental

Figure 5.2: Fuel Assembly Lattice
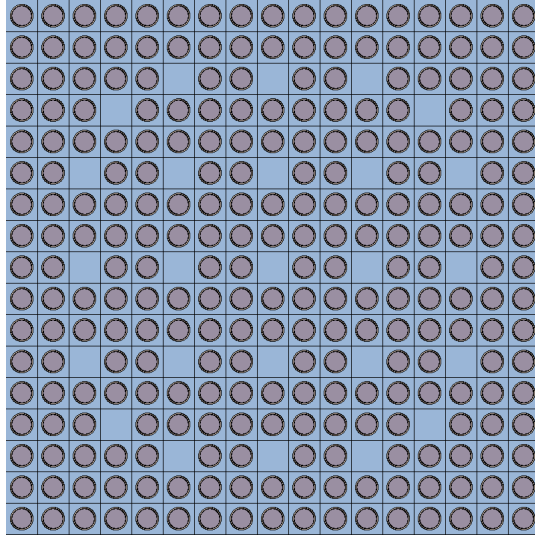
Table 5.6: Mass Fractions in Fuel Region

nuclide	mass fraction
^{16}O	0.11858
^{235}U	0.03966
^{238}U	0.84176

Table 5.7: Mass Fractions in Cladding Region

nuclide	mass fraction
Zr	0.98135
Cr	0.00100
Fe	0.00135
Ni	0.00055
Sn	0.01450
^{16}O	0.11858

Table 5.8: Mass Fractions in Coolant Region

nuclide	mass fraction
^{1}H	0.11107
^{16}O	0.8886
^{10}B	6.0785E-05
^{11}B	0.00026914

entries have their naturally occurring isotopic distribution. Table 5.8 displays the mass weights for borated light water. Note that these mass fractions may be perturbed from the given values.

5.2.3 Cross Section Generation: Serpent

Of the over 3000 nuclides, high-fidelity neutron cross section information is available for only approximately 400 major species. (The ENDF/B-VII incident neutron library was used in the ACE nuclear data format [6].) Moreover, not all reactions are tallied for these nuclides. However, where fundamental cross section data exists for a nuclide and a reaction, it is preferable to use this high-fidelity information to compute group constants over other methods discussed below. For a complete listing of which method was used for each nuclide, and which reaction channels were available, please refer to Appendix C.

G-group cross sections are assembled for each perturbation using the Monte Carlo neutron transport code Serpent [14] where possible. Char fills a templated Serpent input deck with the perturbation values and then executes the transport code. The templates use a combination of detectors in the fuel,

cladding, and coolant regions as well as the universe metrics that Serpent outputs to determine the group constants. Detectors tally volume averaged, energy discretized parameters. To obtain a group constant, the detector for the reaction rate of a nuclide is divided (internally by Serpent) by the detector for the flux spectrum.

In almost every case, the detectors specified with the appropriate MT number suffice. However, some tallies (and some reaction-like parameters) are not given by detectors but are still computable via Serpent.

Foremost among the non-standard calculations is the group-to-group scattering cross section $\sigma_{s,ipg\to h}$. Among the region-based output of Serpent are both a group transfer probability matrix $P_{g\to h}$ as well as the group-to-group scattering cross section. These are subject to the constraints in equations 5.2 & 5.3.

$$\sum_h^G P_{g\to h} = 1 \tag{5.2}$$

$$\sigma_{s,g\to h} = P_{g\to h} \cdot \sigma_{s,g} \tag{5.3}$$

However, the group transfer probability, and thus the group-to-group scattering cross sections are functions of the entire spatial region and not individual species within that region.

The RMG requires that the group-to-group scattering cross sections be provided per nuclide. To this end, the author modified the source code of Serpent to include an optional additional mode where P_{gh} is calculated for only a specific sub-material in a region. Using this mode with a single

nuclide material and the detector-calculated scattering cross section $\sigma_{s,ipg}$, the group-to-group scattering cross section was computed for a single species via equation 5.3.

The next supplemental calculation that Char performs comes more from a deficiency in the ENDF specification than from Serpent. Reactions which leave the final nucleus in an energy state above ground do not receive separate MT numbers. Some of these excited states are metastable and may persist long enough in the core to have a significant interaction probability of their own and/or to have noticeable impacts on the fuel cycle. That metastable nuclides have their own cross section libraries, but can not be formed by neutron interactions present in ground-state nuclide libraries, is a perennial issue.

Here the metastable issue is circumvented by using the 64-group cross section library from Cinder that is included with MCNPX versions 2.6+ [28]. The Cinder cross sections include metastable interactions. Serpent is then used to compute a flux spectrum which matches the group structure of the Cinder data for each perturbation. Collapsing the metastable and ground cross sections to G-groups and dividing the former by the later gives a metastable-to-ground ratio r_{meta}. This ratio may then be used along with the Serpent tally to calculate the group constants desired, as seen in equations 5.4 & 5.5.

$$\sigma_{\gamma,ipg} = \frac{\sigma_{\gamma_{\mathrm{tot}},ipg}}{1 + r_{\mathrm{meta}}} \tag{5.4}$$

$$\sigma_{\gamma*,ipg} = r_{\mathrm{meta}} \cdot \sigma_{\gamma,ipg} \tag{5.5}$$

In equation 5.4, the $\sigma_{\gamma_{\mathrm{tot}},ipg}$ represents the total neutron capture cross section

as provided by the Serpent via MT 102. However, Cinder lists the ground and metastable states separately. Most nuclides do not have a metastable state and thus the ground state interaction is the total (*i.e.* $\sigma_{\gamma,ipg} = \sigma_{\gamma_{tot},ipg}$). The RMG expects the interaction tallies to be split out, as in Cinder. Analogous equations are derivable for the (n, 2n*) interaction.

Furthermore, the average number of neutrons produced per fission event $\bar{\nu}$ is also calculated in a special way via Serpent. The pseudo-tally number -7 yields $\bar{\nu}\sigma_{f,ipg}$. Using the fission group constant calculated from Serpent detectors in the usual way, $\bar{\nu}$ is obtained via equation 5.6.

$$\bar{\nu}_{ipg} = \frac{\bar{\nu}\sigma_{f,ipg}}{\sigma_{f,ipg}} \tag{5.6}$$

The final pseudo-tally that is calculated via serpent is the fission neutron energy spectrum, $\chi(E)$. The cross section data libraries do not contain information on $\chi(E)$. However, Serpent outputs per group values for this parameter for different regions. While this does not capture per nuclide effects, $\chi(E)$ varies only slightly among different species. Moreover, since a Serpent run is performed for each perturbation, changes to the initial conditions are still encapsulated. Thus the induced error on the RMG is very low.

Sample input deck listings that were used to calculate burnups, flux spectra, and group constants may be seen in Appendix A.

5.2.4 Cross Section Generation: Physical Models & Cinder

As mentioned in §5.2.3, high-fidelity cross section data is available for only a small fraction of the nuclides, though arguably the most important ones. However, some species may have significant fuel cycle importance and yet do not have the highest-fidelity data available.

In this case, Char and the RMG 'fall-back' to using a combination of Cinder data and fundamental physical models to estimate the group constants. The first stage in this calculation, as with the metastable-to-ground ratio, is to use Serpent to compute a 64-group flux ϕ_n which matches the structure used in the Cinder library. If Cinder data exists for a nuclide for a reaction, a simple collapse down to G-groups is performed. For other reactions physical models are used. In all cases if Cinder data and physical models are not available, then group constants of zero are assumed. Note that group constants tabulated in this way, while dependent on changes in the spectrum, are independent of effects such as self-shielding. The remainder of this section discusses the reactions individually.

First, Cinder includes cross section information for fission reactions. If n indexes $N = 64$ groups from Cinder and E [MeV] denotes the energy boundaries, the G-group collapsed fission cross section may be computed as in equation 5.11 [42].

$$n_l = \min(n|E_g < E_n) \tag{5.7}$$

$$n_u = \max(n|E_n < E_{g+1}) - 1 \tag{5.8}$$

$$f_l = \frac{E_{n_l} - E_g}{E_{n_l} - E_{n_l-1}} \tag{5.9}$$

$$f_u = \frac{E_{g+1} - E_{n_u}}{E_{n_u+1} - E_{n_u}} \tag{5.10}$$

$$\sigma_{f,ipg} = \frac{f_l \sigma_{f,ipn_l-1} \phi_{n_l-1} + \sum_{n=n_l}^{n_u} \sigma_{f,ipn} \phi_n + f_l \sigma_{f,ipn_u+1} \phi_{n_u+1}}{f_l \phi_{n_l-1} + \sum_{n=n_l}^{n_u} \phi_n + f_u \phi_{n_u+1}} \tag{5.11}$$

Equations 5.7-5.10 define lower and upper indices and linear energy fractions which aid in calculating group constants in which the boundaries only partially overlap.

Cinder does not include $\bar{\nu}$ data and so for nuclides where the fission cross-section is non-zero, a constant value of 2.5 was assumed. More realistically, $\bar{\nu}$ values may be taken from species with a matching number of nucleons (A-number) if data is not available for a nuclide. Cinder also does not include fission neutron spectrum information. Where fission is possible, the physical model seen in equation 5.12 was discretized to G-groups.

$$\chi(E) = 0.453 \cdot e^{-1.036E} \cdot \sinh\left(\sqrt{2.29E}\right) \tag{5.12}$$

This spectrum comes from ^{235}U, but may be used for other nuclides as well [13].

Non-fission absorption reaction cross sections (γ, 2n, 3n, p, d, ^{3}H, ^{3}He, α, $\gamma*$, 2n*) are computed similarly to the fission group constant. If a reaction type is available in Cinder, a group collapse on the 64-group data is performed. If the reaction type is not present for a nuclide, the interaction is assumed to be impossible and zero values are returned.

Considerably more complicated is the physical model of the scattering cross section. Unfortunately, Cinder provides no pretabulated 64-group data

to collapse. Moreover, the group-to-group scattering cross section $\sigma_{s,ipg \to h}$ is desired, adding an additional dimension to compute. Furthermore, because scattering reactions are mainly about energy transfer between the neutron and nuclide, the material temperature T [K] is also important.

Equation 5.13 represents a continuous energy, double differential model of the scattering cross section [21, 47].

$$\frac{d^2}{dE'd\Omega}\sigma_s(E \to E', \Omega \to \Omega') = \frac{b^2}{kT} \cdot \sqrt{\frac{E'}{E}} e^{-\frac{\beta}{2}} S(\alpha, \beta) \qquad (5.13)$$

where b [cm] is the bound scattering length of the target nucleus, E [MeV] is the incident neutron energy, E' [MeV] is exiting neutron energy, Ω [sr] is the incident neutron solid angle, Ω' [sr] is the exiting neutron solid angle, m_n is mass of the neutron, M_A is the mass of the target nucleus, and k [MeV/K] is Boltzmann's constant. $S(\alpha, \beta)$ represents the scattering kernel with the scattering parameters α and β defined in equations 5.14 & 5.15.

$$\alpha = \frac{E' + E - 2\sqrt{E'E}\cos(\theta)}{\frac{M_A}{m_n}kT} \qquad (5.14)$$

$$\beta = \frac{E' - E}{kT} \qquad (5.15)$$

Many approximations to the scattering kernel exist. For a free gas, $S(\alpha, \beta)$ may be set as in 5.16.

$$S(\alpha, \beta) = \frac{1}{\sqrt{4\pi\alpha}} \text{Exp}\left(-\frac{\alpha^2 + \beta^2}{4\alpha}\right) \qquad (5.16)$$

The bound scattering length for a nuclide, which provides a base estimate of the scattering cross section, is computed via coherent and incoherent

164

components as seen in equation 5.17.

$$b = \sqrt{\left|b_{\text{coh}}\right|^2 + \left|b_{\text{inc}}\right|^2} \tag{5.17}$$

Values for the scattering lengths were obtained from [37]. For nuclides that do not appear in this tabulation, a b-value for a nuclide of the same element was used as a surrogate. If the entire element was absent from the tabulation, then the scattering length of the next lowest Z-numbered nuclide was substituted instead.

Because neutron transport is not performed here, the direction of neutron travel is not important to the RMG. Thus the double differential cross section may be integrated over all solid angles.

$$\frac{d\sigma_s(E \rightarrow E')}{dE'} = \frac{\pi b^2 M_A}{2Em_n} \cdot \left[Q^-(\alpha, \beta) - Q^+(\alpha, \beta)\right] \tag{5.18}$$

where

$$Q^{\pm}(\alpha, \beta) = \text{Exp}\left(-\frac{\beta \mp |\beta|}{2}\right) \left[\text{Erf}\left(\frac{|\beta| \pm \alpha_1}{2\sqrt{\alpha_1}}\right) - \text{Erf}\left(\frac{|\beta| \pm \alpha_{-1}}{2\sqrt{\alpha_{-1}}}\right)\right] \tag{5.19}$$

with

$$\alpha_{\pm 1} = \frac{E' + E \mp 2\sqrt{E'E}}{\frac{M_A}{m_n}kT} \tag{5.20}$$

Equation 5.18 treats $d\sigma_s(E \rightarrow E')/dE'$ in the most general way. Significant algebraic simplifications may be made in the cases where $E' = E$, $m_n \approx M_A$, or $m_n \ll M_A$. A proof of the integration from equation 5.13 to equation 5.18 is presented in Appendix B.

Therefore the group-to-group scattering cross section may thus be calculated as in equation 5.21.

$$\sigma_{s,g\to h} = \frac{\int_{E_{g+1}}^{E_g} \int_{E_{h+1}}^{E_h} \frac{d\sigma_s(E\to E')}{dE'}\phi_g(E)dE'dE}{\int_{E_{g+1}}^{E_g} \phi_g(E)dE} \tag{5.21}$$

This equation is most easily solved numerically rather than analytically. A double trapezoidal integration was found to be sufficient for the estimates here. Subjecting the integral in equation 5.21 to the incident scattering constraint yields the appropriate group constant (equation 5.22).

$$\sigma_{s,g} = \sum_{h}^{G} \sigma_{s,g\to h} \tag{5.22}$$

5.2.5 Cross Section Generation: Interpolation

The last class of nuclides are those for which there is no high-fidelity cross section data available. These species are unimportant to the overall NFC material balance. Thus only the roughest of estimates of their cross sections are needed. Moreover, such estimation may be done at RMG run-time rather than during library generation.

The Korea Atomic Energy Research Institute (KAERI) provides simple cross section information for almost 3000 nuclides at a variety of energies [12]. Specifically, data for thermal (2.53E-08 [MeV]) and fission spectrum average (taken as 1.0 [MeV]) were used as representative thermal and fast cross sections. Ignoring all other effects (particularly epithermal resonances which may have a large impact), group constants were computed by linearly interpolating

166

these two cross sections. Call $\sigma^t_{r_x}$ and $\sigma^f_{r_x}$ the thermal and fast cross sections respectively. The group constants for a reaction r_x were estimated using equation 5.23.

$$\sigma_{r_x,g} = \frac{\sigma^f_{r_x} - \sigma^t_{r_x}}{1 - 2.53\text{E-}08} \cdot (E_g - 2.53\text{E-}08) + \sigma^t_{r_x} \tag{5.23}$$

Alternatively, a simple two energy region method which accounts for the 'one-over-v' dependence could be implemented. Consider that for low energies, the cross section is roughly proportional to the inverse of the neutron velocity v [m/s]. The velocity itself is a simple function of the neutron kinetic energy $v = \sqrt{2E/m_n}$. Thus for low energies, the group constant may be estimated via equation 5.24.

$$\sigma_{r_x,g} = \sqrt{\frac{2.53\text{E-}08}{E_g}} \cdot \sigma^t_{r_x} \text{ , where } E_g < 2.53\text{E-}08 \left(\frac{\sigma^t_{r_x}}{\sigma^f_{r_x}} \right)^2 \tag{5.24}$$

However for energies greater than the thermal-fast intersection point, the cross section may simply be taken as the fast value.

$$\sigma_{r_x,g} = \sigma^f_{r_x} \text{ , where } 2.53\text{E-}08 \left(\frac{\sigma^t_{r_x}}{\sigma^f_{r_x}} \right)^2 \leq E_g \tag{5.25}$$

5.2.6 Cross Section Validation

Due to the quantity of cross section data produced through the three above methods, an automatic validation procedure known as *unit testing* was employed. Here, the units are interpreted as the group constants. A suite of tests executed against these units ensures that the cross sections remain physically valid individually as well as in relation to each other. What follows

are the definitions of the physical tests which make up the suite. All cross sections present in the library were tested in this manner.

The most basic test is to verify that all group constants are real and non-negative valued (infinite and not-a-number values are not allowed).

$$0 \leq \sigma_{r_x,ipg} < \infty \tag{5.26}$$

No less important are the constraints that all group constants are less than or equal to the total cross section and that the sum of all non-total reactions is less than or equal to the total.

$$\sigma_{r_x,ipg} \leq \sigma_{t,ipg} \tag{5.27}$$

$$\sum_{r_x \neq t} \sigma_{r_x,ipg} \leq \sigma_{t,ipg} \tag{5.28}$$

Moreover, if a nuclide is fissionable, the following conditions apply.

$$1 \leq \bar{\nu}_{ipg} \leq 5.5 \tag{5.29}$$

$$\sum_{g}^{G} \chi_{ipg} = 1 \tag{5.30}$$

If the nuclide is not fissionable, the following conditions are used instead.

$$\sigma_{f,ipg} = \bar{\nu}_{ipg} = \chi_{ipg} = 0 \tag{5.31}$$

The relation between scattering group constants is defined as follows, to within machine precision.

$$\sigma_{s,ipg} = \sum_{h}^{G} \sigma_{s,ipg \to h} \tag{5.32}$$

Lastly, it is required that the constituent absorption tallies sum to less than or equal to the absorption cross section.

$$\sum_{r_x} \sigma_{r_x,ipg} \leq \sigma_{a,ipg} \tag{5.33}$$

Further conditions could be added to the suite, such as ensuring that the sum of all non-total group constants is less than or equal to $\sigma_{t,ipg}$. However, such summation tests are typically indicative of a more primitive error in the group constants. For a more in depth treatment on missing reaction channel errors, please refer to the benchmark in §5.4.

Thus basic errors are sufficiently captured by the tests above, without adding extraneous noise to the failure analysis. The simple test suite developed here has proven invaluable towards the RMG benchmarking efforts.

5.3 Multigroup Reactor Model

The multigroup reactor model uses the group constant library developed in the previous section to compute criticality and burnup metrics for a nuclear power reactor. The RMG is specified by several parameters, including all those present in Table 5.3.

The advantage of the RMG method is that the values of the reactor parameters need not exactly match any of the perturbations (Table 5.4) in the cross section library. Other methods are often invalidated when the conditions under which the group constants were computed are altered. However, by

including a robust set of values in the perturbation table, the RMG execution remains meaningful.

A flow sheet for the RMG methodology is presented in Figure 5.3. As is seen, the reactor model contains three main calculation stages for each burn time step. First there is a nearest neighbor & interpolation calculation for determining the group constants for this time step. Following this is flux-criticality calculation. Lastly, the reactor has a burnup-transmutation computation before continuing to the next time step. The algorithms implemented are discussed in §5.3.1-5.3.3.

5.3.1 Nearest Neighbor Cross Section Calculation

The process of converting from the perturbation-based cross section library $\sigma_{r_x,ipg}$ to group constants as a function of burn time in the RMG $\sigma_{r_x,i\tau g}$ involves a nearest neighbor calculation as well as a multi-dimensional linear interpolation.

Call a a perturbable reactor parameter, such as fuel density or burn time (*i.e.* the entries in Table 5.3). With p as the perturbation index such that $1 \leq p \leq n_p$ (*i.e.* the row number of Table 5.4), then a_p is the value of this parameter for this perturbation in the cross section library. Furthermore, denote a_r the value of this parameter on the RMG at run time.

In order to perform the correct interpolation, the two perturbations that are closest to the current state of the reactor, a_1^* & a_2^*, must be found. Here the a_p^* notation indicates that the indices have been sorted in order of

Figure 5.3: Multigroup Reactor Model Flow Diagram

Known: from library,
- $\sigma_{r_x,ipg}$
- $\bar{\nu}_{ipg}$
- $\sigma_{s,ipgh}$
- χ_{ipg}

Given:
a_r
$\tau = 0$

Interpolate: Find p_1^* & p_2^*, the two nearest two perturbations, and interpolate between them.
$\sigma_{r_x,i\tau g} = (\sigma_{r_x,ip_2^*g} - \sigma_{r_x,ip_1^*g})x_f + \sigma_{r_x,ip_1^*g}$

Store:
k_τ
$\phi_{\tau g}$

Calculate Criticality:
$\left(A_{\tau g \to h} - \frac{1}{k}F_{\tau g \to h}\right)\phi_{\tau g} = 0$

Set: Time & Fluence
$\Delta s = s_{\tau+1} - s_\tau$
$\Phi_{\tau+1} = \Phi_\tau + \Delta s \sum_{g=1}^{G} \phi_{\tau g}$

Store:
$T_{i\tau+1}$
BU_τ

More steps?
$\tau \to \tau + 1$

yes

no

Transmute:
$T_{i\tau+1} = e^{M_{\tau ij}\Delta s}T_{i\tau}$
Calculate: BU_τ

Continue with batch averaging methodology (R1G).
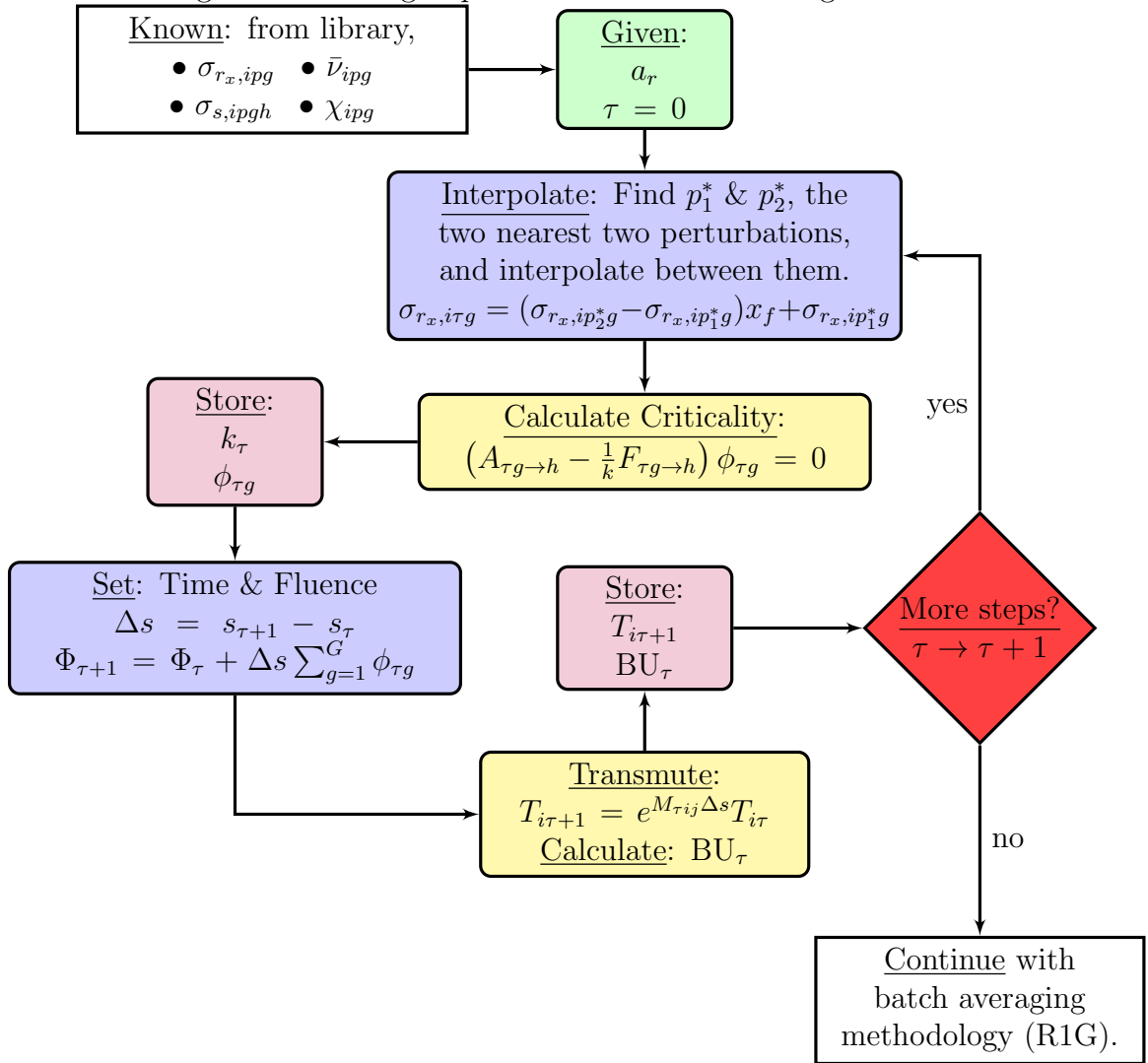
increasing distance.

However, the space that the parameters exist in is at least 10-dimensional, as defined by Table 5.3. Moreover, the scale for these parameters may vary greatly from one a to the next. Therefore, a realistic nearness metric must normalize the values for these parameters individually before calculating a global distance. Equation 5.34 calculates d_p, the distance of the pth perturbation from the state of the reactor.

$$d_p = \sqrt{\sum_a \left(\frac{a_r - a_p}{a_{n_p}} \right)^2} \tag{5.34}$$

Computing the distance d_p for all perturbations to the state of the reactor, the sorted parameters p^* and a_p^* are defined via the sequence $p^* = \{p | d_p \leq d_{p+1}\}$.

Since a_1^* and a_2^* represent the value of a parameter at the two closest perturbations to the current state of the reactor, a unitless multidimensional linear interpolation factor x_f may be defined.

$$x_f = \sum_a \left(\frac{a_r - a_1^*}{a_2^* - a_1^*} \right) \tag{5.35}$$

This x_f value is set for the reactor as a whole then used to generate group constants for all reactions from p_1^* & p_2^* perturbation information available in the cross section library.

$$\sigma_{r_x, i\tau g} = \left(\sigma_{r_x, ip_2^* g} - \sigma_{r_x, ip_1^* g} \right) \cdot x_f + \sigma_{r_x, ip_1^* g} \tag{5.36}$$

Note, that x_f is invalidated whenever the state of the reactor changes. Since burnup time is one of the parameters, x_f must be recalculated every time step but is otherwise constant for all nuclides for all reactions.

5.3.2 Criticality Calculation

Now that group constants have been built for the reactor specified, the next phase of the reactor calculation is to estimate the neutron flux spectrum and the multiplication factor.

The flux spectrum is computed through an iterative matrix method. Call $N_{q,i\tau}$ [atoms/cm^3] the number density for the ith nuclide at time τ in the qth region (fuel, cladding, coolant). The macroscopic cross section of a region is therefore given by equation 5.37.

$$\Sigma_{r_x,q,\tau g} = \sum_i^I N_{q,i\tau} \cdot \sigma_{r_x,i\tau g} \tag{5.37}$$

Since the fuel and coolant are the only two regions with significant neutronic characteristics, homogenized full-core cross sections are given by the reduction in equation 5.38

$$\Sigma_{r_x,\tau g} = \frac{V_{\text{fuel}}\Sigma_{r_x,\text{fuel},\tau g} + \zeta_{\tau g}V_{\text{cool}}\Sigma_{r_x,\text{cool},\tau g}}{V_{\text{fuel}} + \zeta_{\tau g}V_{\text{cool}}} \tag{5.38}$$

Here, ζ_{tg} is the disadvantage factor per group. This is defined as the average flux in the coolant divided by the average flux in the fuel. It is computed via the macroscopic cross sections and the lattice functions found in [13].

The absorption or A-matrix is defined as

$$A_{\tau g \to h} = I_G \times \Sigma_{t,tg} - \Sigma_{s,\tau g \to h} \tag{5.39}$$

where I_G is the $G \times G$ identity matrix. The fission source or F-matrix is defined by

$$F_{\tau g \to h} = \chi_{\text{fuel},\tau g} \times \bar{\nu}\Sigma_{f,\text{fuel},\tau g} \tag{5.40}$$

173

The multigroup flux spectrum is then calculated via the linear relation in equation 5.41.

$$A_{\tau g \to h} \cdot \phi_{\tau g} = \frac{1}{k} F_{\tau g \to h} \cdot \phi_{\tau g} \qquad (5.41)$$

To solve this equation in an efficient iterative fashion, note that the expression $\frac{1}{k} A^{-1} F$ is a matrix with constant coefficients. Using the superscript m to indicate the loop index, equations 5.42 & 5.43 may be successively applied until convergence.

$$\phi_{\tau g}^{m+1} = \frac{1}{k^m} A_{\tau g \to h}^{-1} F_{\tau g \to h} \cdot \phi_{\tau g}^{m+1} \qquad (5.42)$$

$$k^{m+1} = k^m \frac{\sum_g^G \bar{\nu} \Sigma_{f,\text{fuel},\tau g} \phi_{\tau g}^{m+1}}{\sum_g^G \bar{\nu} \Sigma_{f,\text{fuel},\tau g} \phi_{\tau g}^m} \qquad (5.43)$$

The convergence criteria are defined by equations 5.44 and 5.45 or when $m = 100$.

$$\left| \frac{\phi_{\tau g}^{m+1} - \phi_{\tau g}^m}{\phi_{\tau g}^{m+1}} \right| = \epsilon \qquad (5.44)$$

$$\left| \frac{k_\tau^{m+1} - k_\tau^m}{k_\tau^{m+1}} \right| = \epsilon \qquad (5.45)$$

For this study a value of $\epsilon = 0.005$ was taken and convergence was typically reached within two or three iterations.

The iterative algorithm described by equations 5.42 & 5.43 is sufficient for finding the shape of the neutron flux spectrum. However, k^m and $\phi_{\tau g}^m$ are more properly interpreted as unnormalized eigenvalues and eigenvectors of the linear equation in 5.41. Normalization is, therefore, required to discern the 'true' values of k_τ and $\phi_{\tau g}$.

174

In general, there are two methods with which to normalize the total flux: by assuming constant flux or constant power. The total flux here was determined by matching the specific power p_s [MW/kg] input to the model. Denote the one-group macroscopic fission cross section as $\Sigma_{f,\text{fuel},\tau}$ [cm^{-1}].

$$\Sigma_{f,\text{fuel},\tau} = \frac{\sum_g^G \Sigma_{f,\text{fuel},\tau g} \phi_{\tau g}^m}{\sum_g^G \phi_{\tau g}^m} \tag{5.46}$$

The total flux for time τ is thus given by equation 5.47.

$$\phi_\tau = p_s \cdot \rho_{\text{fuel}} \cdot \frac{1}{3.284\text{E-}14 \cdot \Sigma_{f,\text{fuel},\tau}} \tag{5.47}$$

Here the value of 3.284E-14 [kJ/n] is a conversion factor assuming an average energy release of 205 [MeV/fission]. This value may used to rescale the spectrum as seen in equation 5.48

$$\phi_{\tau g} = \phi_\tau \cdot \frac{\phi_{\tau g}^m}{\sum_g^G \phi_{\tau g}^m} \tag{5.48}$$

The multiplication factor of the RMG is handled by another side calculation which uses the rescaled flux spectrum. Here, k_t is computed strictly as a function of the material and neutronic properties of the core.

$$k_\tau = P_{\text{NL}} \cdot \frac{\sum_g^G V_{\text{fuel}} \cdot \bar{\nu}\Sigma_{f,\text{fuel},\tau g} \cdot \phi_{\tau g}}{\sum_g^G \left(V_{\text{fuel}} \cdot \Sigma_{a,\text{fuel},\tau g} + \zeta_{\tau g} \cdot V_{\text{cool}} \cdot \Sigma_{a,\text{cool},\tau g} \right) \cdot \phi_{\tau g}} \tag{5.49}$$

In equation 5.49, P_{NL} represents the non-leakage probability and must be externally supplied to the reactor model. Note that P_{NL} is functionally an adjustment parameter which is used to account for fundamental modeling errors in the geometry. The non-leakage probability accounts for the fact that

175

the reactor is modeled as an infinitely reflected system. Thus, the RMG may be 'tuned' by varying P_{NL}. Reasonable limits on which to adjust the non-leakage probability vary by reactor type.

5.3.3 Transmutation Calculation

The last portion of the coupled multigroup reactor calculation is the transmutation calculation. This step takes the fuel vector at time τ and burns it to obtain the fuel vector at time $\tau + 1$.

ORIGEN 2.2 [7] was used to calculate the nuclide vector $T_{i\tau+1}$. ORIGEN has the capability to take an input vector $T_{i\tau}$ and one-group cross sections and perform the transmutation calculation above. The one-group cross sections that ORIGEN requires are for constituent absorption reactions. Namely, these are $r_x = \gamma, 2n, 3n, f, \alpha, p, \gamma^*, 2n^*$. Such cross sections may be found via a simple group collapse as seen in equation 5.50.

$$\sigma_{r_x,i\tau} = \frac{1}{\phi_\tau} \sum_g^G \sigma_{r_x,i\tau g} \phi_{\tau g} \tag{5.50}$$

Filling an ORIGEN cross section template with the $\sigma_{r_x,i\tau}$ for all available nuclides provides the transmutation code a customized library for the RMG at time τ. Executing ORIGEN with this library, for an input vector $T_{i\tau}$, with a constant power irradiation at p_s for Δs days provides the output nuclide concentration vector.

Therefore the time evolution of the flux spectrum and the neutronic characteristics of the fuel are accounted for by the RMG burnup model. This

final transmutation step effectively increments the reactor calculation to the next time step. If more time steps were specified, the RMG calculation returns to the nearest-neighbor cross section interpolation calculation. Otherwise, the RMG calculation is complete.

5.4   Benchmark

The RMG was validated against a Serpent model of the same standard light-water reactor core. The state of the reactor for the both RMG and Serpent was taken at an off-perturbation point in order to test the nearest-neighbor interpolation in addition to the criticality and burnup calculations. The reactor state is for this benchmark is shown in Table 5.9. The burnup

Table 5.9: Benchmark Reactor State

Parameter	Symbol	Value
Fuel Density	ρ_{fuel}	10.7 g/cm^3
Cladding Density	ρ_{clad}	5.87 g/cm^3
Coolant Density	ρ_{cool}	0.73 g/cm^3
Fuel Cell Radius	r_{fuel}	0.41 cm
Void Cell Radius	r_{void}	0.4185 cm
Cladding Cell Radius	r_{clad}	0.475 cm
Unit Cell Pitch	ℓ	1.3127 cm
Number of Burn Regions	b_r	10
Fuel Specific Power	p_s	0.04 MW/kgIHM
Initial ^{235}U Mass Fraction	$T_{^{235}\text{U}_0}$	0.045 kg$_{\text{i}}$/kgIHM
Initial ^{238}U Mass Fraction	$T_{^{238}\text{U}_0}$	0.955 kg$_{\text{i}}$/kgIHM

times that were computed for the reactor ranged from 0 to 365 days with a step size of 40.556 days. The initial heavy metal concentrations, which were

177

used for benchmarking purposes only, may also be seen in Table 5.9.

The nearest neighbor vector p^* for all time steps, in terms of indices of the perturbation Table 5.4, is given in Table 5.10. The reason this matrix is expected is because the computation is closest to zero time at the start of the burn and gradually migrates closer to 400 days by the end. Moreover the initial ^{235}U vector falls in between two of the perturbation cases, but 4.5% lies clearly closer to the 5% perturbations than the 3% cases. Lastly, the fuel region density lies exactly between two of the perturbation steps. Thus, the perturbations with the minimal distance to the configuration will flank the fuel enrichment (staying closer to 5% ^{235}U) and remain equidistant from the two perturbation fuel densities while otherwise moving through the core in time. Note that, because of the linear interpolation of the group constants, only the two leftmost p^* columns in Table 5.10 (representing p_1^* and p_2^*) influence the RMG calculation. The remaining columns are shown for demonstrative purposes only. Microscopic cross sections calculated via an interpolation between the two nearest neighbor points p_1^* & p_2^* may be collapsed to obtain one-group values $\sigma_{r_x,i\tau}$. These one-group values are presented below as part of the benchmark.

Next, the criticality calculation is compared for the Serpent case and the RMG. This consists of contrasting the multiplication factor and the flux spectrum at different burn times. In all further benchmarks, the errors in the two-point comparison are defined by a fractional deviation. Call a_r a parameter computed via the RMG and a_s the same parameter from the Serpent model.

Table 5.10: Nearest Neighbors over Burn for Interpolating Cross Sections

days	p^*																			
0	16	6	17	7	18	8	11	1	9	19	12	2	13	3	10	20	4	14	5	15
40.6	16	6	17	7	18	8	19	9	11	1	12	2	13	3	10	20	14	4	5	15
81.1	17	7	16	6	18	8	19	9	2	12	11	1	13	3	10	20	14	4	15	5
122	7	17	18	8	6	16	19	9	20	10	2	12	3	13	11	1	14	4	15	5
162	8	18	7	17	19	9	6	16	20	10	3	13	2	12	4	14	11	1	15	5
203	18	8	19	9	17	7	10	20	6	16	3	13	4	14	12	2	5	15	11	1
243	18	8	19	9	17	7	10	20	6	16	3	13	4	14	12	2	5	15	11	1
284	19	9	18	8	10	20	7	17	4	14	6	16	3	13	5	15	2	12	11	1
324	19	9	10	20	8	18	7	17	4	14	5	15	3	13	6	16	2	12	11	1
365	10	20	19	9	18	8	7	17	5	15	4	14	3	13	6	16	12	2	11	1

Equation 5.51 is the fractional deviation ε such that values which the RMG over-predicts will be positive and under-predictions will be negative.

$$\varepsilon = \frac{a_r}{a_s} - 1 \tag{5.51}$$

Figure 5.4 displays the comparison for the multiplication factor k. Note that

Figure 5.4: Multiplication Factor Benchmark
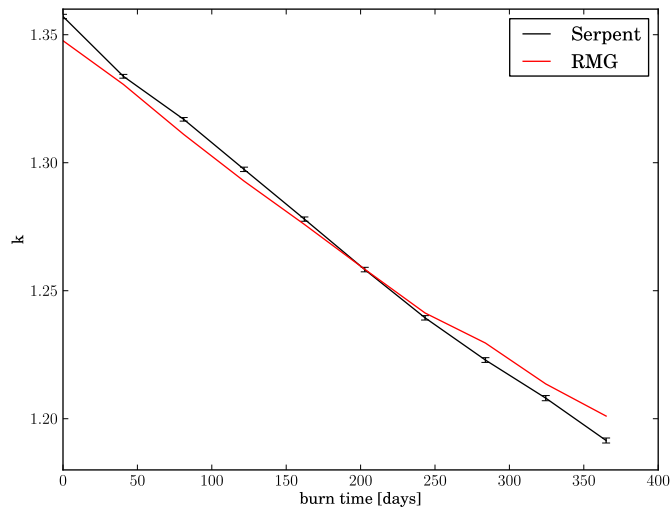
the fractional deviations on the RMG curve in Figure 5.4 take on a value of

179

less than 1% at every burnup step. The error bars on the Serpent curve are the stochastic modeling errors inherent in any Monte Carlo calculation and do not represent inaccuracies in the cross sections. Additionally, these two curves both exhibit the linear trend expected but are seen to have slightly different slopes due to errors in the cross sections and discrepancies in which nuclides are included in the burnup-criticality calculation.

Additionally the flux spectrum at the beginning-of-life (BOL) (0 days) and end-of-life (EOL) (365 days) may be seen in Figures 5.5 & 5.6. By

Figure 5.5: BOL Neutron Flux Spectrum Benchmark
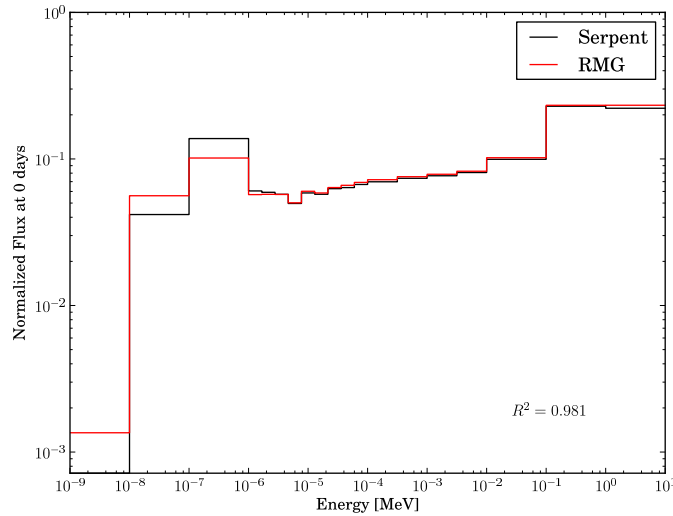
inspection, there is good agreement between the RMG and Serpent spectra. Quantitatively, the fractional deviation lies between 0.5 - 5% for most groups. The groups for which significantly larger ε are present (10 - 85%) are the

Figure 5.6: EOL Neutron Flux Spectrum Benchmark
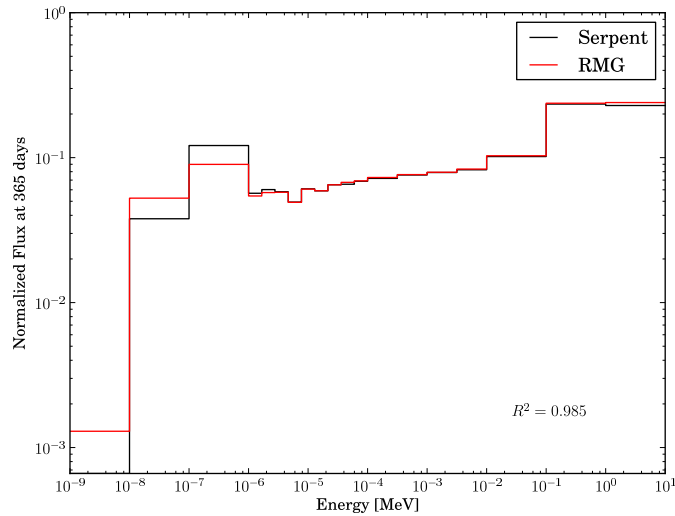
low energy groups where the flux may be smaller by orders of magnitudes. The coefficients of determination (R^2) for both figures are greater than 0.98, indicating a strong correlation between Serpent and RMG spectra. Differences in Figures 5.5 & 5.6 are partially explained by the difference in regions for which the flux is defined. The RMG curves here represent a homogenized full-core, while the Serpent spectra are only for the fuel region. Given the higher probability of thermal scattering events in the coolant and a greater likelihood of absorption reactions in the fuel, the harder Serpent fuel spectrum is expected.

As previously discussed, the RMG modifies the above spectra by a disadvantage factor when computing reaction rates to account for spectral

differences between the fuel and coolant regions. Recall that $\zeta_{\tau g}$ is defined as the flux in the coolant divided by the flux in the fuel. Figure 5.7 shows $\zeta_{\tau g}$ as a function of group for both BOL & EOL. Because the absorption cross section of the fuel is larger than that of the coolant, $\zeta_{\tau g}$ will always be greater than unity. Moreover, the disadvantage factor generally increases with decreasing energy due to the 'one-over-v' dependence on the cross sections.

Figure 5.7: Disadvantage Factor $\zeta_{\tau g}$ at BOL & EOL
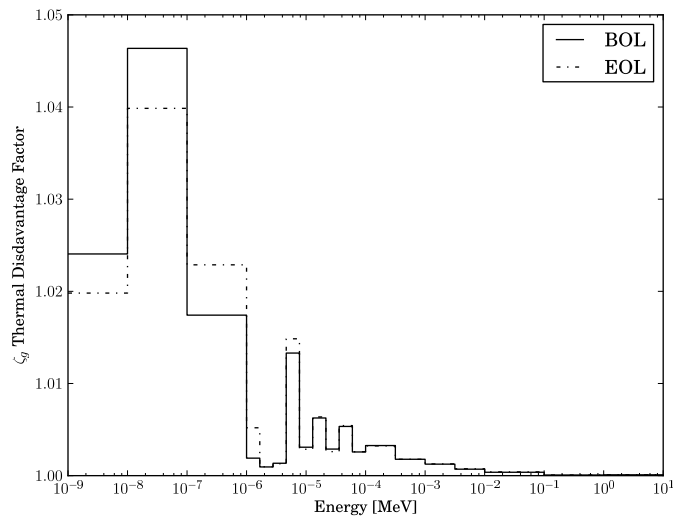
Lastly, the transmutation calculation is benchmarked. Figures 5.8-5.11 display the time evolution of the mass fractions of various important nuclides. This set includes the major actinides as well a various fission products that are tracked in the VISION suite. Serpent does not report errors associated with the mass fraction so no error bars are shown.

182

Figure 5.8: Actinide Mass Fraction Benchmarks

183
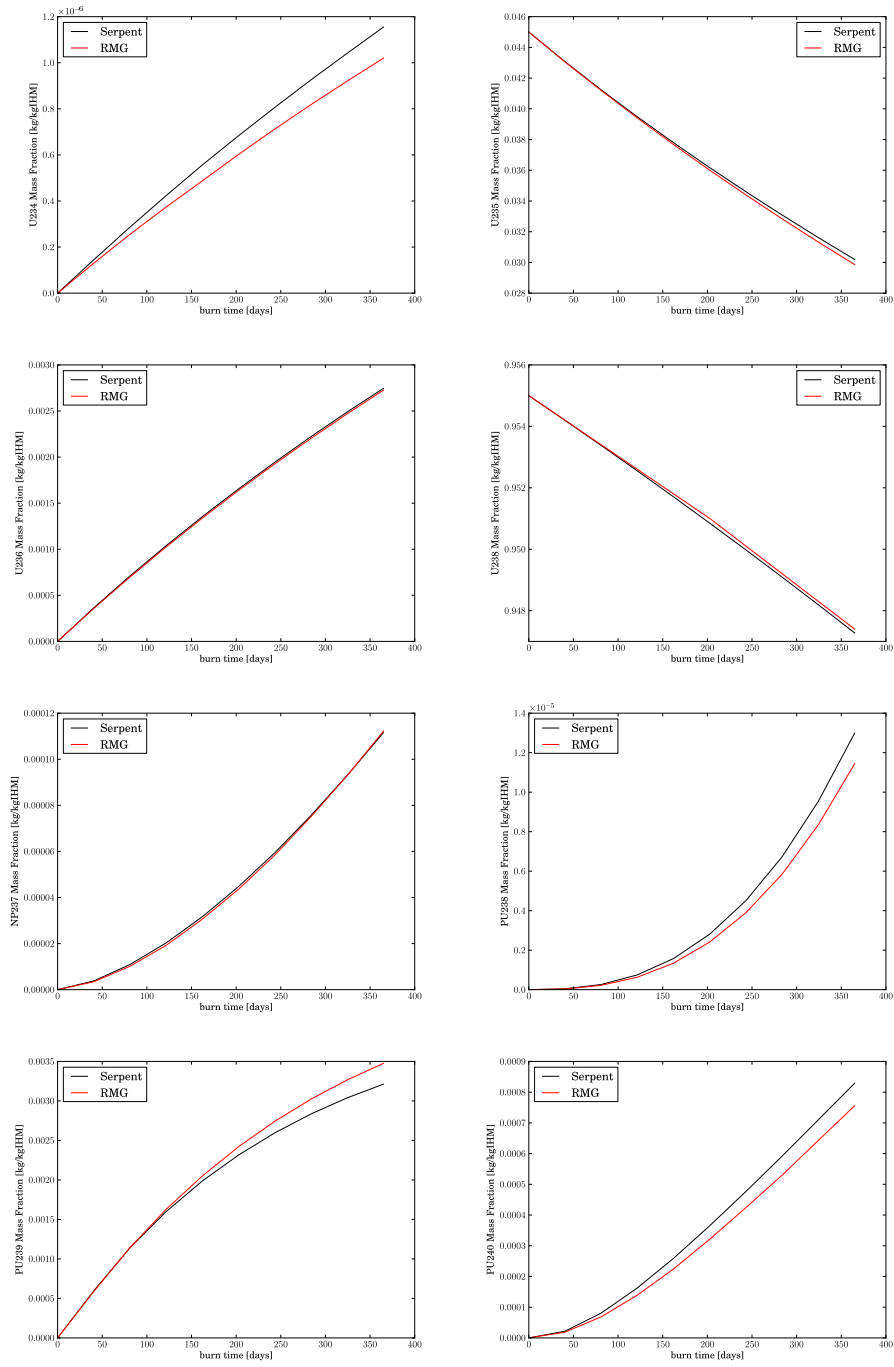
Figure 5.9: Additional Actinide Mass Fraction Benchmarks
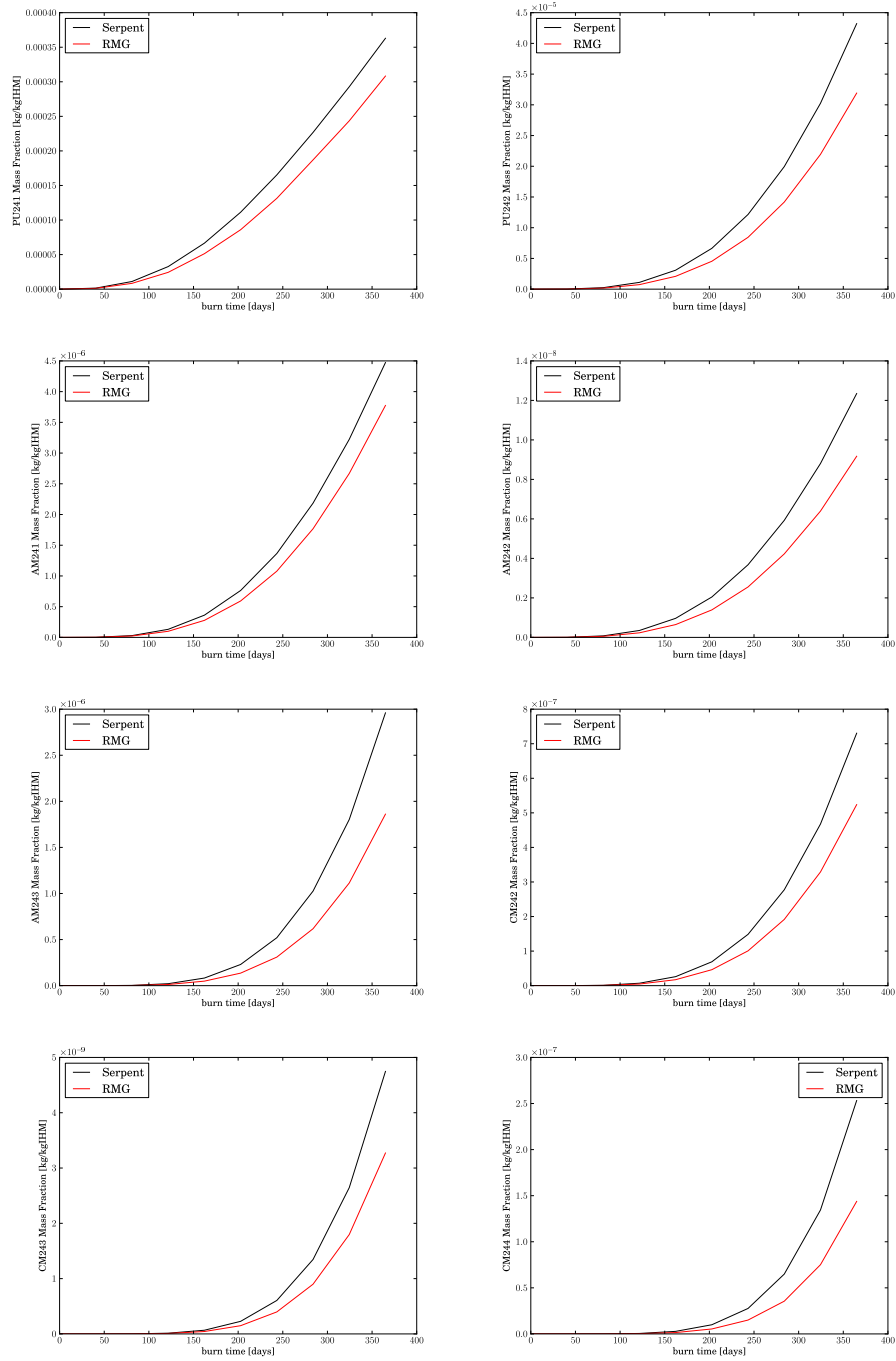
Figure 5.10: Actinide & Fission Product Mass Fraction Benchmarks
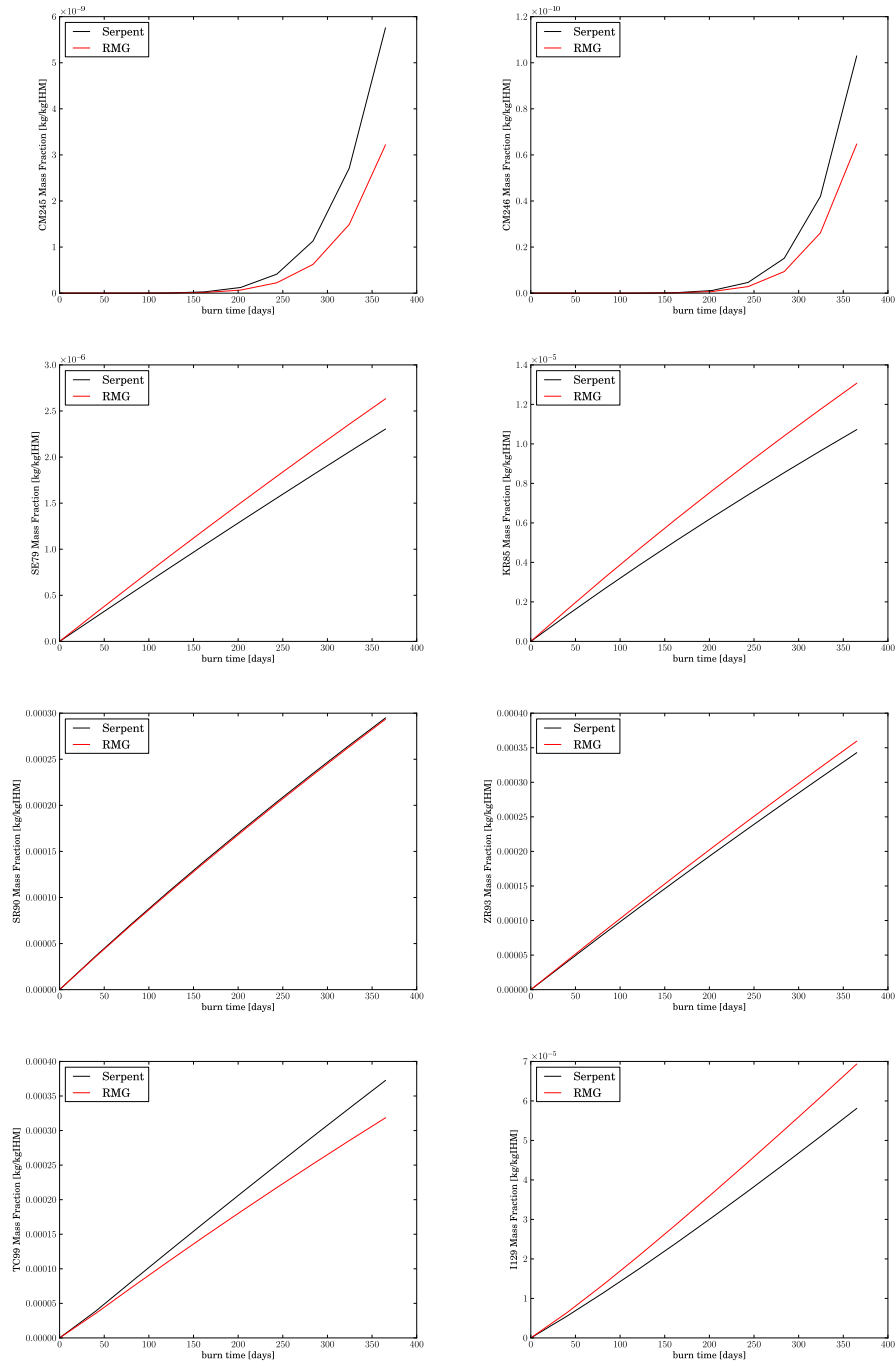
Figure 5.11: Fission Product Mass Fraction Benchmarks
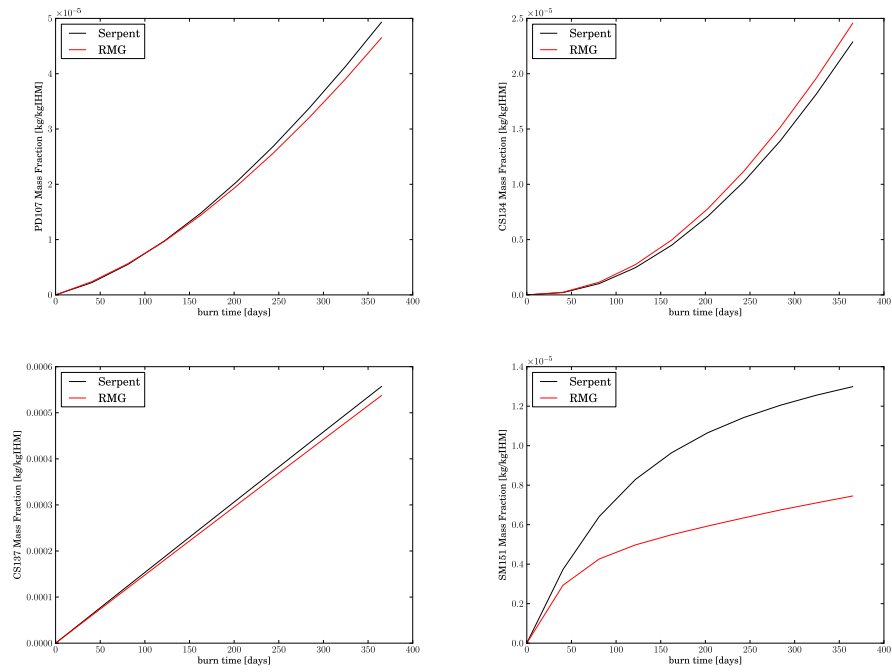
As is seen in these figures, there is good agreement between the transmutation vectors computed by Serpent and those computed by the RMG via ORIGEN. The instances with non-trivial disagreements are largely in the higher order actinides. These nuclides exist in such small amounts, that the relatively high errors do not adversely effect the neutronic performance of the fuel. Moreover, the errors in the mass concentrations are largely a function of the error in the lowest energy groups of the flux.

However, the true strength of the RMG methodology is that it takes into account the time evolution of the cross sections as well. Prior essential physics reactor methods assumed static fluxes as well as cross sections [35]. For the same set of nuclides above, Figures 5.12-5.15 display total, absorption, scattering and fission one-group cross sections as a function of burn time. One-group cross sections are used here in favor of the multigroup cross sections because they capture the total differences between data sets while removing the complexity of plotting three dimensional information.

Moreover, since the one-group cross sections are submitted to ORIGEN to make a transmutation library, it is important to ensure that no reaction is far off from a benchmark value. Tables 5.11-5.15 display the nuclides with the highest $|\varepsilon|$ (in descending order) at any time step for absorption and scattering reactions for the fission products and for absorption, scattering and fission reactions for the actinides. These tables have been filtered to remove species that have short half lives (< 1 day). A superior filter may be to remove nuclides for which no Serpent or Cinder data exists, since these species are presumably

187

Figure 5.12: Actinide One-Group Cross-Section Benchmarks
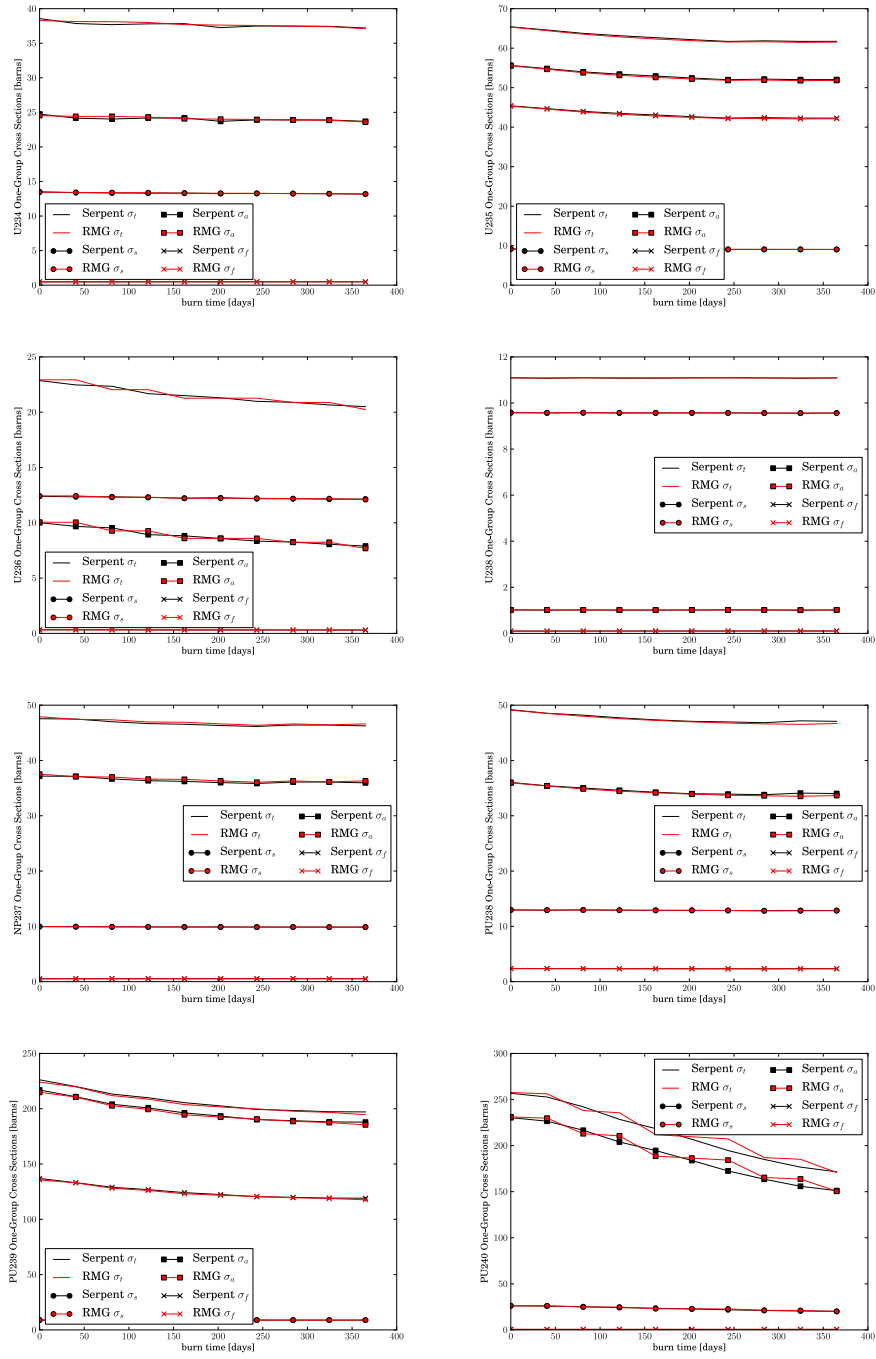
Figure 5.13: Additional Actinide One-Group Cross-Section Benchmarks

189
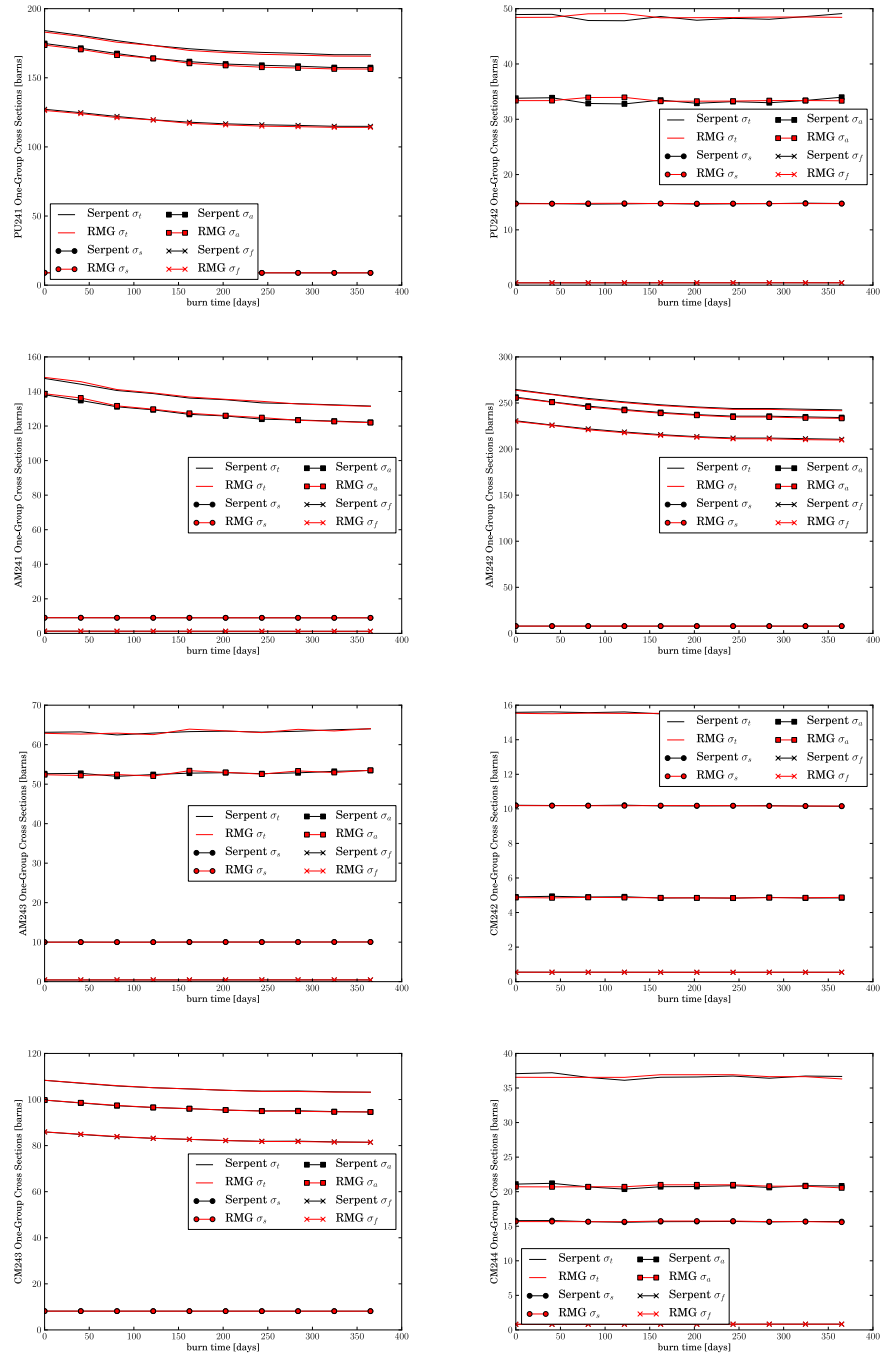
Figure 5.14: Actinide & Fission Product One-Group Cross-Section Benchmarks
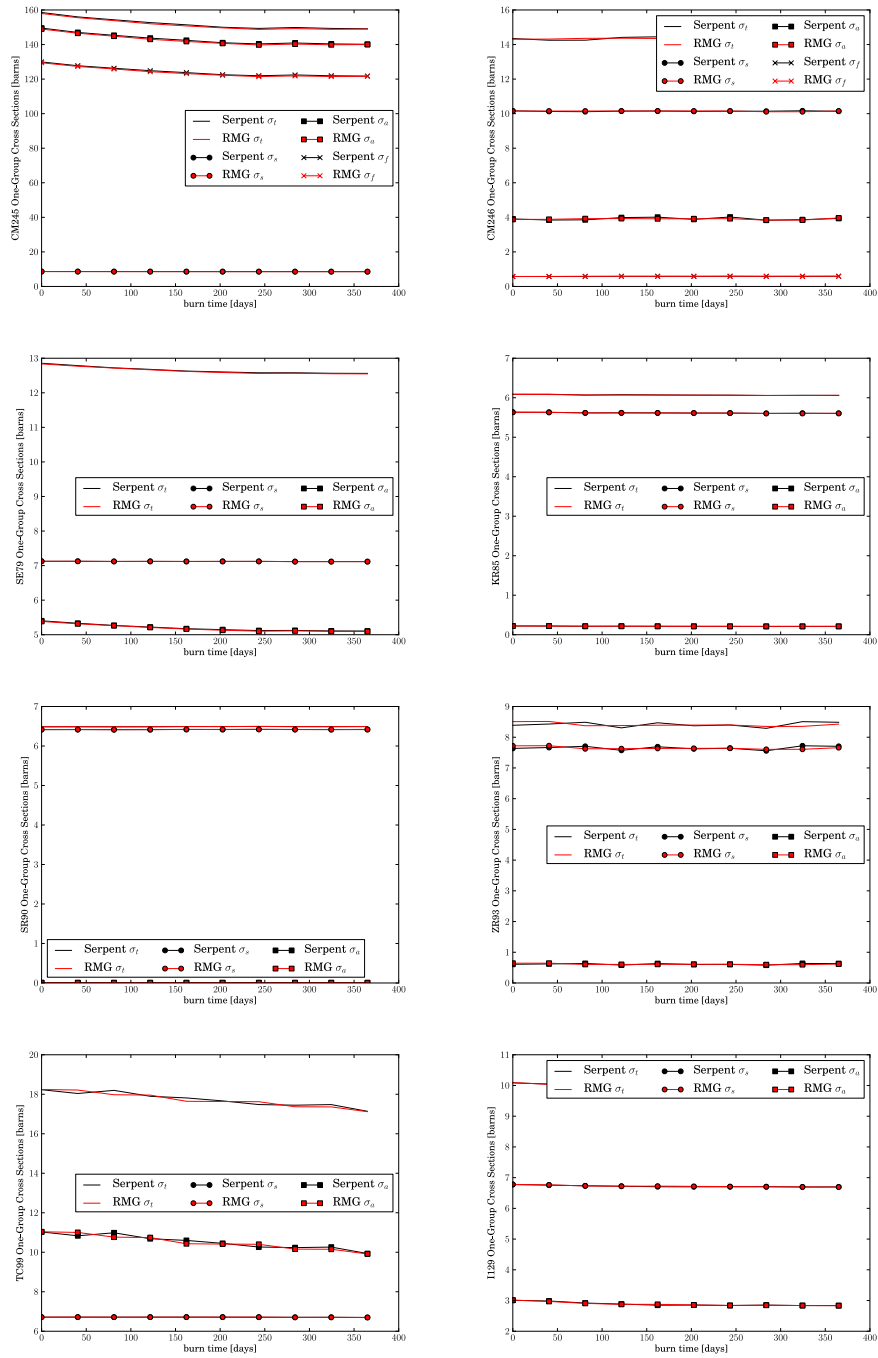
Figure 5.15: Fission Product One-Group Cross-Section Benchmarks

191
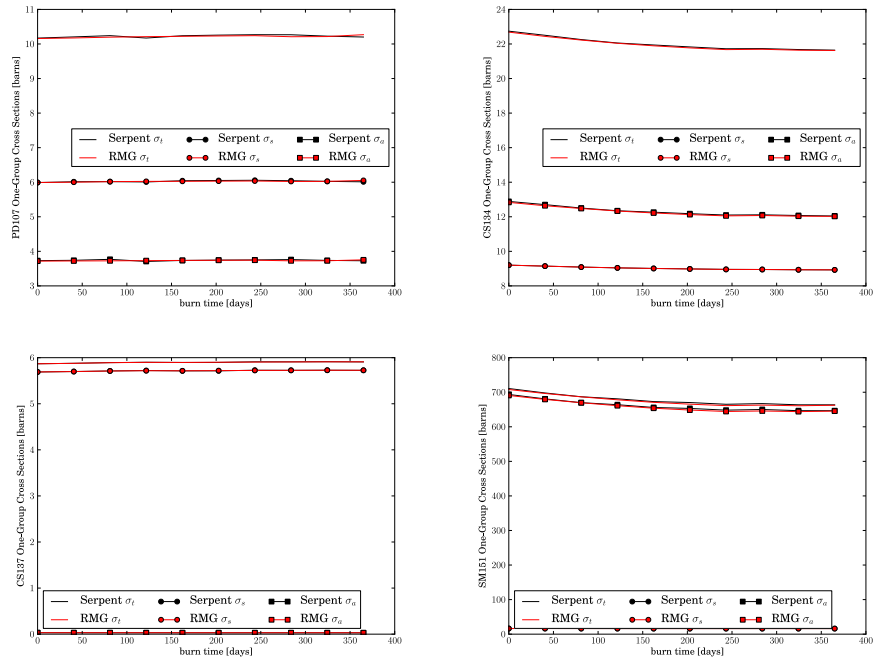
unimportant to the system as a whole. As Tables 5.11-5.15 display, the RMG predicts one-group collapsed cross sections (and thus reaction rates) nearly universally to within 10% of the Serpent values.

Table 5.11: Maximum Actinide σ_s Relative Error

Nuclide	ε
^{240}Pu	+0.0410
^{244}Cm	-0.0096
^{242}Pu	+0.0094
^{236}U	+0.0072
^{246}Cm	-0.0055
^{238}Pu	-0.0051
^{234}U	-0.0048
^{242}Cm	-0.0036
^{239}Pu	+0.0023
^{241}Pu	+0.0015
^{241}Am	+0.0015
^{243}Am	+0.0014
^{237}Np	+0.0014
^{242}Am*	-0.0014
^{238}U	+0.0012
^{243}Cm	-0.0008
^{245}Cm	-0.0005
^{235}U	-0.0005

Lastly, the multigroup model ignores many reaction channels that are assumed to be unimportant. While individual channels have only minor effects, the summation of all unobserved reactions may be non-trivial. Define the missing channel fraction m_f as the maximum over all time of the total one-group cross section less the sum of all other constituent reaction cross sections.

$$m_f = \max_\tau \left[1 - \frac{\sum_{r_x \neq t} \sigma_{r_x, i\tau}}{\sigma_{t, i\tau}} \right] \tag{5.52}$$

192

Table 5.12: Maximum Fission Product σ_s Relative Error

Nuclide	ε
^{140}Ba	+0.1758
^{148}Sm	+0.1069
^{147}Pm	-0.0970
^{133}Ba	-0.0787
^{59}Ni	+0.0717
^{125}Sn	+0.0454
^{155}Eu	+0.0308
^{93}Zr	-0.0149
^{126}Sb	+0.0099
^{107}Pd	+0.0068
^{126}Sn	-0.0051
^{136}Cs	-0.0051
^{151}Sm	-0.0039
^{94}Nb	-0.0039
^{135}Cs	+0.0032
^{95}Zr	+0.0032
^{129}I	+0.0030
^{154}Eu	-0.0027
^{152}Eu	-0.0027
^{125}Sb	-0.0022

Table 5.13: Maximum Actinide σ_a Relative Error

Nuclide	ε
^{240}Pu	+0.0681
^{236}U	+0.0385
^{242}Pu	+0.0361
^{244}Cm	-0.0245
^{246}Cm	-0.0238
^{242}Cm	-0.0187
^{238}Pu	-0.0169
^{234}U	+0.0157
^{239}Pu	-0.0132
^{243}Am	+0.0118
^{241}Am	+0.0108
^{237}Np	+0.0101
^{242}Am*	-0.0100
^{241}Pu	-0.0087
^{238}U	+0.0067
^{235}U	-0.0064
^{245}Cm	-0.0047
^{243}Cm	-0.0021

Table 5.14: Maximum Fission Product σ_a Relative Error

Nuclide	ε
^{125}Sn	+0.3471
^{140}Ba	+0.1927
^{133}Ba	-0.1815
^{148}Sm	+0.1523
^{147}Pm	-0.1000
^{126}Sb	+0.0955
^{94}Nb	-0.0722
^{93}Zr	-0.0624
^{59}Ni	+0.0378
^{135}Cs	-0.0309
^{155}Eu	+0.0235
^{99}Tc	-0.0200
^{154}Eu	-0.0168
^{152}Eu	-0.0149
^{85}Kr	-0.0134
^{113}Cd*	-0.0117
^{107}Pd	-0.0115
^{149}Eu	+0.0114
^{126}Sn	-0.0109
^{150}Eu	+0.0103

Table 5.15: Maximum Actinide σ_f Relative Error

Nuclide	ε
^{236}U	+0.0150
^{239}Pu	-0.0122
^{238}Pu	-0.0105
^{242}Am*	-0.0099
^{246}Cm	-0.0085
^{241}Pu	-0.0082
^{241}Am	+0.0071
^{235}U	-0.0061
^{240}Pu	+0.0049
^{245}Cm	-0.0046
^{238}U	+0.0040
^{242}Cm	-0.0032
^{237}Np	+0.0023
^{244}Cm	-0.0023
^{243}Cm	-0.0020
^{243}Am	+0.0012
^{242}Pu	+0.0010
^{234}U	+0.0010

Table 5.16 displays the sorted (highest to lowest) missing channel fractions for all nuclides tracked. Since nearly all of the m_f values are less than 5%, the assumption that the untracked channels are individually unimportant remains sound.

Table 5.16: Missing Channel Fraction

Nuclide	m_f
^{124}Sb	+0.0604
^{126}Sb	+0.0519
^{125}Sn	+0.0486
^{238}U	+0.0459
^{107}Pd	+0.0453
^{136}Cs	+0.0404
^{85}Kr	+0.0404
^{106}Ru	+0.0386
^{133}Ba	+0.0376
^{232}Th	+0.0373
^{244}Pu	+0.0329
^{129}I	+0.0317
^{242}Cm	+0.0314
^{134}Cs	+0.0311
^{99}Tc	+0.0295
^{252}Cf	+0.0289
^{94}Nb	+0.0283
^{123}Sn	+0.0273
^{79}Se	+0.0270
^{137}Cs	+0.0260

5.5 Conclusion & Future Work

The multigroup reactor model presented in this study provides a method for dynamically computing group constants for any reactor state. While the

initial cross section library generation stage may be computationally expensive (days), the resulting RMG calculations execute in seconds. This dramatic difference in time scales makes the RMG well-suited to nuclear fuel cycle simulations.

Still, the RMG is subject to certain natural constraints. First, in moving from one- to G-groups, the RMG will take more computational resources to execute than the one-group reactor model previously presented. However, the benefit of using additional groups is that the flux spectrum is allowed to change over the course of the fuel burn. For fast reactors, changes in the spectrum are minimal so the error induced by the R1G from a static spectrum is negligible. On the other hand, the RMG enables appropriate modeling of forms such as inert matrix fuel [40] for which R1G models could not capture dramatic shifts in local spectra induced by the compositional evolution of in-core material.

Another constraint with the RMG as formulated is that a multidimensional linear interpolation is used when calculating $\sigma_{r_x,i\tau g}$ from the reactor library $\sigma_{r_x,ipg}$. Therefore, in order to capture non-linear effects in the cross sections, a refinement to the time grid may be required if the number of steps is too coarse in the area of interest. This problem may be solved in other ways as well. Foremost among these would be to project the current reactor state onto a set of basis states defined from the perturbations. A linear combination of these basis states could then be used to obtain more representative interpolation coefficients. Another alternative would be to use a higher order polynomial fit or a spline interpolation to remove the use of a simple linear

interpolation.

Moreover, the perturbation table as formulated is static. Simple changes to the table require a complete re-computation of the outer product of all parameters. While not computationally intensive on its own, the perturbation table determines the state of the reactor and thus the value of all of the group constants in the reactor library.

A more dynamic perturbation table, and thus more dynamic reactor library, would allow for the RMG to handle an increased number of reactor cases without causing a reset of all cases previously computed. One method of implementation would be to allow the parameters in the perturbation table to be stochastically generated. Each parameter a_p would be given a range on which it would be randomly sampled to form a perturbation vector. Such an implementation would enable the easy extension of the perturbation table in that adding rows would not require a re-computation of the outer product. Where this ability becomes particularly important is in the case where there are a large number of parameters, such as the strategy in which the initial concentration of every actinide is varied. Here, the option space is much more efficiently covered by a stochastic perturbation table than an outer product one.

Lastly, refinements and optimizations to the existing model may be made. For example, the current transmutation calculation is carried by ORI-GEN to avoid writing a custom Bateman equation solver. More sophisticated methods which minimize global error could be implemented into the RMG.

199

However, the matrix exponential method used here is sufficient for most cal-
culations.

Chapter 6

Conclusion

Previous NFC simulators were either not physics-based models which could capture perturbations made to the system or had prohibitively long run times when perturbations were introduced. Because of these limitations, only static base cases and linear sensitivity analyses have historically been considered. Though such base cases were often chosen on the informed knowledge of the system designer, large gaps in the analysis space existed. The essential physics models presented here address all such limitations.

Essential physics methods in the context of the nuclear fuel cycle are models in which only the internal parameters affecting system wide metrics (such as material flow or electricity production) are explicitly solved for. Essential physics modeling approaches represent a balance of simplicity of fidelity as deemed appropriate based on the analysis needs of the modeler. By restricting the subset of calculations performed, such methods are many orders of magnitude faster than first-principle methods. Moreover, these models remain physically valid in the local range on which they are defined. Thus perturbing their initial conditions yields appropriate responses to the final state in ways that linear or statistical parametric fits are not capable of.

These essential physics reactor models have been used to examine three fuel cycles in depth: Once-Through, RU, and FR cases. Departing from discrete, pre-defined scenario studies, they were next used to perform a stochastic entropy-based sensitivity analysis on thirty design parameters in a fast burner recycle scenario. However, the one-energy group reactor model originally demonstrated, which was sufficient for fast reactors and (to a lesser degree) uranium-fueled light water reactors, failed to capture spectral changes in the core as a function of burnup. Therefore to enable the analysis of other fuel cycles, a multigroup reactor model was implemented.

The analysis that was performed herein was facilitated by the essential physics models themselves. Low-fidelity (lookup-table) models do not allow for perturbations that respond in a physics-based way. High-fidelity models continue to have prohibitive execution times in the context of fuel cycle simulation. By achieving fast, physics-based results these models increase the information generated by the corresponding simulations. Moreover, the speed and fidelity at which these models operate *enables* the new fuel cycle analytics used.

In conclusion, these methods form a suite of modeling technologies which reach from the lowest levels (individual components) to the highest (inter-cycle comparisons). Prior to the development of this model suite, such broad-ranging analysis had been unrealistic to perform. The work here thus presents a new, multi-scale approach to fuel cycle system design. Because of these essential physics models, it is now possible to tightly couple engineer-

ing concerns from multiple components simultaneously. When assessing the impact of any proposed fuel cycle change, or when attempting to balance the relative merits of one cycle to another, the ability to track perturbation effects through the entire system becomes essential.

Appendices

Appendix A

Serpent Input Decks

The following displays sample Serpent input input decks that were used in the benchmark case for the multigroup model. Serpent was run in both burnup and cross section generation modes. Both files are for the reactor at the beginning of life. First, a sample burnup file is presented below.

Listing A.1: Serpent Burnup Input Deck

```
set title "[CHAR] LWR Benchmark Burnup Calculation"
set acelib "/usr/share/serpent/xsdata/endf7.xsdata"


% —— Matrial Definitions ——
% Initial Fuel Stream
mat fuel −10.7 burn 10
    8016.06c   −0.11858
   92238.06c   −0.84176
   92235.06c   −0.039664

% Cladding Stream
mat cladding    −5.87
   50112.06c   −0.00014065
   40096.06c   −0.027478
   40090.06c   −0.50491
   24052.06c   −0.00083789
   40094.06c   −0.17056
   40091.06c   −0.11011
   28060.06c   −0.00014423
```

```
24053.06c    −9.501E−05
50114.06c    −9.425E−05
40092.06c    −0.1683
28058.06c    −0.00037442
24054.06c    −2.365E−05
50115.06c    −4.93E−05
 8016.06c    −0.00125
28061.06c    −6.27E−06
50116.06c    −0.0021083
28062.06c    −1.9987E−05
50117.06c    −0.0011136
26054.06c    −7.8908E−05
28064.06c    −5.093E−06
50119.06c    −0.0012441
26056.06c    −0.0012387
50122.06c    −0.00067135
26057.06c    −2.8607E−05
50120.06c    −0.0047256
26058.06c    −3.807E−06
50118.06c    −0.0035119
24050.06c    −4.345E−05
50124.06c    −0.00083955


% Coolant Stream
mat coolant    −0.73 moder lwtr 1001
    8016.06c    −0.8886
    1001.06c    −0.11107
    5010.06c    −6.0785E−05
    5011.06c    −0.00026914


therm lwtr lwj3.20t


% —— Run Specification ——
% Periodic boundary conditions
set bc 3
```

```
% 1/8 square symmetry
set sym 8

% Group Stucture
set egrid 5E-05 1E-09 10
set nfg 19
   1E-08
   1E-07
   1E-06
   1.6681E-06
   2.78256E-06
   4.64159E-06
   7.74264E-06
   1.29155E-05
   2.15443E-05
   3.59381E-05
   5.99484E-05
   0.0001
   0.00031623
   0.001
   0.00316228
   0.01
   0.1
   1

% Criticality calc
set pop 5000 130 30


% ---- Geometry ----
pin 1
fuel      0.41
void      0.4185
cladding 0.475
coolant

pin 2
```

coolant

lat 10 1 0.0 0.0 17 17 1.3127

```
1 1 1 1 1 1 1 1 1 1 1 1 1 1 1 1 1
1 1 1 1 1 1 1 1 1 1 1 1 1 1 1 1 1
1 1 1 1 1 2 1 1 2 1 1 2 1 1 1 1 1
1 1 1 2 1 1 1 1 1 1 1 1 1 2 1 1 1
1 1 1 1 1 1 1 1 1 1 1 1 1 1 1 1 1
1 1 2 1 1 2 1 1 2 1 1 2 1 1 2 1 1
1 1 1 1 1 1 1 1 1 1 1 1 1 1 1 1 1
1 1 1 1 1 1 1 1 1 1 1 1 1 1 1 1 1
1 1 2 1 1 2 1 1 2 1 1 2 1 1 2 1 1
1 1 1 1 1 1 1 1 1 1 1 1 1 1 1 1 1
1 1 1 1 1 1 1 1 1 1 1 1 1 1 1 1 1
1 1 2 1 1 2 1 1 2 1 1 2 1 1 2 1 1
1 1 1 1 1 1 1 1 1 1 1 1 1 1 1 1 1
1 1 1 2 1 1 1 1 1 1 1 1 1 2 1 1 1
1 1 1 1 1 2 1 1 2 1 1 2 1 1 1 1 1
1 1 1 1 1 1 1 1 1 1 1 1 1 1 1 1 1
1 1 1 1 1 1 1 1 1 1 1 1 1 1 1 1 1
```

surf 3000   sqc   0.0 0.0 11.15795
cell 300   0   **fill** 10   −3000
cell 301   0   outside   3000

% Decay and fission yield libraries
set declib "/usr/share/serpent/xsdata/sss_endfb7.dec"
set nfylib "/usr/share/serpent/xsdata/sss_endfb7.nfy"

% Burnup calculation options
set bumode   2   *% CRAM method*
set pcc   1   *% Predictor−corrector calculation on*
set xscalc   2   *% Calc cross sections from spectrum (fast)*

set powdens 0.04 *% Fuel specific power [W/g]*

208

% *Depletion cycle*
dep daytot

    40.56
    81.11
    121.7
    162.2
    202.8
    243.3
    283.9
    324.4
      365

% *Nuclide inventory*
set inventory

    10010
    10030
    20040
    60140
    80160
   110230
   170360
   280590
   280630
   340790
   360850
   380871
   380890
   380900
   380910
   380930
   380950
   380990
   381030
   390910

390930
400930
400950
410910
410931
410940
410950
410951
420930
430980
430990
441060
461070
471081
481131
501171
501191
501211
501230
501250
501251
501260
511240
511241
511250
511260
521251
531290
551340
551341
551350
551360
551370
551400
551410
551420
551430

551440
551450
551470
561330
561400
561410
611460
611470
621450
621480
621510
621550
631490
631500
631520
631540
631550
631560
822060
822070
822080
822100
832090
882260
882280
892270
902280
902290
902300
902320
912310
922300
922310
922320
922330
922340
922350

922360
922370
922380
922390
932350
932360
932361
932370
932380
932390
932400
932401
932410
942360
942370
942380
942390
942400
942410
942420
942430
942440
942450
942460
952390
952400
952410
952420
952421
952430
952440
952441
952450
952460
962410
962420
962430

```
962440
962450
962460
962470
962480
962490
962500
962510
972490
982490
982500
982510
982520
```

Next follows a Serpent input deck that was used to compute the ^{238}U group constants. Input files for other nuclides follow analogously.

Listing A.2: Serpent Cross Section Input Deck
```
set title "[CHAR] LWR Benchmark Cross Section Generator"
set acelib "/usr/share/serpent/xsdata/endf7.xsdata"

% ——— Matrial Definitions ———
% Initial Fuel Stream
mat fuel  −10.7
   92235.06c   −0.029256
   92238.06c   −0.62088
    8016.06c   −0.087465

% Cladding Stream
mat cladding    −5.87
   50112.06c   −0.00014065
   40096.06c   −0.027478
   40090.06c   −0.50491
   24052.06c   −0.00083789
   40094.06c   −0.17056
```

```
   40091.06c    −0.11011
   28060.06c    −0.00014423
   24053.06c    −9.501E−05
   50114.06c    −9.425E−05
   40092.06c    −0.1683
   28058.06c    −0.00037442
   24054.06c    −2.365E−05
   50115.06c    −4.93E−05
    8016.06c    −0.00125
   28061.06c    −6.27E−06
   50116.06c    −0.0021083
   28062.06c    −1.9987E−05
   50117.06c    −0.0011136
   26054.06c    −7.8908E−05
   28064.06c    −5.093E−06
   50119.06c    −0.0012441
   26056.06c    −0.0012387
   50122.06c    −0.00067135
   26057.06c    −2.8607E−05
   50120.06c    −0.0047256
   26058.06c    −3.807E−06
   50118.06c    −0.0035119
   24050.06c    −4.345E−05
   50124.06c    −0.00083955

% Coolant Stream
mat coolant    −0.73 moder lwtr 1001
    8016.06c    −0.8886
    1001.06c    −0.11107
    5010.06c    −6.0785E−05
    5011.06c    −0.00026914

therm lwtr lwj3.20t


% —— Run Specification ——
% Periodic boundary conditions
```

214

```
set bc 3

% Fuel universe
set gcu 100

% 1/8 square symmetry
set sym 8

% Group Stucture
set egrid 5E−05 1E−09 10
set nfg 19
   1E−08
   1E−07
   1E−06
   1.6681E−06
   2.78256E−06
   4.64159E−06
   7.74264E−06
   1.29155E−05
   2.15443E−05
   3.59381E−05
   5.99484E−05
   0.0001
   0.00031623
   0.001
   0.00316228
   0.01
   0.1
   1

% Criticality calc
set pop 5000 130 30

% —— Geometry ——
pin 1
fill 100 0.41
void      0.4185
```

```
cladding  0.475
coolant

pin 2
coolant

surf 100  inf
cell  110  100  fuel     −100

lat  10  1  0.0  0.0  17  17  1.3127

1 1 1 1 1 1 1 1 1 1 1 1 1 1 1 1 1
1 1 1 1 1 1 1 1 1 1 1 1 1 1 1 1 1
1 1 1 1 1 2 1 1 2 1 1 2 1 1 1 1 1
1 1 1 2 1 1 1 1 1 1 1 1 2 1 1 1
1 1 1 1 1 1 1 1 1 1 1 1 1 1 1 1 1
1 1 2 1 1 2 1 1 2 1 1 2 1 1 2 1 1
1 1 1 1 1 1 1 1 1 1 1 1 1 1 1 1 1
1 1 1 1 1 1 1 1 1 1 1 1 1 1 1 1 1
1 1 2 1 1 2 1 1 2 1 1 2 1 1 2 1 1
1 1 1 1 1 1 1 1 1 1 1 1 1 1 1 1 1
1 1 1 1 1 1 1 1 1 1 1 1 1 1 1 1 1
1 1 2 1 1 2 1 1 2 1 1 2 1 1 2 1 1
1 1 1 1 1 1 1 1 1 1 1 1 1 1 1 1 1
1 1 1 2 1 1 1 1 1 1 1 1 2 1 1 1
1 1 1 1 1 2 1 1 2 1 1 2 1 1 1 1 1
1 1 1 1 1 1 1 1 1 1 1 1 1 1 1 1 1
1 1 1 1 1 1 1 1 1 1 1 1 1 1 1 1 1


surf 3000   sqc  0.0  0.0  11.15795
cell  300     0   fill  10    −3000
cell  301     0   outside    3000


% —— Group Constant Generation ——
% Energy group structure
```

```
ene energies 1
    1E−09
    1E−08
    1E−07
    1E−06
    1.6681E−06
    2.78256E−06
    4.64159E−06
    7.74264E−06
    1.29155E−05
    2.15443E−05
    3.59381E−05
    5.99484E−05
    0.0001
    0.00031623
    0.001
    0.00316228
    0.01
    0.1
    1
    10


% Total flux in fuel
det phi de energies dm fuel

% Group constant material
mat xsmat 1.0 92238.06c 1.0

% Set group transfer probability to this material
set gtpmat xsmat

% Specify the detectors
det sigma_2n de energies dm fuel dr 16 xsmat dt 3 phi
det sigma_t de energies dm fuel dr 1 xsmat dt 3 phi
det nubar_sigma_f de energies dm fuel dr −7 xsmat dt 3 phi
det sigma_f de energies dm fuel dr 18 xsmat dt 3 phi
det sigma_e de energies dm fuel dr 2 xsmat dt 3 phi
```

```
det sigma_gamma de energies dm fuel dr 102 xsmat dt 3 phi
det sigma_i5 de energies dm fuel dr 55 xsmat dt 3 phi
det sigma_i4 de energies dm fuel dr 54 xsmat dt 3 phi
det sigma_i3 de energies dm fuel dr 53 xsmat dt 3 phi
det sigma_i2 de energies dm fuel dr 52 xsmat dt 3 phi
det sigma_i1 de energies dm fuel dr 51 xsmat dt 3 phi
```

Appendix B

Integration of Double Differential Scattering Cross Section Over Solid Angle

Suppose that equation B.1 is a continuous energy, double differential model of the scattering cross section [21, 47].

$$\frac{d^2}{dE'd\Omega}\sigma_s(E \to E', \Omega \to \Omega') = \frac{b^2}{kT} \cdot \sqrt{\frac{E'}{E}}e^{-\frac{\beta}{2}}S(\alpha, \beta) \qquad \text{(B.1)}$$

where b [cm] is the bound scattering length of the target nucleus, E [MeV] is the incident neutron energy, E' [MeV] is exiting neutron energy, Ω [sr] is the incident neutron solid angle, Ω' [sr] is the exiting neutron solid angle, m_n is mass of the neutron, M_A is the mass of the target nucleus, and k [MeV/K] is Boltzmann's constant. Note that the term $S(\alpha, \beta)$ is the scattering kernel with the scattering parameters α and β.

$$\alpha = \frac{E' + E - 2\sqrt{E'E}\cos(\theta)}{\frac{M_A}{m_n}kT} \qquad \text{(B.2)}$$

$$\beta = \frac{E' - E}{kT} \qquad \text{(B.3)}$$

Using the free gas approximation, $S(\alpha, \beta)$ is modeled as seen in equation B.4.

$$S(\alpha, \beta) = \frac{1}{\sqrt{4\pi\alpha}}\text{Exp}\left(-\frac{\alpha^2 + \beta^2}{4\alpha}\right) \qquad \text{(B.4)}$$

By integrating the double differential scattering cross section over all solid angles Ω, an energy-only expression may be obtained.

Begin by noting that the only term in equation B.1 that is dependent on the scattering angle is the kernel $S(\alpha, \beta)$. Thus defining K such that,

$$K = \frac{b^2}{kT}\sqrt{\frac{E'}{E}} \tag{B.5}$$

equation B.1 becomes equation B.6.

$$\frac{d^2}{dE'd\Omega}\sigma_s(E \to E', \Omega \to \Omega') = K \cdot e^{-\frac{\beta}{2}} \cdot \frac{e^{-\frac{\alpha^2+\beta^2}{4\alpha}}}{\sqrt{4\pi\alpha}} \tag{B.6}$$

This expression in turn may be integrated over all scattering angle, on which only α is dependent for a free gas.

$$\frac{d\sigma_s(E \to E')}{dE'} = K \cdot e^{-\frac{\beta}{2}} \cdot \int_\Omega \frac{e^{-\frac{\alpha^2+\beta^2}{4\alpha}}}{\sqrt{4\pi\alpha}}d\Omega \tag{B.7}$$

Expanding the Ω into its azimuthal and inclination angle components, the integral in equation B.7 may be reduced as follows.

$$\int_\Omega \frac{e^{-\frac{\alpha^2+\beta^2}{4\alpha}}}{\sqrt{4\pi\alpha}}d\Omega = \int_0^{2\pi}\int_0^\pi \frac{e^{-\frac{\alpha^2+\beta^2}{4\alpha}}}{\sqrt{4\pi\alpha}}\sin(\theta)d\theta d\phi = 2\pi\int_0^\pi \frac{e^{-\frac{\alpha^2+\beta^2}{4\alpha}}}{\sqrt{4\pi\alpha}}\sin(\theta)d\theta \tag{B.8}$$

Now making a change of variables by setting $\mu = \cos(\theta)$, the integral in equation B.8 becomes,

$$\sqrt{\pi}\int_1^{-1} \frac{e^{-\frac{\alpha^2+\beta^2}{4\alpha}}}{\sqrt{\alpha}}\sin(\theta)\frac{-d\mu}{\sin(\theta)} = \sqrt{\pi}\int_{-1}^1 \frac{e^{-\frac{\alpha^2+\beta^2}{4\alpha}}}{\sqrt{\alpha}}d\mu \tag{B.9}$$

Performing another change of variables from μ to α, the relationship L is found between the differentials.

$$\frac{d\mu}{d\alpha} = -\frac{2\sqrt{E'E}}{\frac{M_A}{m_n}kT} = L \tag{B.10}$$

220

The limits on the integrand are thus defined as follows.

$$\alpha_{\pm 1} = \frac{E' + E \mp 2\sqrt{E'E}}{\frac{M_A}{m_n} kT} \tag{B.11}$$

Thus the evaluation of the integral becomes dependent on the error function.

$$\frac{\sqrt{\pi}}{L} \int_{\alpha_{-1}}^{\alpha_1} \frac{e^{-\frac{\alpha^2 + \beta^2}{4\alpha}}}{\sqrt{\alpha}} d\alpha = \frac{\pi}{L} e^{-\frac{|\beta|}{2}} \left. \left(e^{|\beta|} \mathrm{Erf}\left[\frac{|\beta| + \alpha}{2\sqrt{\alpha}}\right] - \mathrm{Erf}\left[\frac{|\beta| - \alpha}{2\sqrt{\alpha}}\right] - e^{|\beta|} + 1 \right) \right|_{\alpha_{-1}}^{\alpha_1} \tag{B.12}$$

The terms in this evaluation that are not dependent on α disappear when the limits are applied.

$$\frac{\sqrt{\pi}}{L} \int_{\alpha_{-1}}^{\alpha_1} \frac{e^{-\frac{\alpha^2 + \beta^2}{4\alpha}}}{\sqrt{\alpha}} d\alpha = \frac{\pi}{L} \left. \left(e^{\frac{|\beta|}{2}} \mathrm{Erf}\left[\frac{|\beta| + \alpha}{2\sqrt{\alpha}}\right] - e^{-\frac{|\beta|}{2}} \mathrm{Erf}\left[\frac{|\beta| - \alpha}{2\sqrt{\alpha}}\right] \right) \right|_{\alpha_{-1}}^{\alpha_1} \tag{B.13}$$

Adding in the $e^{-\frac{\beta}{2}}$ term from equation B.7,

$$e^{-\frac{\beta}{2}} \frac{\sqrt{\pi}}{L} \int_{\alpha_{-1}}^{\alpha_1} \frac{e^{-\frac{\alpha^2 + \beta^2}{4\alpha}}}{\sqrt{\alpha}} d\alpha = \frac{\pi}{L} \left. \left(e^{-\frac{\beta - |\beta|}{2}} \mathrm{Erf}\left[\frac{|\beta| + \alpha}{2\sqrt{\alpha}}\right] - e^{-\frac{\beta + |\beta|}{2}} \mathrm{Erf}\left[\frac{|\beta| - \alpha}{2\sqrt{\alpha}}\right] \right) \right|_{\alpha_{-1}}^{\alpha_1} \tag{B.14}$$

This expression may be further simplified to

$$e^{-\frac{\beta}{2}} \frac{\sqrt{\pi}}{L} \int_{\alpha_{-1}}^{\alpha_1} \frac{e^{-\frac{\alpha^2 + \beta^2}{4\alpha}}}{\sqrt{\alpha}} d\alpha = \frac{\pi}{L} \left(Q^+(\alpha, \beta) - Q^-(\alpha, \beta) \right) \tag{B.15}$$

by defining a Q such that

$$Q^{\pm}(\alpha, \beta) = e^{-\frac{\beta \mp |\beta|}{2}} \left(\mathrm{Erf}\left[\frac{|\beta| \pm \alpha_1}{2\sqrt{\alpha_1}}\right] - \mathrm{Erf}\left[\frac{|\beta| \pm \alpha_{-1}}{2\sqrt{\alpha_{-1}}}\right] \right) \tag{B.16}$$

Note that the term $e^{-\frac{\beta - |\beta|}{2}}$ in $Q^+(\alpha, \beta)$ has a special meaning for up-scattering and down-scattering events. For up-scattering it is unity and for down-scattering

it becomes simply $e^{-\beta}$. For the $e^{-\frac{\beta+|\beta|}{2}}$ in $Q^-(\alpha, \beta)$, the simplifications are inverted.

Therefore the differential equation for the scattering cross section is seen to be

$$\frac{d\sigma_s(E \to E')}{dE'} = \frac{\pi K}{L} \left(Q^+(\alpha, \beta) - Q^-(\alpha, \beta) \right) \tag{B.17}$$

where

$$\frac{\pi K}{L} = \frac{\pi b^2}{kT} \sqrt{\frac{E'}{E}} \left(\frac{-kT}{2\sqrt{E'E}} \right) \frac{M_A}{m_n} = -\frac{\pi b^2}{2E} \frac{M_A}{m_n} \tag{B.18}$$

which yields the final expression for the integral of double differential scattering cross section.

$$\frac{d\sigma_s(E \to E')}{dE'} = \frac{\pi b^2}{2E} \frac{M_A}{m_n} \left(Q^-(\alpha, \beta) - Q^+(\alpha, \beta) \right) \tag{B.19}$$

Appendix C

Multigroup Reactor Nuclide Lists

The cross sections for the multigroup reactor model library may be calculated in one of three different ways: via Serpent, via physical models, or via interpolation. What follows here is a listing of which nuclides are treated by which methods. For the Serpent case, which reaction channels are available are also listed in a separate table.

Table C.1: Nuclides Calculated via Serpent

^{1}H	^{3}H	^{4}He
^{16}O	^{23}Na	^{59}Ni
^{79}Se	^{85}Kr	^{89}Sr
^{90}Sr	^{91}Y	^{93}Zr
^{95}Zr	^{94}Nb	^{95}Nb
^{99}Tc	^{106}Ru	^{107}Pd
^{123}Sn	^{125}Sn	^{126}Sn
^{124}Sb	^{125}Sb	^{126}Sb
^{129}I	^{134}Cs	^{135}Cs
^{136}Cs	^{137}Cs	^{133}Ba
^{140}Ba	^{147}Pm	^{148}Sm
^{151}Sm	^{152}Eu	^{154}Eu
^{155}Eu	^{156}Eu	^{206}Pb
^{207}Pb	^{208}Pb	^{209}Bi
^{226}Ra	^{227}Ac	^{228}Th
^{229}Th	^{230}Th	^{232}Th
^{231}Pa	^{232}U	^{233}U
^{234}U	^{235}U	^{236}U
^{237}U	^{238}U	^{239}U
^{235}Np	^{236}Np	^{237}Np
^{238}Np	^{239}Np	^{236}Pu
^{237}Pu	^{238}Pu	^{239}Pu
^{240}Pu	^{241}Pu	^{242}Pu
^{243}Pu	^{244}Pu	^{246}Pu
^{241}Am	^{242}Am	^{242}Am*
^{243}Am	^{244}Am	^{244}Am*
^{241}Cm	^{242}Cm	^{243}Cm
^{244}Cm	^{245}Cm	^{246}Cm
^{247}Cm	^{248}Cm	^{249}Cm
^{250}Cm	^{249}Bk	^{249}Cf
^{250}Cf	^{251}Cf	^{252}Cf

Table C.2: Reactions Available in Serpent (Part 1)

nuclides	reactions
^{1}H	t, e, γ
^{3}H	$t, e, 2n$
^{4}He	t, e
^{16}O	$t, e, i1, i2, i3, i4, i5, \gamma, \alpha$
^{23}Na	$t, e, i1, i2, i3, i4, i5, \gamma, p, \alpha$
^{59}Ni	$t, e, 2n, \gamma, p, d, {}^{3}\text{H}, {}^{3}\text{He}, \alpha$
^{79}Se	$t, e, 2n, i1, i2, i3, i4, i5, \gamma, p, d, {}^{3}\text{H}, \alpha$
^{85}Kr	$t, e, 2n, i1, i2, i3, i4, i5, \gamma, p, \alpha$
^{89}Sr	$t, e, 2n, i1, i2, i3, i4, i5, \gamma, p, \alpha$
^{90}Sr	$t, e, 2n, i1, i2, i3, i4, i5, \gamma, p, d, \alpha$
^{91}Y	$t, e, 2n, i1, i2, i3, i4, i5, \gamma, p, d, {}^{3}\text{H}, \alpha$
^{93}Zr	$t, e, 2n, i1, i2, i3, i4, i5, \gamma, p, d, {}^{3}\text{H}, \alpha$
^{95}Zr	$t, e, 2n, i1, i2, i3, i4, i5, \gamma, p, d, {}^{3}\text{H}, \alpha$
^{94}Nb	$t, e, i, 2n, i1, i2, i3, i4, i5, \gamma, p, d, {}^{3}\text{H}, {}^{3}\text{He}, \alpha$
^{95}Nb	$t, e, 2n, i1, i2, i3, i4, i5, \gamma, p, d, {}^{3}\text{H}, \alpha$
^{99}Tc	$t, e, 2n, i1, i2, i3, i4, i5, \gamma, p, \alpha$
^{106}Ru	$t, e, 2n, i1, i2, i3, i4, \gamma, p, d, \alpha$
^{107}Pd	$t, e, 2n, i1, i2, i3, i4, i5, \gamma, p, d, {}^{3}\text{H}, \alpha$
^{123}Sn	$t, e, 2n, i1, i2, i3, i4, i5, \gamma, p, \alpha$
^{125}Sn	$t, e, 2n, i1, i2, i3, i4, i5, \gamma, p, \alpha$
^{126}Sn	$t, e, 2n, i1, i2, i3, i4, i5, \gamma, p, \alpha$
^{124}Sb	$t, e, i, 2n, i1, \gamma, p, d, {}^{3}\text{H}, \alpha$
^{125}Sb	$t, e, 2n, i1, i2, i3, i4, i5, \gamma, p, d, {}^{3}\text{H}, \alpha$
^{126}Sb	$t, e, 2n, i1, i2, i3, i4, i5, \gamma, p, \alpha$
^{129}I	$t, e, 2n, i1, i2, i3, i4, i5, \gamma, p, d, {}^{3}\text{H}, \alpha$
^{134}Cs	$t, e, i, 2n, i1, i2, i3, i4, i5, \gamma, p, d, {}^{3}\text{H}, \alpha$
^{135}Cs	$t, e, 2n, i1, i2, i3, i4, \gamma, p, d, {}^{3}\text{H}, \alpha$
^{136}Cs	$t, e, 2n, \gamma, p, d, {}^{3}\text{H}, \alpha$
^{137}Cs	$t, e, 2n, i1, i2, i3, i4, i5, \gamma, p, d, {}^{3}\text{H}, \alpha$
^{133}Ba	$t, e, 2n, i1, i2, i3, i4, i5, \gamma, p, \alpha$
^{140}Ba	$t, e, 2n, \gamma, p, d, {}^{3}\text{H}, \alpha$
^{147}Pm	$t, e, 2n, i1, i2, i3, i4, i5, \gamma, p, d, {}^{3}\text{H}, \alpha$
^{148}Sm	$t, e, 2n, i1, i2, i3, i4, i5, \gamma, p, \alpha$
^{151}Sm	$t, e, 2n, i1, i2, i3, i4, i5, \gamma, p, \alpha$
^{152}Eu	$t, e, i, 2n, i1, i2, i3, i4, i5, \gamma, p, d, {}^{3}\text{H}, {}^{3}\text{He}, \alpha$
^{154}Eu	$t, e, i, 2n, i1, i2, i3, i4, i5, \gamma, p, d, {}^{3}\text{H}, \alpha$

Table C.3: Reactions Available in Serpent (Part 2)

nuclides	reactions
^{155}Eu	t, e, $2n$, $i1$, $i2$, $i3$, $i4$, $i5$, γ, p, d, ^{3}H, α
^{156}Eu	t, e, i, $2n$, $i1$, $i2$, $i3$, $i4$, $i5$, γ, p, d, ^{3}H, α
^{206}Pb	t, e, $2n$, $i1$, $i2$, $i3$, $i4$, $i5$, γ, p, d, ^{3}H, α
^{207}Pb	t, e, $2n$, $i1$, $i2$, $i3$, $i4$, $i5$, γ, p, d, ^{3}H, α
^{208}Pb	t, e, $2n$, $i1$, $i2$, $i3$, $i4$, $i5$, γ, p, d, ^{3}H, α
^{209}Bi	t, e, $2n$, $i1$, $i2$, $i3$, $i4$, $i5$, γ, p, d, ^{3}H, ^{3}He, α
^{226}Ra	t, e, $2n$, f, $i1$, $i2$, $i3$, $i4$, $i5$, γ
^{227}Ac	t, e, $2n$, f, $i1$, $i2$, $i3$, $i4$, $i5$, γ
^{228}Th	t, e, $2n$, f, $i1$, $i2$, $i3$, $i4$, $i5$, γ
^{229}Th	t, e, $2n$, f, $i1$, $i2$, $i3$, $i4$, γ
^{230}Th	t, e, $2n$, f, $i1$, $i2$, $i3$, $i4$, $i5$, γ
^{232}Th	t, e, $2n$, f, $i1$, $i2$, $i3$, $i4$, $i5$, γ
^{231}Pa	t, e, i, $2n$, f, $i1$, $i2$, $i3$, $i4$, $i5$, γ
^{232}U	t, e, $2n$, $f19$, $f20$, $f21$, $i1$, $i2$, $i3$, $i4$, $i5$, γ
^{233}U	t, e, i, $2n$, f, $i1$, $i2$, $i3$, $i4$, $i5$, γ
^{234}U	t, e, $2n$, $f19$, $f20$, $f21$, $i1$, $i2$, $i3$, $i4$, $i5$, γ
^{235}U	t, e, i, $2n$, f, $i1$, $i2$, $i3$, $i4$, $i5$, γ
^{236}U	t, e, $2n$, $f19$, $f20$, $i1$, $i2$, $i3$, $i4$, $i5$, γ
^{237}U	t, e, $2n$, f, $i1$, $i2$, $i3$, $i4$, $i5$, γ
^{238}U	t, e, $2n$, f, $i1$, $i2$, $i3$, $i4$, $i5$, γ
^{239}U	t, e, $2n$, f, $i1$, $i2$, $i3$, $i4$, $i5$, γ
^{235}Np	t, e, $2n$, f, $i1$, $i2$, $i3$, $i4$, $i5$, γ
^{236}Np	t, e, $2n$, f, $i1$, $i2$, $i3$, $i4$, γ
^{237}Np	t, e, $2n$, f, $i1$, $i2$, $i3$, $i4$, $i5$, γ
^{238}Np	t, e, $2n$, f, $i1$, $i2$, $i3$, $i4$, $i5$, γ
^{239}Np	t, e, $2n$, f, $i1$, $i2$, $i3$, $i4$, $i5$, γ
^{236}Pu	t, e, $2n$, f, $i1$, $i2$, $i3$, $i4$, γ
^{237}Pu	t, e, $2n$, $f19$, $f20$, $i1$, $i2$, $i3$, $i4$, $i5$, γ
^{238}Pu	t, e, $2n$, $f19$, $f20$, $i1$, $i2$, $i3$, $i4$, $i5$, γ
^{239}Pu	t, e, i, $2n$, f, $i1$, $i2$, $i3$, $i4$, $i5$, γ
^{240}Pu	t, e, i, $2n$, $f19$, $f20$, $i1$, $i2$, $i3$, $i4$, $i5$, γ
^{241}Pu	t, e, $2n$, f, $i1$, $i2$, $i3$, $i4$, $i5$, γ
^{242}Pu	t, e, $2n$, f, $i1$, $i2$, $i3$, $i4$, $i5$, γ
^{243}Pu	t, e, $2n$, f, γ
^{244}Pu	t, e, $2n$, $f19$, $f20$, $i1$, $i2$, $i3$, $i4$, $i5$, γ

Table C.4: Reactions Available in Serpent (Part 3)

nuclides	reactions
^{246}Pu	t, e, $2n$, f, $i1$, $i2$, γ
^{241}Am	t, e, $2n$, f, $i1$, $i2$, $i3$, $i4$, $i5$, γ
^{242}Am	t, e, $2n$, f, $i1$, $i2$, $i3$, $i4$, $i5$, γ
^{242}Am*	t, e, i, $2n$, f, $i1$, $i2$, $i3$, $i4$, $i5$, γ
^{243}Am	t, e, $2n$, f, $i1$, $i2$, $i3$, $i4$, $i5$, γ
^{244}Am	t, e, $2n$, f, $i1$, $i2$, $i3$, $i4$, $i5$, γ
^{244}Am*	t, e, $2n$, f, $i1$, $i2$, $i3$, $i4$, $i5$, γ
^{241}Cm	t, e, $2n$, $f19$, $i1$, $i2$, $i3$, $i4$, γ
^{242}Cm	t, e, $2n$, $f19$, $f20$, $i1$, $i2$, $i3$, γ
^{243}Cm	t, e, $2n$, $f19$, $f20$, $i1$, $i2$, $i3$, $i4$, $i5$, γ
^{244}Cm	t, e, $2n$, f, $i1$, $i2$, $i3$, $i4$, $i5$, γ
^{245}Cm	t, e, $2n$, f, $i1$, $i2$, $i3$, $i4$, $i5$, γ
^{246}Cm	t, e, $2n$, $f19$, $f20$, $i1$, $i2$, $i3$, $i4$, $i5$, γ
^{247}Cm	t, e, $2n$, f, $i1$, $i2$, $i3$, $i4$, $i5$, γ
^{248}Cm	t, e, $2n$, $f19$, $f20$, $i1$, $i2$, $i3$, $i4$, $i5$, γ
^{249}Cm	t, e, $2n$, f, $i1$, $i2$, $i3$, $i4$, $i5$, γ
^{250}Cm	t, e, $2n$, f, $i1$, $i2$, γ
^{249}Bk	t, e, $2n$, f, $i1$, $i2$, $i3$, $i4$, $i5$, γ, p, α
^{249}Cf	t, e, $2n$, f, $i1$, $i2$, $i3$, $i4$, $i5$, γ, p, α
^{250}Cf	t, e, $2n$, f, γ
^{251}Cf	t, e, $2n$, f, γ
^{252}Cf	t, e, $2n$, f, γ

Table C.5: Nuclides Calculated via Models

^{14}C	^{36}Cl	^{63}Ni
^{87}Sr*	^{91}Sr	^{93}Sr
^{95}Sr	^{99}Sr	^{103}Sr
^{93}Y	^{91}Nb	^{93}Nb*
^{95}Nb*	^{93}Mo	^{98}Tc
^{108}Ag*	^{113}Cd*	^{117}Sn*
^{119}Sn*	^{121}Sn*	^{125}Sn*
^{124}Sb*	^{125}Te*	^{134}Cs*
^{140}Cs	^{141}Cs	^{142}Cs
^{143}Cs	^{144}Cs	^{145}Cs
^{147}Cs	^{141}Ba	^{146}Pm
^{145}Sm	^{155}Sm	^{149}Eu
^{150}Eu	^{210}Pb	^{228}Ra
^{230}U	^{231}U	^{236}Np*
^{240}Np	^{240}Np*	^{241}Np
^{245}Pu	^{239}Am	^{240}Am
^{245}Am	^{246}Am	^{251}Cm

Table C.6: Nuclides Calculated via Interpolation (Part 1)

^{2}H	^{3}He	^{5}He	^{6}He	^{7}He	^{8}He
^{4}Li	^{6}Li	^{7}Li	^{8}Li	^{9}Li	^{11}Li
^{6}Be	^{7}Be	^{8}Be	^{9}Be	^{10}Be	^{11}Be
^{12}Be	^{13}Be	^{14}Be	^{7}B	^{9}B	^{10}B
^{11}B	^{12}B	^{13}B	^{14}B	^{15}B	^{16}B
^{17}B	^{8}C	^{9}C	^{10}C	^{11}C	^{12}C
^{13}C	^{15}C	^{16}C	^{17}C	^{18}C	^{19}C
^{20}C	^{1}N	^{11}N	^{12}N	^{13}N	^{14}N
^{15}N	^{16}N	^{16}N*	^{17}N	^{18}N	^{19}N
^{20}N	^{21}N	^{22}N	^{12}O	^{13}O	^{14}O
^{15}O	^{17}O	^{18}O	^{19}O	^{20}O	^{21}O
^{22}O	^{24}O	^{15}F	^{16}F	^{17}F	^{18}F
^{19}F	^{20}F	^{21}F	^{22}F	^{23}F	^{24}F
^{25}F	^{26}F	^{29}F	^{16}Ne	^{17}Ne	^{18}Ne
^{19}Ne	^{20}Ne	^{20}Ne*	^{21}Ne	^{22}Ne	^{23}Ne
^{24}Ne	^{25}Ne	^{26}Ne	^{28}Ne	^{29}Ne	^{29}Ne*
^{30}Ne	^{20}Na	^{21}Na	^{22}Na	^{24}Na	^{24}Na*
^{25}Na	^{26}Na	^{27}Na	^{28}Na	^{29}Na	^{30}Na
^{31}Na	^{32}Na	^{20}Mg	^{21}Mg	^{22}Mg	^{23}Mg
^{24}Mg	^{25}Mg	^{26}Mg	^{27}Mg	^{28}Mg	^{29}Mg
^{30}Mg	^{31}Mg	^{32}Mg	^{34}Mg	^{35}Mg	^{36}Mg
^{37}Mg	^{21}Al	^{22}Al	^{23}Al	^{24}Al	^{24}Al*
^{25}Al	^{26}Al	^{26}Al*	^{27}Al	^{28}Al	^{29}Al
^{30}Al	^{31}Al	^{32}Al	^{34}Al	^{35}Al	^{36}Al
^{37}Al	^{39}Al	^{22}Si	^{24}Si	^{25}Si	^{26}Si
^{27}Si	^{28}Si	^{29}Si	^{30}Si	^{31}Si	^{32}Si
^{34}Si	^{36}Si	^{37}Si	^{38}Si	^{39}Si	^{25}P
^{26}P	^{27}P	^{28}P	^{29}P	^{30}P	^{31}P
^{32}P	^{33}P	^{34}P	^{35}P	^{36}P	^{37}P
^{38}P	^{39}P	^{40}P	^{42}P	^{28}S	^{29}S
^{30}S	^{31}S	^{32}S	^{33}S	^{34}S	^{35}S
^{36}S	^{37}S	^{38}S	^{39}S	^{40}S	^{41}S
^{42}S	^{44}S	^{29}Cl	^{30}Cl	^{31}Cl	^{32}Cl
^{33}Cl	^{34}Cl	^{34}Cl*	^{35}Cl	^{37}Cl	^{38}Cl
^{38}Cl*	^{39}Cl	^{40}Cl	^{41}Cl	^{42}Cl	^{44}Cl
^{46}Cl	^{51}Cl	^{31}Ar	^{32}Ar	^{33}Ar	^{34}Ar

Table C.7: Nuclides Calculated via Interpolation (Part 2)

^{35}Ar	^{36}Ar	^{37}Ar	^{38}Ar	^{39}Ar	^{40}Ar
^{41}Ar	^{42}Ar	^{43}Ar	^{44}Ar	^{46}Ar	^{51}Ar
^{33}K	^{34}K	^{35}K	^{36}K	^{37}K	^{38}K
^{38}K*	^{39}K	^{40}K	^{41}K	^{42}K	^{43}K
^{44}K	^{45}K	^{46}K	^{47}K	^{48}K	^{49}K
^{50}K	^{51}K	^{34}Ca	^{36}Ca	^{37}Ca	^{38}Ca
^{39}Ca	^{40}Ca	^{41}Ca	^{42}Ca	^{43}Ca	^{44}Ca
^{45}Ca	^{46}Ca	^{47}Ca	^{48}Ca	^{49}Ca	^{50}Ca
^{51}Ca	^{52}Ca	^{53}Ca	^{38}Sc	^{40}Sc	^{41}Sc
^{42}Sc	^{42}Sc*	^{43}Sc	^{44}Sc	^{44}Sc*	^{45}Sc
^{45}Sc*	^{46}Sc	^{46}Sc*	^{47}Sc	^{48}Sc	^{49}Sc
^{50}Sc	^{50}Sc*	^{51}Sc	^{52}Sc	^{53}Sc	^{55}Sc
^{40}Ti	^{41}Ti	^{42}Ti	^{43}Ti	^{44}Ti	^{45}Ti
^{46}Ti	^{47}Ti	^{48}Ti	^{49}Ti	^{50}Ti	^{51}Ti
^{52}Ti	^{53}Ti	^{54}Ti	^{55}Ti	^{56}Ti	^{58}Ti
^{42}V	^{43}V	^{44}V	^{44}V*	^{45}V	^{46}V
^{46}V*	^{47}V	^{48}V	^{49}V	^{50}V	^{51}V
^{52}V	^{53}V	^{54}V	^{55}V	^{56}V	^{57}V
^{58}V	^{60}V	^{62}V	^{63}V	^{42}Cr	^{43}Cr
^{44}Cr	^{46}Cr	^{47}Cr	^{48}Cr	^{49}Cr	^{50}Cr
^{51}Cr	^{52}Cr	^{53}Cr	^{54}Cr	^{55}Cr	^{56}Cr
^{57}Cr	^{58}Cr	^{60}Cr	^{62}Cr	^{63}Cr	^{65}Cr
^{44}Mn	^{45}Mn	^{46}Mn	^{48}Mn	^{49}Mn	^{50}Mn
^{50}Mn*	^{51}Mn	^{52}Mn	^{52}Mn*	^{53}Mn	^{54}Mn
^{55}Mn	^{56}Mn	^{57}Mn	^{58}Mn	^{58}Mn*	^{59}Mn
^{60}Mn	^{60}Mn*	^{61}Mn	^{62}Mn	^{65}Mn	^{67}Mn
^{45}Fe	^{46}Fe	^{48}Fe	^{49}Fe	^{50}Fe	^{51}Fe
^{52}Fe	^{52}Fe*	^{53}Fe	^{53}Fe*	^{54}Fe	^{55}Fe
^{56}Fe	^{57}Fe	^{58}Fe	^{59}Fe	^{60}Fe	^{61}Fe
^{62}Fe	^{63}Fe	^{64}Fe	^{66}Fe	^{67}Fe	^{68}Fe
^{50}Co	^{51}Co	^{52}Co	^{53}Co	^{53}Co*	^{54}Co
^{54}Co*	^{55}Co	^{56}Co	^{57}Co	^{58}Co	^{58}Co*
^{59}Co	^{60}Co	^{60}Co*	^{61}Co	^{62}Co	^{62}Co*
^{63}Co	^{64}Co	^{65}Co	^{66}Co	^{67}Co	^{68}Co
^{50}Ni	^{51}Ni	^{52}Ni	^{53}Ni	^{54}Ni	^{55}Ni

Table C.8: Nuclides Calculated via Interpolation (Part 3)

^{56}Ni	^{57}Ni	^{58}Ni	^{60}Ni	^{61}Ni	^{62}Ni
^{64}Ni	^{65}Ni	^{66}Ni	^{67}Ni	^{68}Ni	^{72}Ni
^{74}Ni	^{75}Ni	^{76}Ni	^{78}Ni	^{53}Cu	^{54}Cu
^{56}Cu	^{57}Cu	^{58}Cu	^{59}Cu	^{60}Cu	^{61}Cu
^{62}Cu	^{63}Cu	^{64}Cu	^{65}Cu	^{66}Cu	^{67}Cu
^{68}Cu	^{68}Cu*	^{69}Cu	^{70}Cu	^{70}Cu*	^{71}Cu
^{72}Cu	^{74}Cu	^{75}Cu	^{76}Cu	^{78}Cu	^{56}Zn
^{57}Zn	^{59}Zn	^{60}Zn	^{61}Zn	^{62}Zn	^{63}Zn
^{64}Zn	^{65}Zn	^{66}Zn	^{67}Zn	^{68}Zn	^{69}Zn
^{69}Zn*	^{70}Zn	^{71}Zn	^{71}Zn*	^{72}Zn	^{73}Zn
^{73}Zn*	^{74}Zn	^{75}Zn	^{76}Zn	^{77}Zn	^{77}Zn*
^{78}Zn	^{79}Zn	^{80}Zn	^{81}Zn	^{82}Zn	^{61}Ga
^{62}Ga	^{63}Ga	^{64}Ga	^{65}Ga	^{66}Ga	^{67}Ga
^{68}Ga	^{69}Ga	^{70}Ga	^{71}Ga	^{72}Ga	^{73}Ga
^{74}Ga	^{74}Ga*	^{75}Ga	^{76}Ga	^{77}Ga	^{78}Ga
^{79}Ga	^{80}Ga	^{81}Ga	^{82}Ga	^{61}Ge	^{62}Ge
^{64}Ge	^{65}Ge	^{66}Ge	^{67}Ge	^{68}Ge	^{69}Ge
^{69}Ge*	^{70}Ge	^{71}Ge	^{71}Ge*	^{72}Ge	^{73}Ge
^{73}Ge*	^{74}Ge	^{75}Ge	^{75}Ge*	^{76}Ge	^{77}Ge
^{77}Ge*	^{78}Ge	^{79}Ge	^{79}Ge*	^{80}Ge	^{81}Ge
^{81}Ge*	^{82}Ge	^{83}Ge	^{84}Ge	^{66}As	^{67}As
^{68}As	^{69}As	^{70}As	^{71}As	^{72}As	^{73}As
^{74}As	^{75}As	^{76}As	^{77}As	^{77}As*	^{78}As
^{79}As	^{80}As	^{81}As	^{82}As	^{82}As*	^{83}As
^{84}As	^{85}As	^{86}As	^{87}As	^{66}Se	^{68}Se
^{69}Se	^{70}Se	^{71}Se	^{72}Se	^{73}Se	^{73}Se*
^{74}Se	^{75}Se	^{76}Se	^{77}Se	^{77}Se*	^{78}Se
^{79}Se*	^{80}Se	^{81}Se	^{81}Se*	^{82}Se	^{83}Se
^{83}Se*	^{84}Se	^{85}Se	^{86}Se	^{87}Se	^{88}Se
^{89}Se	^{92}Se	^{71}Br	^{72}Br	^{72}Br*	^{73}Br
^{74}Br	^{74}Br*	^{75}Br	^{76}Br	^{76}Br*	^{77}Br
^{77}Br*	^{78}Br	^{78}Br*	^{79}Br	^{79}Br*	^{80}Br
^{80}Br*	^{81}Br	^{82}Br	^{82}Br*	^{83}Br	^{84}Br
^{84}Br*	^{85}Br	^{86}Br	^{87}Br	^{88}Br	^{89}Br
^{90}Br	^{92}Br	^{93}Br	^{71}Kr	^{72}Kr	^{73}Kr

Table C.9: Nuclides Calculated via Interpolation (Part 4)

^{74}Kr	^{75}Kr	^{76}Kr	^{77}Kr	^{78}Kr	^{79}Kr
^{79}Kr*	^{80}Kr	^{81}Kr	^{81}Kr*	^{82}Kr	^{83}Kr
^{83}Kr*	^{84}Kr	^{85}Kr*	^{86}Kr	^{87}Kr	^{88}Kr
^{89}Kr	^{90}Kr	^{91}Kr	^{92}Kr	^{93}Kr	^{94}Kr
^{95}Kr	^{72}Rb	^{73}Rb	^{74}Rb	^{75}Rb	^{76}Rb
^{77}Rb	^{78}Rb	^{78}Rb*	^{79}Rb	^{80}Rb	^{81}Rb
^{81}Rb*	^{82}Rb	^{82}Rb*	^{83}Rb	^{84}Rb	^{84}Rb*
^{85}Rb	^{86}Rb	^{86}Rb*	^{87}Rb	^{88}Rb	^{89}Rb
^{90}Rb	^{90}Rb*	^{91}Rb	^{92}Rb	^{93}Rb	^{94}Rb
^{95}Rb	^{96}Rb	^{97}Rb	^{98}Rb	^{98}Rb*	^{99}Rb
^{101}Rb	^{74}Sr	^{76}Sr	^{77}Sr	^{78}Sr	^{79}Sr
^{80}Sr	^{81}Sr	^{82}Sr	^{83}Sr	^{83}Sr*	^{84}Sr
^{85}Sr	^{85}Sr*	^{86}Sr	^{86}Sr*	^{87}Sr	^{88}Sr
^{92}Sr	^{94}Sr	^{96}Sr	^{97}Sr	^{98}Sr	^{100}Sr
^{101}Sr	^{102}Sr	^{104}Sr	^{79}Y	^{80}Y	^{81}Y
^{82}Y	^{83}Y	^{83}Y*	^{84}Y	^{84}Y*	^{85}Y
^{85}Y*	^{86}Y	^{86}Y*	^{87}Y	^{87}Y*	^{88}Y
^{89}Y	^{89}Y*	^{90}Y	^{90}Y*	^{91}Y*	^{92}Y
^{93}Y*	^{94}Y	^{95}Y	^{96}Y	^{96}Y*	^{97}Y
^{97}Y*	^{98}Y	^{98}Y*	^{99}Y	^{99}Y*	^{100}Y
^{100}Y*	^{101}Y	^{102}Y	^{103}Y	^{104}Y	^{82}Zr
^{83}Zr	^{84}Zr	^{85}Zr	^{85}Zr*	^{86}Zr	^{87}Zr
^{87}Zr*	^{88}Zr	^{89}Zr	^{89}Zr*	^{90}Zr	^{90}Zr*
^{91}Zr	^{91}Zr*	^{92}Zr	^{94}Zr	^{96}Zr	^{97}Zr
^{98}Zr	^{99}Zr	^{100}Zr	^{101}Zr	^{102}Zr	^{103}Zr
^{104}Zr	^{108}Zr	^{83}Nb	^{84}Nb	^{85}Nb	^{86}Nb
^{87}Nb	^{87}Nb*	^{88}Nb	^{88}Nb*	^{89}Nb	^{89}Nb*
^{90}Nb	^{90}Nb*	^{91}Nb*	^{92}Nb	^{92}Nb*	^{93}Nb
^{94}Nb*	^{96}Nb	^{97}Nb	^{97}Nb*	^{98}Nb	^{98}Nb*
^{99}Nb	^{99}Nb*	^{100}Nb	^{100}Nb*	^{101}Nb	^{102}Nb
^{103}Nb	^{104}Nb	^{104}Nb*	^{105}Nb	^{106}Nb	^{108}Nb
^{84}Mo	^{85}Mo	^{86}Mo	^{87}Mo	^{88}Mo	^{89}Mo
^{89}Mo*	^{90}Mo	^{91}Mo	^{91}Mo*	^{92}Mo	^{93}Mo*
^{94}Mo	^{95}Mo	^{96}Mo	^{97}Mo	^{98}Mo	^{99}Mo
^{100}Mo	^{101}Mo	^{102}Mo	^{103}Mo	^{104}Mo	^{105}Mo

232

Table C.10: Nuclides Calculated via Interpolation (Part 5)

^{106}Mo	^{108}Mo	^{110}Mo	^{88}Tc	^{88}Tc*	^{89}Tc
^{89}Tc*	^{90}Tc	^{90}Tc*	^{91}Tc	^{91}Tc*	^{92}Tc
^{93}Tc	^{93}Tc*	^{94}Tc	^{94}Tc*	^{95}Tc	^{95}Tc*
^{96}Tc	^{96}Tc*	^{97}Tc	^{97}Tc*	^{99}Tc*	^{100}Tc
^{101}Tc	^{101}Tc*	^{102}Tc	^{102}Tc*	^{103}Tc	^{104}Tc
^{105}Tc	^{106}Tc	^{107}Tc	^{108}Tc	^{110}Tc	^{112}Tc
^{89}Ru	^{90}Ru	^{91}Ru	^{91}Ru*	^{92}Ru	^{93}Ru
^{93}Ru*	^{94}Ru	^{95}Ru	^{96}Ru	^{97}Ru	^{98}Ru
^{99}Ru	^{100}Ru	^{101}Ru	^{102}Ru	^{103}Ru	^{103}Ru*
^{104}Ru	^{105}Ru	^{107}Ru	^{108}Ru	^{109}Ru	^{110}Ru
^{112}Ru	^{114}Ru	^{94}Rh	^{94}Rh*	^{95}Rh	^{95}Rh*
^{96}Rh	^{96}Rh*	^{97}Rh	^{97}Rh*	^{98}Rh	^{98}Rh*
^{99}Rh	^{99}Rh*	^{100}Rh	^{100}Rh*	^{101}Rh	^{101}Rh*
^{102}Rh	^{102}Rh*	^{103}Rh	^{103}Rh*	^{104}Rh	^{104}Rh*
^{105}Rh	^{105}Rh*	^{106}Rh	^{106}Rh*	^{107}Rh	^{108}Rh
^{108}Rh*	^{109}Rh	^{110}Rh	^{110}Rh*	^{111}Rh	^{112}Rh
^{112}Rh*	^{113}Rh	^{114}Rh	^{114}Rh*	^{115}Rh	^{116}Rh
^{116}Rh*	^{117}Rh	^{94}Pd	^{95}Pd	^{95}Pd*	^{96}Pd
^{97}Pd	^{98}Pd	^{99}Pd	^{100}Pd	^{101}Pd	^{102}Pd
^{103}Pd	^{104}Pd	^{105}Pd	^{106}Pd	^{107}Pd*	^{108}Pd
^{109}Pd	^{109}Pd*	^{110}Pd	^{111}Pd	^{111}Pd*	^{112}Pd
^{113}Pd	^{114}Pd	^{115}Pd	^{115}Pd*	^{116}Pd	^{117}Pd
^{117}Pd*	^{118}Pd	^{120}Pd	^{96}Ag	^{97}Ag	^{98}Ag
^{99}Ag	^{99}Ag*	^{100}Ag	^{100}Ag*	^{101}Ag	^{101}Ag*
^{102}Ag	^{102}Ag*	^{103}Ag	^{103}Ag*	^{104}Ag	^{104}Ag*
^{105}Ag	^{105}Ag*	^{106}Ag	^{106}Ag*	^{107}Ag	^{107}Ag*
^{108}Ag	^{109}Ag	^{109}Ag*	^{110}Ag	^{110}Ag*	^{111}Ag
^{111}Ag*	^{112}Ag	^{113}Ag	^{113}Ag*	^{114}Ag	^{115}Ag
^{115}Ag*	^{116}Ag	^{116}Ag*	^{117}Ag	^{117}Ag*	^{118}Ag
^{118}Ag*	^{119}Ag	^{119}Ag*	^{120}Ag	^{120}Ag*	^{121}Ag
^{122}Ag	^{123}Ag	^{125}Ag	^{98}Cd	^{99}Cd	^{100}Cd
^{101}Cd	^{102}Cd	^{103}Cd	^{104}Cd	^{105}Cd	^{106}Cd
^{107}Cd	^{108}Cd	^{109}Cd	^{110}Cd	^{111}Cd	^{111}Cd*
^{112}Cd	^{113}Cd	^{114}Cd	^{115}Cd	^{115}Cd*	^{116}Cd
^{117}Cd	^{117}Cd*	^{118}Cd	^{119}Cd	^{119}Cd*	^{120}Cd

Table C.11: Nuclides Calculated via Interpolation (Part 6)

^{121}Cd	^{121}Cd*	^{122}Cd	^{123}Cd	^{123}Cd*	^{124}Cd
^{125}Cd	^{125}Cd*	^{126}Cd	^{127}Cd	^{128}Cd	^{99}In
^{100}In	^{102}In	^{103}In	^{104}In	^{104}In*	^{105}In
^{105}In*	^{106}In	^{106}In*	^{107}In	^{107}In*	^{108}In
^{108}In*	^{109}In	^{109}In*	^{110}In	^{110}In*	^{111}In
^{111}In*	^{112}In	^{112}In*	^{113}In	^{113}In*	^{114}In
^{114}In*	^{115}In	^{115}In*	^{116}In	^{116}In*	^{117}In
^{117}In*	^{118}In	^{118}In*	^{119}In	^{119}In*	^{120}In
^{120}In*	^{121}In	^{121}In*	^{122}In	^{122}In*	^{123}In
^{123}In*	^{124}In	^{124}In*	^{125}In	^{125}In*	^{126}In
^{126}In*	^{127}In	^{127}In*	^{128}In	^{128}In*	^{129}In
^{129}In*	^{130}In	^{130}In*	^{131}In	^{131}In*	^{132}In
^{133}In	^{100}Sn	^{102}Sn	^{103}Sn	^{104}Sn	^{105}Sn
^{106}Sn	^{107}Sn	^{108}Sn	^{109}Sn	^{110}Sn	^{111}Sn
^{111}Sn*	^{112}Sn	^{113}Sn	^{113}Sn*	^{114}Sn	^{115}Sn
^{115}Sn*	^{116}Sn	^{117}Sn	^{118}Sn	^{119}Sn	^{120}Sn
^{121}Sn	^{122}Sn	^{123}Sn*	^{124}Sn	^{124}Sn*	^{127}Sn
^{127}Sn*	^{128}Sn	^{128}Sn*	^{129}Sn	^{129}Sn*	^{130}Sn
^{130}Sn*	^{131}Sn	^{131}Sn*	^{132}Sn	^{132}Sn*	^{133}Sn
^{134}Sn	^{104}Sb	^{106}Sb	^{107}Sb	^{108}Sb	^{109}Sb
^{110}Sb	^{111}Sb	^{112}Sb	^{113}Sb	^{114}Sb	^{115}Sb
^{115}Sb*	^{116}Sb	^{116}Sb*	^{117}Sb	^{117}Sb*	^{118}Sb
^{118}Sb*	^{119}Sb	^{120}Sb	^{120}Sb*	^{121}Sb	^{122}Sb
^{122}Sb*	^{123}Sb	^{126}Sb*	^{127}Sb	^{128}Sb	^{128}Sb*
^{129}Sb	^{129}Sb*	^{130}Sb	^{130}Sb*	^{131}Sb	^{132}Sb
^{132}Sb*	^{133}Sb	^{134}Sb	^{134}Sb*	^{135}Sb	^{136}Sb
^{106}Te	^{107}Te	^{108}Te	^{109}Te	^{110}Te	^{111}Te
^{112}Te	^{113}Te	^{114}Te	^{115}Te	^{115}Te*	^{116}Te
^{117}Te	^{117}Te*	^{118}Te	^{119}Te	^{119}Te*	^{120}Te
^{121}Te	^{121}Te*	^{122}Te	^{123}Te	^{123}Te*	^{124}Te
^{125}Te	^{126}Te	^{127}Te	^{127}Te*	^{128}Te	^{129}Te
^{129}Te*	^{130}Te	^{131}Te	^{131}Te*	^{132}Te	^{133}Te
^{133}Te*	^{134}Te	^{134}Te*	^{135}Te	^{135}Te*	^{136}Te
^{137}Te	^{138}Te	^{108}I	^{110}I	^{111}I	^{112}I
^{113}I	^{114}I	^{114}I*	^{115}I	^{116}I	^{117}I

Table C.12: Nuclides Calculated via Interpolation (Part 7)

^{118}I	^{118}I*	^{119}I	^{120}I	^{120}I*	^{121}I
^{122}I	^{123}I	^{124}I	^{125}I	^{126}I	^{127}I
^{128}I	^{130}I	^{130}I*	^{131}I	^{132}I	^{132}I*
^{133}I	^{133}I*	^{134}I	^{134}I*	^{135}I	^{136}I
^{136}I*	^{137}I	^{138}I	^{139}I	^{140}I	^{142}I
^{110}Xe	^{112}Xe	^{113}Xe	^{114}Xe	^{115}Xe	^{116}Xe
^{117}Xe	^{118}Xe	^{119}Xe	^{120}Xe	^{121}Xe	^{122}Xe
^{123}Xe	^{124}Xe	^{125}Xe	^{125}Xe*	^{126}Xe	^{127}Xe
^{127}Xe*	^{128}Xe	^{129}Xe	^{129}Xe*	^{130}Xe	^{131}Xe
^{131}Xe*	^{132}Xe	^{132}Xe*	^{133}Xe	^{133}Xe*	^{134}Xe
^{134}Xe*	^{135}Xe	^{135}Xe*	^{136}Xe	^{137}Xe	^{138}Xe
^{139}Xe	^{140}Xe	^{141}Xe	^{142}Xe	^{143}Xe	^{144}Xe
^{145}Xe	^{113}Cs	^{114}Cs	^{116}Cs	^{116}Cs*	^{117}Cs
^{117}Cs*	^{118}Cs	^{118}Cs*	^{119}Cs	^{119}Cs*	^{120}Cs
^{120}Cs*	^{121}Cs	^{121}Cs*	^{122}Cs	^{122}Cs*	^{123}Cs
^{123}Cs*	^{124}Cs	^{124}Cs*	^{125}Cs	^{126}Cs	^{127}Cs
^{128}Cs	^{129}Cs	^{130}Cs	^{130}Cs*	^{131}Cs	^{132}Cs
^{133}Cs	^{135}Cs*	^{136}Cs*	^{138}Cs	^{138}Cs*	^{139}Cs
^{144}Cs*	^{146}Cs	^{114}Ba	^{116}Ba	^{117}Ba	^{118}Ba
^{119}Ba	^{120}Ba	^{121}Ba	^{122}Ba	^{123}Ba	^{124}Ba
^{125}Ba	^{126}Ba	^{127}Ba	^{127}Ba*	^{128}Ba	^{129}Ba
^{129}Ba*	^{130}Ba	^{130}Ba*	^{131}Ba	^{131}Ba*	^{132}Ba
^{133}Ba*	^{134}Ba	^{134}Ba*	^{135}Ba	^{135}Ba*	^{136}Ba
^{136}Ba*	^{137}Ba	^{137}Ba*	^{138}Ba	^{139}Ba	^{142}Ba
^{143}Ba	^{144}Ba	^{145}Ba	^{146}Ba	^{147}Ba	^{148}Ba
^{150}Ba	^{121}La	^{123}La	^{124}La	^{125}La	^{126}La
^{127}La	^{127}La*	^{128}La	^{129}La	^{129}La*	^{130}La
^{131}La	^{131}La*	^{132}La	^{132}La*	^{133}La	^{134}La
^{135}La	^{136}La	^{137}La	^{138}La	^{139}La	^{140}La
^{141}La	^{142}La	^{143}La	^{144}La	^{145}La	^{146}La
^{146}La*	^{147}La	^{148}La	^{150}La	^{123}Ce	^{124}Ce
^{125}Ce	^{126}Ce	^{127}Ce	^{128}Ce	^{129}Ce	^{130}Ce
^{131}Ce	^{131}Ce*	^{132}Ce	^{132}Ce*	^{133}Ce	^{133}Ce*
^{134}Ce	^{135}Ce	^{135}Ce*	^{136}Ce	^{137}Ce	^{137}Ce*
^{138}Ce	^{138}Ce*	^{139}Ce	^{139}Ce*	^{140}Ce	^{141}Ce

Table C.13: Nuclides Calculated via Interpolation (Part 8)

^{142}Ce	^{143}Ce	^{144}Ce	^{145}Ce	^{146}Ce	^{147}Ce
^{148}Ce	^{149}Ce	^{150}Ce	^{152}Ce	^{126}Pr	^{128}Pr
^{129}Pr	^{130}Pr	^{131}Pr	^{131}Pr*	^{132}Pr	^{133}Pr
^{134}Pr	^{134}Pr*	^{135}Pr	^{136}Pr	^{137}Pr	^{138}Pr
^{138}Pr*	^{139}Pr	^{140}Pr	^{141}Pr	^{142}Pr	^{142}Pr*
^{143}Pr	^{144}Pr	^{144}Pr*	^{145}Pr	^{146}Pr	^{147}Pr
^{148}Pr	^{148}Pr*	^{149}Pr	^{150}Pr	^{151}Pr	^{152}Pr
^{154}Pr	^{129}Nd	^{130}Nd	^{131}Nd	^{132}Nd	^{133}Nd
^{134}Nd	^{134}Nd*	^{135}Nd	^{135}Nd*	^{136}Nd	^{137}Nd
^{137}Nd*	^{138}Nd	^{139}Nd	^{139}Nd*	^{140}Nd	^{140}Nd*
^{141}Nd	^{141}Nd*	^{142}Nd	^{143}Nd	^{144}Nd	^{145}Nd
^{146}Nd	^{147}Nd	^{148}Nd	^{149}Nd	^{150}Nd	^{151}Nd
^{152}Nd	^{153}Nd	^{154}Nd	^{156}Nd	^{132}Pm	^{133}Pm
^{134}Pm	^{134}Pm*	^{135}Pm	^{135}Pm*	^{136}Pm	^{136}Pm*
^{137}Pm	^{138}Pm	^{138}Pm*	^{139}Pm	^{139}Pm*	^{140}Pm
^{140}Pm*	^{141}Pm	^{142}Pm	^{143}Pm	^{144}Pm	^{145}Pm
^{148}Pm	^{148}Pm*	^{149}Pm	^{150}Pm	^{151}Pm	^{152}Pm
^{152}Pm*	^{153}Pm	^{154}Pm	^{154}Pm*	^{155}Pm	^{156}Pm
^{157}Pm	^{158}Pm	^{134}Sm	^{135}Sm	^{136}Sm	^{137}Sm
^{138}Sm	^{139}Sm	^{139}Sm*	^{140}Sm	^{141}Sm	^{141}Sm*
^{142}Sm	^{143}Sm	^{143}Sm*	^{144}Sm	^{146}Sm	^{147}Sm
^{149}Sm	^{150}Sm	^{152}Sm	^{153}Sm	^{153}Sm*	^{154}Sm
^{156}Sm	^{157}Sm	^{158}Sm	^{159}Sm	^{160}Sm	^{136}Eu
^{136}Eu*	^{137}Eu	^{138}Eu	^{139}Eu	^{140}Eu	^{140}Eu*
^{141}Eu	^{141}Eu*	^{142}Eu	^{142}Eu*	^{143}Eu	^{144}Eu
^{145}Eu	^{146}Eu	^{146}Eu*	^{147}Eu	^{148}Eu	^{150}Eu*
^{151}Eu	^{152}Eu*	^{153}Eu	^{154}Eu*	^{157}Eu	^{158}Eu
^{159}Eu	^{160}Eu	^{139}Gd	^{140}Gd	^{141}Gd	^{141}Gd*
^{142}Gd	^{143}Gd	^{143}Gd*	^{144}Gd	^{145}Gd	^{145}Gd*
^{146}Gd	^{147}Gd	^{148}Gd	^{149}Gd	^{150}Gd	^{151}Gd
^{152}Gd	^{153}Gd	^{153}Gd*	^{154}Gd	^{155}Gd	^{155}Gd*
^{156}Gd	^{157}Gd	^{157}Gd*	^{158}Gd	^{159}Gd	^{159}Gd*
^{160}Gd	^{161}Gd	^{162}Gd	^{163}Gd	^{164}Gd	^{140}Tb
^{141}Tb	^{142}Tb	^{142}Tb*	^{143}Tb	^{144}Tb	^{144}Tb*
^{145}Tb	^{145}Tb*	^{146}Tb	^{146}Tb*	^{147}Tb	^{147}Tb*

Table C.14: Nuclides Calculated via Interpolation (Part 9)

^{148}Tb	^{148}Tb*	^{149}Tb	^{149}Tb*	^{150}Tb	^{150}Tb*
^{151}Tb	^{151}Tb*	^{152}Tb	^{152}Tb*	^{153}Tb	^{153}Tb*
^{154}Tb	^{154}Tb*	^{155}Tb	^{156}Tb	^{156}Tb*	^{157}Tb
^{158}Tb	^{158}Tb*	^{159}Tb	^{160}Tb	^{161}Tb	^{162}Tb
^{163}Tb	^{164}Tb	^{165}Tb	^{141}Dy	^{142}Dy	^{144}Dy
^{145}Dy	^{145}Dy*	^{146}Dy	^{146}Dy*	^{147}Dy	^{147}Dy*
^{148}Dy	^{149}Dy	^{149}Dy*	^{150}Dy	^{151}Dy	^{152}Dy
^{153}Dy	^{154}Dy	^{155}Dy	^{155}Dy*	^{156}Dy	^{157}Dy
^{157}Dy*	^{158}Dy	^{159}Dy	^{159}Dy*	^{160}Dy	^{161}Dy
^{162}Dy	^{163}Dy	^{164}Dy	^{165}Dy	^{165}Dy*	^{166}Dy
^{167}Dy	^{168}Dy	^{169}Dy	^{145}Ho	^{146}Ho	^{147}Ho
^{148}Ho	^{148}Ho*	^{149}Ho	^{149}Ho*	^{150}Ho	^{150}Ho*
^{151}Ho	^{151}Ho*	^{152}Ho	^{152}Ho*	^{153}Ho	^{153}Ho*
^{154}Ho	^{154}Ho*	^{155}Ho	^{156}Ho	^{156}Ho*	^{157}Ho
^{158}Ho	^{158}Ho*	^{159}Ho	^{159}Ho*	^{160}Ho	^{160}Ho*
^{161}Ho	^{161}Ho*	^{162}Ho	^{162}Ho*	^{163}Ho	^{163}Ho*
^{164}Ho	^{164}Ho*	^{165}Ho	^{166}Ho	^{166}Ho*	^{167}Ho
^{168}Ho	^{168}Ho*	^{169}Ho	^{170}Ho	^{170}Ho*	^{171}Ho
^{145}Er	^{146}Er	^{147}Er	^{147}Er*	^{148}Er	^{149}Er
^{149}Er*	^{150}Er	^{151}Er	^{151}Er*	^{152}Er	^{153}Er
^{154}Er	^{154}Er*	^{155}Er	^{156}Er	^{157}Er	^{157}Er*
^{158}Er	^{159}Er	^{160}Er	^{161}Er	^{162}Er	^{163}Er
^{164}Er	^{165}Er	^{166}Er	^{167}Er	^{167}Er*	^{168}Er
^{169}Er	^{170}Er	^{171}Er	^{172}Er	^{173}Er	^{174}Er
^{175}Er	^{147}Tm	^{147}Tm*	^{148}Tm	^{149}Tm	^{150}Tm
^{150}Tm*	^{151}Tm	^{151}Tm*	^{152}Tm	^{152}Tm*	^{153}Tm
^{153}Tm*	^{154}Tm	^{154}Tm*	^{155}Tm	^{155}Tm*	^{156}Tm
^{156}Tm*	^{157}Tm	^{158}Tm	^{159}Tm	^{160}Tm	^{160}Tm*
^{161}Tm	^{162}Tm	^{162}Tm*	^{163}Tm	^{164}Tm	^{164}Tm*
^{165}Tm	^{166}Tm	^{167}Tm	^{168}Tm	^{169}Tm	^{170}Tm
^{171}Tm	^{172}Tm	^{173}Tm	^{174}Tm	^{175}Tm	^{176}Tm
^{177}Tm	^{149}Yb	^{150}Yb	^{151}Yb	^{151}Yb*	^{152}Yb
^{152}Yb*	^{153}Yb	^{154}Yb	^{155}Yb	^{156}Yb	^{157}Yb
^{158}Yb	^{159}Yb	^{160}Yb	^{161}Yb	^{162}Yb	^{163}Yb
^{164}Yb	^{165}Yb	^{166}Yb	^{167}Yb	^{168}Yb	^{169}Yb

237

Table C.15: Nuclides Calculated via Interpolation (Part 10)

$^{169}\text{Yb}^*$	^{170}Yb	^{171}Yb	^{172}Yb	^{173}Yb	^{174}Yb
$^{174}\text{Yb}^*$	^{175}Yb	^{176}Yb	$^{176}\text{Yb}^*$	^{177}Yb	$^{177}\text{Yb}^*$
^{178}Yb	^{179}Yb	^{150}Lu	^{151}Lu	^{152}Lu	^{153}Lu
^{154}Lu	$^{154}\text{Lu}^*$	^{155}Lu	$^{155}\text{Lu}^*$	^{156}Lu	^{157}Lu
$^{157}\text{Lu}^*$	^{158}Lu	^{159}Lu	^{160}Lu	^{161}Lu	$^{161}\text{Lu}^*$
^{162}Lu	$^{162}\text{Lu}^*$	^{163}Lu	^{164}Lu	^{165}Lu	^{166}Lu
$^{166}\text{Lu}^*$	^{167}Lu	^{168}Lu	$^{168}\text{Lu}^*$	^{169}Lu	$^{169}\text{Lu}^*$
^{170}Lu	$^{170}\text{Lu}^*$	^{171}Lu	$^{171}\text{Lu}^*$	^{172}Lu	$^{172}\text{Lu}^*$
^{173}Lu	^{174}Lu	$^{174}\text{Lu}^*$	^{175}Lu	^{176}Lu	$^{176}\text{Lu}^*$
^{177}Lu	$^{177}\text{Lu}^*$	^{178}Lu	$^{178}\text{Lu}^*$	^{179}Lu	$^{179}\text{Lu}^*$
^{180}Lu	^{181}Lu	^{154}Hf	$^{154}\text{Hf}^*$	^{155}Hf	^{156}Hf
$^{156}\text{Hf}^*$	^{157}Hf	^{158}Hf	^{159}Hf	^{160}Hf	^{161}Hf
^{162}Hf	^{164}Hf	^{165}Hf	^{166}Hf	^{167}Hf	^{168}Hf
^{169}Hf	^{170}Hf	^{171}Hf	^{172}Hf	^{173}Hf	^{174}Hf
^{175}Hf	^{176}Hf	^{177}Hf	$^{177}\text{Hf}^*$	^{178}Hf	$^{178}\text{Hf}^*$
^{179}Hf	$^{179}\text{Hf}^*$	^{180}Hf	$^{180}\text{Hf}^*$	^{181}Hf	^{182}Hf
$^{182}\text{Hf}^*$	^{183}Hf	^{184}Hf	$^{184}\text{Hf}^*$	^{156}Ta	^{157}Ta
$^{157}\text{Ta}^*$	^{158}Ta	^{159}Ta	^{160}Ta	^{161}Ta	^{162}Ta
^{163}Ta	^{164}Ta	^{165}Ta	^{166}Ta	^{168}Ta	^{169}Ta
^{170}Ta	^{171}Ta	^{172}Ta	^{173}Ta	^{174}Ta	^{175}Ta
^{176}Ta	$^{176}\text{Ta}^*$	^{177}Ta	^{178}Ta	$^{178}\text{Ta}^*$	^{179}Ta
$^{179}\text{Ta}^*$	^{180}Ta	^{181}Ta	^{182}Ta	$^{182}\text{Ta}^*$	^{183}Ta
^{184}Ta	^{185}Ta	^{186}Ta	^{158}W	^{159}W	^{160}W
^{161}W	^{162}W	^{163}W	^{164}W	^{165}W	^{166}W
^{167}W	^{168}W	^{169}W	^{170}W	^{171}W	^{172}W
^{173}W	^{174}W	^{175}W	^{176}W	^{177}W	^{178}W
^{179}W	$^{179}\text{W}^*$	^{180}W	$^{180}\text{W}^*$	^{181}W	^{182}W
^{183}W	$^{183}\text{W}^*$	^{184}W	^{185}W	$^{185}\text{W}^*$	^{186}W
^{187}W	^{188}W	^{189}W	^{190}W	^{160}Re	^{162}Re
^{163}Re	^{164}Re	^{165}Re	^{166}Re	^{167}Re	^{168}Re
^{169}Re	^{170}Re	^{171}Re	^{172}Re	$^{172}\text{Re}^*$	^{173}Re
^{174}Re	^{175}Re	^{176}Re	^{177}Re	^{178}Re	^{179}Re
^{180}Re	^{181}Re	^{182}Re	$^{182}\text{Re}^*$	^{183}Re	$^{183}\text{Re}^*$
^{184}Re	$^{184}\text{Re}^*$	^{185}Re	^{186}Re	$^{186}\text{Re}^*$	^{187}Re
^{188}Re	$^{188}\text{Re}^*$	^{189}Re	^{190}Re	$^{190}\text{Re}^*$	^{191}Re

Table C.16: Nuclides Calculated via Interpolation (Part 11)

^{162}Os	^{164}Os	^{165}Os	^{166}Os	^{167}Os	^{168}Os
^{169}Os	^{170}Os	^{171}Os	^{172}Os	^{173}Os	^{174}Os
^{175}Os	^{176}Os	^{177}Os	^{178}Os	^{179}Os	^{180}Os
^{181}Os	^{181}Os*	^{182}Os	^{183}Os	^{183}Os*	^{184}Os
^{185}Os	^{186}Os	^{187}Os	^{188}Os	^{189}Os	^{189}Os*
^{190}Os	^{190}Os*	^{191}Os	^{191}Os*	^{192}Os	^{192}Os*
^{193}Os	^{194}Os	^{196}Os	^{167}Ir	^{169}Ir	^{170}Ir
^{171}Ir	^{172}Ir	^{172}Ir*	^{173}Ir	^{173}Ir*	^{174}Ir
^{174}Ir*	^{175}Ir	^{176}Ir	^{177}Ir	^{178}Ir	^{179}Ir
^{180}Ir	^{181}Ir	^{182}Ir	^{183}Ir	^{184}Ir	^{185}Ir
^{186}Ir	^{186}Ir*	^{187}Ir	^{187}Ir*	^{188}Ir	^{189}Ir
^{189}Ir*	^{190}Ir	^{190}Ir*	^{191}Ir	^{191}Ir*	^{192}Ir
^{192}Ir*	^{193}Ir	^{193}Ir*	^{194}Ir	^{194}Ir*	^{195}Ir
^{195}Ir*	^{196}Ir	^{196}Ir*	^{197}Ir	^{197}Ir*	^{168}Pt
^{170}Pt	^{171}Pt	^{172}Pt	^{173}Pt	^{174}Pt	^{175}Pt
^{176}Pt	^{177}Pt	^{178}Pt	^{179}Pt	^{180}Pt	^{181}Pt
^{182}Pt	^{183}Pt	^{183}Pt*	^{184}Pt	^{184}Pt*	^{185}Pt
^{185}Pt*	^{186}Pt	^{187}Pt	^{188}Pt	^{189}Pt	^{190}Pt
^{191}Pt	^{192}Pt	^{193}Pt	^{193}Pt*	^{194}Pt	^{195}Pt
^{195}Pt*	^{196}Pt	^{197}Pt	^{197}Pt*	^{198}Pt	^{199}Pt
^{199}Pt*	^{200}Pt	^{201}Pt	^{202}Pt	^{171}Au	^{171}Au*
^{172}Au	^{173}Au	^{175}Au	^{176}Au	^{177}Au	^{178}Au
^{179}Au	^{180}Au	^{181}Au	^{182}Au	^{183}Au	^{184}Au
^{184}Au*	^{185}Au	^{185}Au*	^{186}Au	^{186}Au*	^{187}Au
^{187}Au*	^{188}Au	^{189}Au	^{189}Au*	^{190}Au	^{191}Au
^{191}Au*	^{192}Au	^{193}Au	^{193}Au*	^{194}Au	^{194}Au*
^{195}Au	^{195}Au*	^{196}Au	^{196}Au*	^{197}Au	^{197}Au*
^{198}Au	^{198}Au*	^{199}Au	^{199}Au*	^{200}Au	^{200}Au*
^{201}Au	^{202}Au	^{203}Au	^{204}Au	^{205}Au	^{176}Hg
^{177}Hg	^{178}Hg	^{179}Hg	^{180}Hg	^{181}Hg	^{182}Hg
^{183}Hg	^{184}Hg	^{185}Hg	^{185}Hg*	^{186}Hg	^{187}Hg
^{187}Hg*	^{188}Hg	^{189}Hg	^{189}Hg*	^{190}Hg	^{191}Hg
^{191}Hg*	^{192}Hg	^{193}Hg	^{193}Hg*	^{194}Hg	^{195}Hg
^{195}Hg*	^{196}Hg	^{197}Hg	^{197}Hg*	^{198}Hg	^{199}Hg
^{199}Hg*	^{200}Hg	^{201}Hg	^{202}Hg	^{203}Hg	^{204}Hg

Table C.17: Nuclides Calculated via Interpolation (Part 12)

^{205}Hg	^{205}Hg*	^{206}Hg	^{207}Hg	^{208}Hg	^{177}Tl
^{179}Tl*	^{180}Tl	^{181}Tl	^{182}Tl	^{183}Tl	^{183}Tl*
^{184}Tl	^{185}Tl	^{185}Tl*	^{186}Tl	^{186}Tl*	^{187}Tl
^{187}Tl*	^{188}Tl	^{188}Tl*	^{189}Tl	^{189}Tl*	^{190}Tl
^{190}Tl*	^{191}Tl	^{191}Tl*	^{192}Tl	^{192}Tl*	^{193}Tl
^{193}Tl*	^{194}Tl	^{194}Tl*	^{195}Tl	^{195}Tl*	^{196}Tl
^{196}Tl*	^{197}Tl	^{197}Tl*	^{198}Tl	^{198}Tl*	^{199}Tl
^{199}Tl*	^{200}Tl	^{200}Tl*	^{201}Tl	^{201}Tl*	^{202}Tl
^{203}Tl	^{204}Tl	^{205}Tl	^{206}Tl	^{206}Tl*	^{207}Tl
^{207}Tl*	^{208}Tl	^{209}Tl	^{210}Tl	^{180}Pb	^{181}Pb
^{182}Pb	^{183}Pb	^{184}Pb	^{186}Pb	^{187}Pb	^{187}Pb*
^{188}Pb	^{189}Pb	^{190}Pb	^{191}Pb	^{191}Pb*	^{192}Pb
^{193}Pb	^{193}Pb*	^{194}Pb	^{195}Pb	^{195}Pb*	^{196}Pb
^{197}Pb	^{197}Pb*	^{198}Pb	^{199}Pb	^{199}Pb*	^{200}Pb
^{201}Pb	^{201}Pb*	^{202}Pb	^{202}Pb*	^{203}Pb	^{203}Pb*
^{204}Pb	^{204}Pb*	^{205}Pb	^{205}Pb*	^{207}Pb*	^{209}Pb
^{211}Pb	^{212}Pb	^{213}Pb	^{214}Pb	^{185}Bi	^{186}Bi
^{186}Bi*	^{187}Bi	^{187}Bi*	^{189}Bi	^{189}Bi*	^{190}Bi
^{190}Bi*	^{191}Bi	^{191}Bi*	^{192}Bi	^{192}Bi*	^{193}Bi
^{193}Bi*	^{194}Bi	^{194}Bi*	^{195}Bi	^{195}Bi*	^{196}Bi
^{197}Bi	^{197}Bi*	^{198}Bi	^{198}Bi*	^{199}Bi	^{199}Bi*
^{200}Bi	^{200}Bi*	^{201}Bi	^{201}Bi*	^{202}Bi	^{203}Bi
^{203}Bi*	^{204}Bi	^{204}Bi*	^{205}Bi	^{206}Bi	^{207}Bi
^{207}Bi*	^{208}Bi	^{208}Bi*	^{210}Bi	^{210}Bi*	^{211}Bi
^{212}Bi	^{212}Bi*	^{213}Bi	^{214}Bi	^{216}Bi	^{190}Po
^{192}Po	^{193}Po	^{193}Po*	^{194}Po	^{195}Po	^{195}Po*
^{196}Po	^{197}Po	^{197}Po*	^{198}Po	^{199}Po	^{199}Po*
^{200}Po	^{201}Po	^{201}Po*	^{202}Po	^{203}Po	^{203}Po*
^{204}Po	^{205}Po	^{206}Po	^{207}Po	^{207}Po*	^{208}Po
^{209}Po	^{210}Po	^{211}Po	^{211}Po*	^{212}Po	^{212}Po*
^{213}Po	^{214}Po	^{214}Po*	^{215}Po	^{216}Po	^{217}Po
^{218}Po	^{196}At	^{197}At	^{197}At*	^{198}At	^{198}At*
^{199}At	^{200}At	^{200}At*	^{201}At	^{202}At	^{202}At*
^{203}At	^{204}At	^{204}At*	^{205}At	^{206}At	^{207}At
^{208}At	^{209}At	^{210}At	^{211}At	^{212}At	^{212}At*

Table C.18: Nuclides Calculated via Interpolation (Part 13)

^{213}At	^{214}At	^{215}At	^{216}At	^{216}At*	^{217}At
^{218}At	^{219}At	^{220}At	^{196}Rn	^{197}Rn	^{197}Rn*
^{198}Rn	^{199}Rn	^{199}Rn*	^{200}Rn	^{201}Rn	^{201}Rn*
^{202}Rn	^{203}Rn	^{203}Rn*	^{204}Rn	^{205}Rn	^{206}Rn
^{207}Rn	^{207}Rn*	^{208}Rn	^{209}Rn	^{210}Rn	^{211}Rn
^{212}Rn	^{213}Rn	^{214}Rn	^{214}Rn*	^{215}Rn	^{216}Rn
^{217}Rn	^{218}Rn	^{219}Rn	^{220}Rn	^{221}Rn	^{222}Rn
^{224}Rn	^{226}Rn	^{227}Rn	^{228}Rn	^{200}Fr	^{200}Fr*
^{201}Fr	^{202}Fr	^{202}Fr*	^{203}Fr	^{204}Fr	^{204}Fr*
^{205}Fr	^{206}Fr	^{206}Fr*	^{207}Fr	^{208}Fr	^{209}Fr
^{210}Fr	^{211}Fr	^{212}Fr	^{213}Fr	^{214}Fr	^{214}Fr*
^{215}Fr	^{216}Fr	^{216}Fr*	^{217}Fr	^{218}Fr	^{218}Fr*
^{219}Fr	^{220}Fr	^{221}Fr	^{222}Fr	^{223}Fr	^{224}Fr
^{225}Fr	^{226}Fr	^{227}Fr	^{228}Fr	^{203}Ra	^{203}Ra*
^{204}Ra	^{206}Ra	^{207}Ra	^{207}Ra*	^{208}Ra	^{209}Ra
^{210}Ra	^{211}Ra	^{212}Ra	^{213}Ra	^{213}Ra*	^{214}Ra
^{215}Ra	^{216}Ra	^{216}Ra*	^{217}Ra	^{218}Ra	^{219}Ra
^{220}Ra	^{221}Ra	^{222}Ra	^{223}Ra	^{224}Ra	^{225}Ra
^{227}Ra	^{229}Ra	^{230}Ra	^{233}Ra	^{207}Ac	^{208}Ac
^{208}Ac*	^{209}Ac	^{210}Ac	^{211}Ac	^{212}Ac	^{213}Ac
^{214}Ac	^{215}Ac	^{216}Ac	^{216}Ac*	^{217}Ac	^{217}Ac*
^{218}Ac	^{219}Ac	^{220}Ac	^{221}Ac	^{222}Ac	^{222}Ac*
^{223}Ac	^{224}Ac	^{225}Ac	^{226}Ac	^{228}Ac	^{229}Ac
^{230}Ac	^{231}Ac	^{232}Ac	^{233}Ac	^{210}Th	^{212}Th
^{214}Th	^{215}Th	^{216}Th	^{216}Th*	^{217}Th	^{218}Th
^{219}Th	^{220}Th	^{221}Th	^{222}Th	^{223}Th	^{224}Th
^{225}Th	^{226}Th	^{227}Th	^{231}Th	^{233}Th	^{234}Th
^{235}Th	^{237}Th	^{213}Pa	^{216}Pa	^{219}Pa	^{221}Pa
^{224}Pa	^{226}Pa	^{227}Pa	^{228}Pa	^{229}Pa	^{230}Pa
^{232}Pa	^{233}Pa	^{234}Pa	^{234}Pa*	^{235}Pa	^{236}Pa
^{237}Pa	^{238}Pa	^{239}Pa	^{218}U	^{219}U	^{222}U
^{223}U	^{224}U	^{225}U	^{226}U	^{227}U	^{228}U
^{229}U	^{231}U*	^{236}U*	^{240}U	^{225}Np	^{228}Np
^{229}Np	^{230}Np	^{231}Np	^{232}Np	^{233}Np	^{234}Np
^{237}Np*	^{242}Np	^{242}Np*	^{243}Np	^{244}Np	^{228}Pu

Table C.19: Nuclides Calculated via Interpolation (Part 14)

^{229}Pu	^{230}Pu	^{232}Pu	^{233}Pu	^{234}Pu	^{235}Pu
^{235}Pu*	^{238}Pu*	^{232}Am	^{234}Am	^{237}Am	^{237}Am*
^{238}Am	^{240}Am*	^{246}Am*	^{247}Am	^{235}Cm	^{236}Cm
^{237}Cm	^{238}Cm	^{239}Cm	^{240}Cm	^{240}Cm*	^{242}Cm*
^{252}Cm	^{237}Bk	^{238}Bk	^{239}Bk	^{240}Bk	^{241}Bk
^{242}Bk	^{243}Bk	^{244}Bk	^{244}Bk*	^{245}Bk	^{246}Bk
^{247}Bk	^{248}Bk	^{248}Bk*	^{250}Bk	^{251}Bk	^{239}Cf
^{240}Cf	^{241}Cf	^{242}Cf	^{243}Cf	^{244}Cf	^{245}Cf
^{246}Cf	^{246}Cf*	^{247}Cf	^{248}Cf	^{253}Cf	^{254}Cf
^{255}Cf	^{256}Cf	^{241}Es	^{242}Es	^{243}Es	^{244}Es
^{245}Es	^{246}Es	^{247}Es	^{248}Es	^{249}Es	^{250}Es
^{250}Es*	^{251}Es	^{252}Es	^{253}Es	^{254}Es	^{254}Es*
^{255}Es	^{256}Es	^{256}Es*	^{246}Fm	^{247}Fm	^{248}Fm
^{249}Fm	^{250}Fm	^{250}Fm*	^{251}Fm	^{252}Fm	^{253}Fm
^{254}Fm	^{255}Fm	^{256}Fm	^{257}Fm	^{258}Fm	^{245}Md
^{246}Md	^{248}Md	^{249}Md	^{250}Md	^{251}Md	^{253}Md
^{254}Md	^{255}Md	^{256}Md	^{257}Md	^{258}Md	^{258}Md*
^{259}Md	^{260}Md	^{251}No	^{252}No	^{253}No	^{254}No
^{254}No*	^{255}No	^{256}No	^{257}No	^{258}No	^{259}No
^{260}No	^{262}No	^{253}Lr	^{254}Lr	^{255}Lr	^{256}Lr
^{257}Lr	^{258}Lr	^{259}Lr	^{260}Lr	^{261}Lr	^{262}Lr
^{254}Rf	^{255}Rf	^{256}Rf	^{257}Rf	^{258}Rf	^{259}Rf
^{260}Rf	^{261}Rf	^{262}Rf	^{263}Rf	^{257}Db	^{258}Db
^{260}Db	^{262}Db	^{263}Db	^{258}Sg	^{259}Sg	^{260}Sg
^{263}Sg	^{265}Sg	^{262}Bh	^{262}Bh*	^{264}Bh	^{264}Hs

Bibliography

[1] Report to Congress Advanced Fuel Cycle Initiative : Status Report for FY 2005. Technical Report February, 2006.

[2] R. Ahlswede and I. Csiszar. Common randomness in information theory and cryptography. I. Secret sharing. *IEEE Transactions on Information Theory*, 39(4):1121–1132, July 1993.

[3] J.G. Barratt and E.A. Schneider. Monte Carlo Uncertainty Analysis of a Transmuting Fuel Cycle. *TRANSACTIONS-AMERICAN NUCLEAR SOCIETY*, 90:249–250, 2004.

[4] Ludwig Boltzmann. Weitere studien über das wärmegleichgewicht unter gasmolekülen. *Sitzungsberichte Akademie der Wissenschaften*, 66:275–370, 1872.

[5] Lionel Boucher and Jean-Paul Grouiller. "COSI": The Complete Renewal of the Simulation Software for the Fuel Cycle Analysis. *ASME Conference Proceedings*, 2006(42428):865–870, January 2006.

[6] M CHADWICK, P OBLOZINSKY, M HERMAN, N GREENE, R MCK-NIGHT, D SMITH, P YOUNG, R MACFARLANE, G HALE, and S FRAN-KLE. ENDF/B-VII.0: Next Generation Evaluated Nuclear Data Library

for Nuclear Science and Technology. *Nuclear Data Sheets*, 107(12):2931–3060, December 2006.

[7] A G Croff. ORIGEN 2.2 - CCC-371. Technical report, Oak Ridge National Laboratory, 2002.

[8] M. J. Driscoll, Thomas Joseph Downar, and E. E. Pilat. *The linear reactivity model for nuclear fuel management.* American Nuclear Society, 1990.

[9] Brian S. Everitt. *ANALYSIS OF CONTINGENCY TABLES.* Chapman & Hall, 1992.

[10] Rodolfo Ferrer, Samuel E Bays, B Forget, and M Asgari. Minor Actinide Transmutation for Low Conversion Ratio Sodium Fast Reactors. In *GLOBAL 2007*, 2007.

[11] Jacob J Jacobson, Gretchen E Matthern, Steven J Piet, and David E Shropshire. VISION : Verifiable Fuel Cycle Simulation Model Advances in Nuclear Fuel Management. *Management*, 2009.

[12] KAERI. Table of Nuclides, 2000.

[13] John R. Lamarsh. *Introduction to nuclear reactor theory.* American Nuclear Society, 2002.

[14] Jaakko Lepp. PSG2 / Serpent a Continuous-energy Monte Carlo Reactor Physics Burnup Calculation Code. Technical report, 2011.

[15] J Li, M Nicholson, W C Proctor, M S Yim, and D N McNelis. Examining repository loading options to expand Yucca Mountain repository capacity. *In: Proc. Advanced Nuclear Fuel Cycles and Systems, GLOBAL*, 2007.

[16] J Li, A M Scopatz, M S Yim, and E A Schneider. The Sensitivity of Fuel Cycle Performance to Separation Efficiency. *Nuclear Engineering and Design*, 240:511–523, 2009.

[17] Jun Li, Man-sung Yim, and D N McNelis. An Efficient and Comprehensive Model for Fuel Cycle System Performance Evaluation. In *GLOBAL 2009*, Paris, France, 2009.

[18] Jun Li, Man-sung Yim, and D N McNelis. A Simplified Methodology for Nuclear Waste Repository Thermal Analysis. *Annals of Nuclear Energy*, 2010.

[19] Huibin Liu, Wei Chen, and Agus Sudjianto. Relative Entropy Based Method for Probabilistic Sensitivity Analysis in Engineering Design. *Journal of Mechanical Design*, 128(2):326, 2006.

[20] Christopher D. Manning and Hinrich Schuetze. *Foundations of Statistical Natural Language Processing*. The MIT Press, 1999.

[21] M. Mattes and J. Keinert. Thermal neutron scattering data for the moderator materials H2O, D2O and ZrHx in ENDF-6 format and as ACE library for MCNP (X) codes. Technical Report April, 2005.

245

[22] G. E. Michaels and T. D. Welch. Evaluation of Disposition Options for Reprocessed Uranium. Technical report, Oak Ridge National Laboratory, Oak Ridge, TN, USA, 1993.

[23] Nuclear Energy Agency. *Nuclear Data and Reaction Types*, 2009.

[24] OECD. Accelerator-driven Systems (ADS) and Fast Reactors (FR) in Advanced Nuclear Fuel Cycles. Technical report, 2002.

[25] OECD. Advanced Nuclear Fuel Cycles and Radioactive Waste Management - NEA-5990. Technical report, Nuclear Energy Agency, 2006.

[26] Kyle Matthew Oliver, Paul P H Wilson andc Arnaud Reveillere, Tae Wook Ahn, Kerry Dunn, Katy Huff, and Royal Elmore. Studying international fuel cycle robustness with the GENIUSv2 discrete facilities/materials fuel cycle systems analysis tool. In *GLOBAL 2009 - Accepted for publication*, 2009.

[27] Karl Pearson. *On the theory of contingency and its relation to association and normal correlation.* Dulau and Co., London, 1904.

[28] Denise B Pelowitz. MCNPX USER'S MANUAL Version 2.6.0 - LA-CP-07-1473. Technical report, Los Alamos National Laboratory, 2008.

[29] SJ Piet, RG Bennett, BW Dixon, JS Herring, DE Shropshire, Mark Roth, JD Smith, Phillip Finck, Robert Hill, James Laidler, and Others. On-Going Comparison of Advanced Fuel Cycle Options. In *Conference:*

Americas Nuclear Energy Symposium (ANES 2004), Miami, FL (US), 10/03/200410/06/2004, 2004.

[30] William H Press, Saul A Teukolsky, William T Vetterling, and Brian P Flannery. *Numerical Recipes 3rd Edition: The Art of Scientific Computing*. Cambridge University Press, 2007.

[31] N. Rashevsky. Life, information theory, and topology. *The Bulletin of Mathematical Biophysics*, 17(3):229–235, September 1955.

[32] E. Schneider, A. Scopatz, and M. Deinert. Depleted and Recyclable Uranium in the United States: Inventories and Options. In *GLOBAL 2007*, pages 1549–1554, Boise, Idaho, USA, 2007. American Nuclear Society, 555 North Kensington Avenue, La Grange Park, IL 60526 (United States).

[33] Erich A. Schneider, Charles G. Bathke, and Michael R. James. NFCSim : A dynamic fuel burnup and fuel cycle simulation tool. *Nuclear technology*, 151(1):35–50, 2005.

[34] Anthony Scopatz, Jun Li, Man-sung Yim, and Erich Schneider. Nuclear Fuel Cycle Sensitivity to the Variation of Physical Parameters. In *PHYSOR 2010*, Pittsburgh, PA, USA, 2010.

[35] Anthony M. Scopatz and Erich a. Schneider. A new method for rapid computation of transient fuel cycle material balances. *Nuclear Engineering and Design*, 239(10):2169–2184, October 2009.

[36] Author Scopatz, Jun Li, Man-sung Yim, and Erich Schneider. A Systemic Evaluation of the Sensitivity of Fuel Cycle. In *GLOBAL 2009*, Paris, France, 2009.

[37] V.F. Sears. Neutron scattering lengths and cross sections. *Neutron News*, 3(3):26–37, 1992.

[38] C E Shannon. A Mathematical Theory of Communication. *M.D. computing : computers in medical practice*, 14(4):306–17, 1948.

[39] D E Shropshire, K A Williams, E A Hoffman, J D Smith, D J Hebditch, J J Jacobson, J D Morton, A M Phillips, and J P Taylor. Advanced Fuel Cycle Economic Analysis of Symbiotic Light-Water Reactor and Fast Burner Reactor Systems - INL/EXT-09-15254. Technical Report January, Idaho National Labortory, Idaho Falls, ID, USA, 2009.

[40] F. Sokolov and H. P. Nawada. Viability of inert matrix fuel in reducing plutonium amounts in reactors - IAEA-TECDOC-1507. Technical Report August, International Atomic Energy Agency, Vienna, Austria, 2006.

[41] Weston M Stacey. Nuclear Reactor Physics. *Journal of Nuclear Energy Part A Reactor Science*, 10(5):54, 1959.

[42] Weston M. Stacey. *Nuclear Reactor Physics*. Wiley-VCH, 2007.

[43] M Takano. Burnup Credit Criticality Benchmark - Result of Phase 1A - NEA/NSC/DOC(93)22. Technical Report January, Nuclear Energy Agency, 1994.

248

[44] General Atomics GNEP Team. GNEP Deployment Studies : Executive Summary. Technical report, General Atomics, 2008.

[45] Satosi Watanabe. Information Theoretical Analysis of Multivariate Correlation. *IBM Journal of Research and Development*, 4(1):66–82, January 1960.

[46] Roald A Wiegland. Criteria Derived for Geologic Disposal Concepts. In *OECD/NEA 9th Information Exchange Meeting on Actinide and Fission Product Partitioning and Transmutation*, Nimes, France, 2006.

[47] a Yamamoto and N Sugimura. Improvement on multi-group scattering matrix in thermal energy range generated by NJOY. *Annals of Nuclear Energy*, 33(6):555–559, April 2006.

[48] YY Yao and S. Regina. 6 Information-Theoretic Measures for Knowledge Discovery and Data Mining. *Entropy measures, maximum entropy principle and emerging applications*, page 115, 2003.

[49] Hubert P. Yockey. *Information Theory, Evolution, and The Origin of Life*. Cambridge University Press, 2011.

Index

250

Vita

Anthony Michael Scopatz was born in these United States and spent many childhood years traversing them. Anthony then embarked on a Bachelor of Science in Physics at the University of California, Santa Barbara in 2002. Upon successful completion in 2006, graduate studies commenced at the University of Texas at Austin in the Nuclear and Radiation Engineering Program in the Mechanical Engineering Department. Anthony currently resides in Austin and wishes to escape Civilization for the great untamed wilds of North America with increased frequency. *Vox Clamantis in Deserto.*

Permanent address: scopatz@gmail.com

This dissertation was typeset with LaTeX[†] by the author.

[†]LaTeX is a document preparation system developed by Leslie Lamport as a special version of Donald Knuth's TeX Program.